INAUGURAL – DISSERTATION

zur Erlangung der Doktorwürde
der Naturwissenschaftlich-Mathematischen
Gesamtfakultät
der
Ruprecht-Karls-Universität
Heidelberg

Vorgelegt von
Dipl. Chem. Mariam Veschgini
geboren in: Teheran, Iran

Tag der mündlichen Prüfung: 16. Dezember, 2016

DISSERTATION

Submitted to the
Combined Faculty of Natural Sciences and Mathematics
Heidelberg University, Germany
for the degree of
Doctor of Natural Sciences (Dr. rer. nat.)

Presented by
Dipl. Chem. Mariam Veschgini
born in Teheran, Iran

Oral examination: December 16th, 2016

Viscoelasticity and Structure of Soft Biological Interfaces:
from Artificial Models to Living Tissues

Gutachter: Prof. Dr. Motomu Tanaka
Prof. Dr. Thomas W. Holstein

Zusammenfassung

In dieser Arbeit wurde die Mechanik dynamischer, biologischer Grenzflächen über verschiedene Ebenen struktureller Komplexität von pulmunalem Surfactant bis hin zu regenerativem Gewebe quantitative untersucht.

In Kapitel 3 wurde die Korrelation zwischen den biophysikalischen Eigenschaften der Extrazellulären Matrix, der Mesoglea, des Süßwasser Polypen Hydra und der damit verbundenen biologischen Funktionen erläutert. Im Körperbau der Hydren dient die Mesoglea als Trennschicht zwischen den externen (ektodermalen) und den internen (entodermalen) Zellschichten und verleiht dem Polypen seine mechanische Stabilität. In dieser Arbeit konnte unter Verwendung von nano-fokussierter Röntgenkleinwinckelstreuung unter streifendem Einfall (nano-GISAXS) die Struktur von Collagen Typ I aus isolierter mesoglea bestimmt werden. Diese war vergleichbar mit der des Vertebraten homologen Proteins. Zudem, wurde eine strukturelle Anisotropie in Bezug auf die orale-aborale Achse festgestellt, welche die ausgeprägten Dehnungen und Kontraktionen der Hydra entlang dieser Achse ermöglicht. Darüberhinaus, wurden die räumliche und zeitliche Entwicklung mechanischer Eigenschaften der Mesoglea mit "nano-indentation” unter zu Hilfenahme eines Rasterkraftmikroskops (AFM) *ex vivo* untersucht. Die Ergebnisse zeigten, dass Jungtiere anfänglich eine Einheitliche weiche Mesoglea hatten. Diese charakteristischen “Elastizitätsmuster” veränderten sich jedoch mit der Zeit und in Verbindung mit ihrer asexuellen Reproduktion. Diese mechanischen Modifizierungen konnten mit Hilfe einer quantitativen Proteomanalyse, die eine veränderte Protease-expression nachwies, erklärt werden. Eine Umwandlung des Körpergewebes in Kopfgewebe, entweder chemisch induziert oder durch eine Überexpression von β-Catenin, führte zu einer Erniedrigung des elastischen Moduls über die gesamte Mesoglea. Das Ergebnis zeigt, dass die räumlich-zeitliche, mechanische Musterbildung in der Mesoglea mit der Stammzellenaktivität verbunden ist.

In Kapitel 4 wurden mit Hilfe einer hoch empfindlichen zwei-finger mikro-Roboterhand die viskoelastischen Eigenschaften von Hydra Gewebefragmenten während der frühen Phase der Regenration bestimmt. Der Elastizitätsmodul der Hydra Regenrate wurde durch eine lineare Kompression des Gewebes bestimmt, wobei deren Verformung gering gehalten wurde. Bei einem konstanten Verformungsgrad konnte die Spannungsrelaxation der Regenerate unter Verwendung des Maxwell-Modells für viskoelastische Materialien analysiert werden. Dabei wurden der Stokesche Reibungskoeffizient und das Viskositätsmodul bestimmt. Im Weiteren, wurde die vom Regenerat erzeugte Kraft gemessen, welche eine enge Korrelation zu den morphologischen Veränderungen der Kontrollprobe zeigte.

In Kapitel 5 wurde die Inaktivierung des pulmunalen Surfactants im Verlauf des Akuten progressive Lungenversagens (ARDS) simuliert. Dabei wurde die Kompetitive Adsorption von Dipalmitoylphosphatidylcholine (DPPC) und bovinem Serumalbumin (BSA) an der Wasser-Luft Grenzfläche untersucht und die dynamisch oszillierende Grenzfläche der Alveolen durch eine periodische Änderung der Oberfläche modelliert. Anhand dieses Modells wurde der Einfluss von Perfluorohexan (PFH) als potentielles Therapeutikum untersucht. Mit Hilfe der Fluoreszenzmikroskopie wurde eine beschleunigte Verdrängung von adsorbiertem BSA durch DPPC in Anwesenheit von PFH festgestellt, welche von einer signifikanten Änderung der viskoelastischen Eigenschaften der Grenzfläche begleitet wurde. Dies lässt den Einbau vom PFH in die Proteinschicht vermuten.

Summary

The primary aim of this thesis is to shed a quantitative light on the mechanics of dynamic biological interfaces with different levels of structural complexities, ranging from lung surfactant models to regenerating tissues.

In chapter 3, the correlation between biophysical properties and function of the native extracellular matrix (ECM), mesoglea, of the freshwater polyp Hydra was studied. In the body design of Hydra, mesoglea acts as an interlayer between external (ectodermal) and internal (endodermal) cell layers, sustaining the mechanical integrity of polyps. In this study, nano-focused grazing incidence small angle X-ray scattering on isolated mesoglea revealed that the packing order of Hydra collagen type I was comparable to its vertebrate homologue. The structure was anisotropic with respect to the oral-aboral axis, supporting the extensive extension and contractions of the body along this axis. In the next step, the spatio-temporal evolution of mesoglea mechanics was tracked *ex vivo* by nano-indentation using an atomic force microscope. The experimental data demonstrated that freshly detached polyps initially had a uniformly soft mesoglea, but mesoglea changed the characteristic "elasticity patterns" during the asexual reproduction. This change could be explained by a quantitative proteome analysis, implying that the mechanical remodeling of Hydra was highly correlated with protease expression activity. When the body column tissue was transformed into head tissue either by a drug or by the over-expression of β-catenin, mesoglea had low elastic moduli over the whole body. This result suggests that the spatio-temporal patterns in mesoglea mechanics is strongly correlated with the stem cell activity.

In chapter 4 a highly sensitive two-fingered micro-robotic hand was used to determine the viscoelastic properties of Hydra tissue fragments (regenerates) during early stages of regeneration. Owing to the dexterous grasping motion of microobjects realized by the micro-robot, the bulk elastic modulus of Hydra regenerates could be determined by linearly compressing the tissue by keeping the strain level low. Under a constant strain, the stress relaxation behavior could be interpreted by applying the Maxwell model of viscoelastic materials, yielding the Stokes frictional coefficient and viscous modulus. Furthermore, the forces actively generated by the regenerate were measured and shown to correlate well with shape fluctuations of a freely regenerating sample.

In chapter 5, lung surfactant inactivation by serum proteins during the acute respiratory distress syndrome (ARDS) was simulated. As the model of dynamic, oscillating interfaces in lung, the competitive adsorption of dipalmitoylphosphatidylcholine (DPPC) and bovine serum albumin (BSA) to the air/water interface was monitored by periodically changing the surface area. The model was used to investigate the impact of perfluorohexane (PFH) as a potential therapeutics. The lipid-protein composite films at the air/water interface in the presence and absence of PFH gas could be visualized by fluorescence microscopy, indicating an accelerated displacement of a pre-adsorbed BSA by DPPC in saturated PFH atmosphere. The acceleration of BSA-DPPC replacement under PFH atmosphere was accompanied by significant changes in viscoelasticity of the interface, suggesting the incorporation of PFH to the protein layer.

Acknowledgements

I would first like to thank my supervisor Prof. Dr. Motomu Tanaka for giving me the opportunity to work in his lab, for the inspiring and fruitful scientific discussions and for his support and guidance throughout the last years. I am also grateful for the chance to spend part of my PhD at the Institute for Integrated Cell-Material Sciences (iCeMS) in Kyoto.

I am thankful to Prof. Dr. Thomas Holstein and Dr. Suat Özbek for introducing me to the fascinating field of developmental biology of Hydra, close collaboration and the productive discussions. I am also grateful to Prof. Dr. Thomas Holstein for his guidance and support throughout the past years.

I am grateful to Prof. Dr. Marie-Pierre Krafft for the fruitful collaboration and scientific discussions on the lung surfactant model and the intriguing field of semifluorinated alkanes.

My sincere thanks to Prof. Dr. Tatsuo Arai for the great opportunity to work with a unique micro-robotic device.

I would like to acknowledge Dr. Oleg Konovalov, Dr. Manfred Burghammer and Dr. Emanuela Di Cola for their help and support during the scattering experiments at the European Synchrotron Radiation Facility in Grenoble.

Many thanks to Dr. Wasim Abuillan, Dr. Hendrik Petersen, Nyamdorj Khangai and Florian Gebert for the great co-operation, their support during the experiments and fruitful scientific discussions.

I would like to thank Mieko Yoshida, Dr. Akihisa Yamamoto and Dr. Marcel Hörning for their support and hospitality throughout my stay in Kyoto.

I am grateful to Dr. Stefan Kaufmann and Dr. Wasim Abuillan for proofreading of my thesis.

Thanks to the Deutsche Forschungsgemeinschaft for the financial support (GRK1114 and EcTop2).

I would also like to acknowledge Klaus Schmitt and his team for the great technical assistance.

I thank all members of the working groups of Prof. Tanaka and Prof. Holstein for the friendly atmosphere, the great time and their help and support during the beam times.

I would also like to express my deepest gratitude to my family for their love and permanent support throughout my life.

Table of Contents

Chapter 1

General Introduction

Biological systems generate, sense and respond to both chemical and physical signals over a wide range of length scales from single cells up to tissues and organs [1].

For example, cells feel the physical properties of their microenvironments by interactions with extracellular matrix and neighboring cells (Figure 1.1) [2]. The adhesion molecules involved in these connections transduce the forces into biochemical signaling (Mechanotransduction) [2]. For example, focal adhesion complexes (cell-ECM adhesions via the trans-membrane receptor integrin) lead to the remodeling of cytoskeletons, which modulates the tension that is exerted on cell nuclei [2, 3].

The impact of the mechanical properties of the extracellular matrix (ECM) on *in vitro* cell behavior has been studied intensively by using hydrogel substrates possessing defined elastic moduli. Shape, migration, proliferation and differentiation of various cell types were shown to depend strongly on elasticity of the substrate [4-6]. For example, high substrate stiffness was shown to facilitate migration and proliferation of epidermal cells [7], and not only the elasticity but also the viscosity of substrates enhance the cell spreading [8]. The mechanical properties of

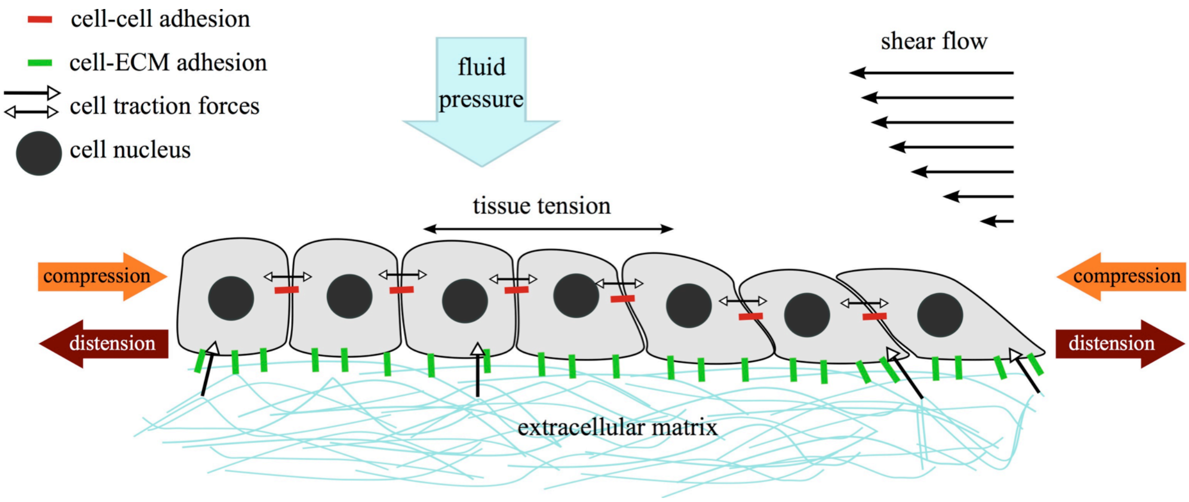

Figure 1.1. Cells feel and respond to mechanical forces and physical properties of their microenvironment. Cell-matrix and cell-cell adhesions are the mechanosensors of individual cells. Cell-cell adhesions transmit mechanical stimuli within tissues and contribute to the tissue tension. Cells and tissue are exposed to a variety of forces throughout animal life, which regulate the embryonic development as well as maintenance and functioning of adult organs.

the cell substrate are also important in maintenance, differentiation and linage specification of stem cells [9-11]. Engler et al., for example, demonstrated that substrate elasticity guided the differentiation of human mesenchymal stem cells to neurons, myoblasts or osteoblasts [12]. On the other hand, it is known that the dysregulation of ECM homeostasis is associated with various diseases like fibrosis and cancer [3, 13, 14]. However, almost all the previous studies still remain on the single cell level in vitro, and therefore little is known about how ECM remodeling coordinates (stem) cell function in *in vivo* tissues.

Cell-ECM interactions are correlated with cell-cell adhesions and thus tissue morphogenesis [1, 15]. A vivid example at early stages of embryogenesis in multicellular animals is the gastrulation. During gastrulation embryonic cells are separated into three germ layers (the ectoderm, mesoderm and endoderm) that establish the basic body plan [1]. The process is marked by tissue invagination, followed by the remodeling of ECM and massive collective cell migrations, which are regulated by a close interplay between cell-ECM and cell-cell interactions [16, 17]. These morphological movements are correlated with the gene expression pattern in drosophila embryos [18]. For example, a total failure of morphogenesis was reported when cell migrations were disturbed by cell ablation [19]. Similar, but the process going to the opposite direction of gastrulation is the extravasation of tissue, such as an asexual reproduction of freshwater polyps Hydra (Figure 1.2a) [20]. Here, the extravasation of "buds"

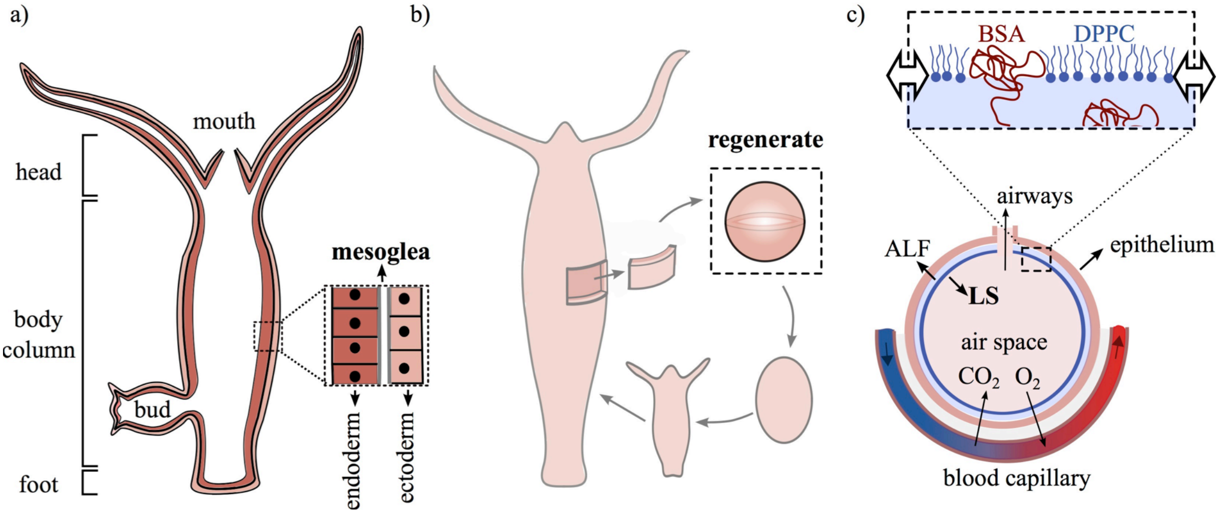

Figure 1.2. Schematic overview of systems investigated in this study. a) The spatio-temroral evolution of the mechanical properties of the native extracellular matrix (mesoglea) of the freshwater polyp Hydra is studied in chapter 3. b) In chapter 4 the mechanical aspects of the regenerating Hydra tissue fragments (regenerates) are elucidated during early stages of regeneration. c) A simplified model of the lung surfactant (LS) is used in chapter 5 to study the LS inactivation by serum albumin during ARDS (box). The impact of perfluorohexane is investigated as a potential therapeutics. Note that the schematic is not in scale. White arrows indicate compression and expansion of the interfacial film. ALF: alveolar lining fluid

towards the outside is also followed by the remodeling of ECM and collective cell migrations [21]. In Chapter 3, the spatio-temporal remodeling of Hydra ECM (mesoglea) is investigated by mapping the elastic modulus of *ex vivo* samples during the asexual self-reproduction process. The obtained results are discussed in terms of the change in protein expression patterns as well as the stem cell activities.

It is notable that the embryonic development is also susceptible to external mechanical cues [22]. For example, the osmotic pressure of the fluid inside sea urchin blastocysts decreases before tissue invagination [23, 24], while an enforced increase in osmotic pressure resulted in a delay or even reversion of tissue invagination [25]. The turgor pressure also plays crucial roles when a small piece of tissue cut off the Hydra body column regenerates into an intact polyp (Figure 1.2b) [26]. The tissue fragments first curl up into a hollow tissue sphere with a fluid-filled core, which undergoes extensive expansion-contraction cycles during regeneration [26]. These size fluctuations were reported to be driven in an osmoregulatory manner: an increase in the osmolarity outside the tissue sphere results in a delayed regeneration process or a complete failure [26]. However, despite the important role of mechanical forces in pattern formation during early development, only little is known about the magnitude of these forces or the viscoelastic properties of the tissue, which determine the response of the tissue to these regulating forces. In Chapter 4, a highly sensitive two-fingered micro-robotic hand (~ 1 nN) [27] was used to determine the viscoelastic properties of Hydra tissue fragments (regenerates) during early stages of regeneration. The dexterous grasping motion of micro-objects by the micro-robotic device allowed a quantitative determination of both viscous and elastic modulus of regenerating tissues from the linear stress-strain relationships and stress relaxation measurements.

Mechanical stimuli are also crucial for the proper formation of different organs at later stages of embryonic development as well as for the organ homeostasis in adults [1, 28]. For example, a normal growth and development of the lung depends on the lung distension during embryonic development, which is regulated by fetal breathing movements as well as tracheal and amniotic fluid pressures [16, 29]. An over-distension of the fetal lung due to an increase in the tracheal fluid pressure results in larger lungs with a higher number of alveoli, while an under-distension by drainage of the tracheal fluid results in an underdeveloped lung [29, 30].

The proper functioning of organs is also related to their mechanical environment. For example, the alveolar epithelium, across which the gas exchange takes place, is lined with the alveolar lining fluid (ALF), containing a surfactant complex [31]. The lung surfactant complex facilitates the expansion of the alveoli during inhalation while preventing the alveoli collapse upon exhalation by reducing the surface tension of ALF [31]. An abnormal high ALF surface tension is associated with severe and potentially lethal diseases like the acute respiratory distress syndrome (ARDS) [32]. In the coarse of ARDS, serum proteins like albumin leak into the alveolar air space and hinder the adsorption of the lung surfactant to the ALF interface, resulting in the collapse of the alveoli [32, 33]. In chapter 5, dynamic, oscillating interfaces in lung was modeled by periodically changing the surface area at the air/water interface. Here, the competitive adsorption of dipalmitoylphosphatidyl-choline (DPPC) and bovine serum albumin (BSA) to the interface was monitored. A special focus was put on the impact of perfluorohexane (PFH), which is considered as a potential therapeutics. The replacement of BSA by DPPC was accelerated in the presence of PFH, suggesting the incorporation of PFH to the protein layer plays crucial roles.

Chapter 2
Theoretical Background

2.1 Viscoelasticity

The deformation of a body in response to external forces is described by the stress-strain relationship [34].

2.1.1 Stress

The stress, σ, is defined as force per unit area [34]:

$$\sigma = \frac{F}{A} \qquad (2.1)$$

where A represents the total area of the surface on which the force, F, is applied. Generally, the stress describes the interaction of material in one part of the body on the other via internal forces [35]. The stress felt by an arbitrary point inside the body, B, can be represented by considering the forces exerted on an infinitesimal cubic volume at a given point inside B as shown in Figure 2.1.1 [35, 36]. The stress vectors acting on each of the six surfaces of the cube can be decomposed into three components: the normal stress, σ_{ij}, which is is perpendicular to each surface and two tangential components, τ_{ij}, representing shear stresses. Equal and

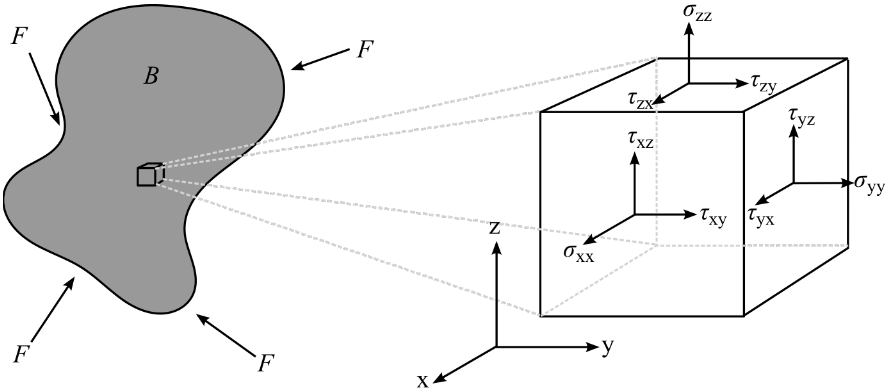

Figure 2.1.1 The application of external forces on a deformable body B generates internal stresses. The stress at any point is represented by nine components: three normal σ_{ij} and six tangential stress components τ_{ij}. (inspired by Ref No. 35)

opposite components exist on opposing surfaces [35]. Thus, using Cartesian coordinates, the stress is represented by nine components i.e. a tensor of rank 2 [35, 36]:

$$\sigma_{ij} = \begin{pmatrix} \sigma_{xx} & \tau_{xy} & \tau_{xz} \\ \tau_{yx} & \sigma_{yy} & \tau_{yz} \\ \tau_{zx} & \tau_{zy} & \sigma_{zz} \end{pmatrix} \tag{2.2}$$

Under equilibrium the stress matrix is symmetric, i.e.:

$$\tau_{xy} = \tau_{yx}, \qquad \tau_{xz} = \tau_{zx}, \qquad \tau_{yz} = \tau_{zy} \tag{2.3}$$

Thus, leaving six independent stress components [36].

2.1.2 Strain

The deformation of a material in response to an applied stress is quantified by the strain, a dimensionless ratio reflecting the relative deformation of the body [34]. Figure 2.1.2 schematically represents the deformation of a body when subjected to (a) one-dimensional normal or tensile stress and (b) shear stress. A one-dimensional normal stress, σ_{xx}, results in extension or compression of a solid body. The tensile strain is usually given by:

$$\varepsilon_{xx} = \frac{L - L_0}{L_0} = \frac{L}{L_0} - 1 \tag{2.4}$$

Where L_0 and L represent the initial and final length of the body, respectively (Figure 2.1.2.a) [35]. The deformation of an object in one direction may be accompanied by changes, e.g. in the direction perpendicular to the applied stress. This is reflected by Poisson's ratio, ν, which reflects the ratio between the deformation transversal, ε_{zz}, to the applied stress (σ_{xx}) to the deformation on the direction of the stress, ε_{xx}:

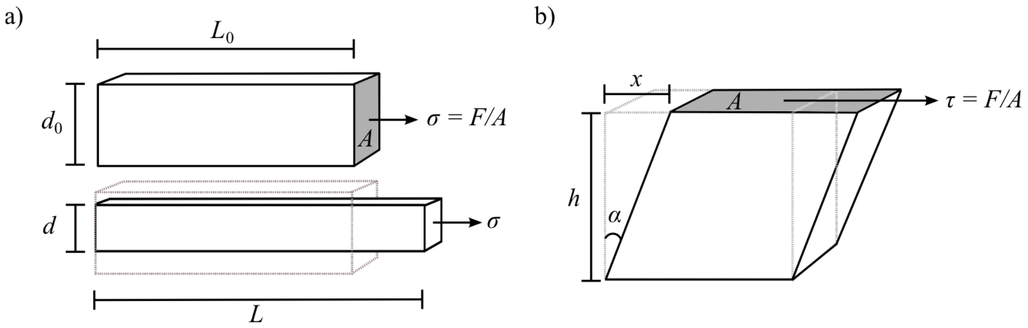

Figure 2.1.2. Deformation of a solid body when subjected to a) tensile stress: The relative elongation is a usual measure of the tensile strain and b) shear stress: the shear strain is defined by tan α.

$$\upsilon = -\frac{\varepsilon_{zz}}{\varepsilon_{xx}} = -\frac{(d-d_0)/d_0}{\varepsilon_{xx}} \tag{2.5}$$

where d_0 and d represent the initial and final thickness of the body, respectively [36].

On the other hand, when a tangential shear stress, τ, is applied to a body the resulting shear strain is given by:

$$\gamma = \frac{x}{h} = \tan\alpha \tag{2.6}$$

where h represents the initial height of the object and x is the transversal displacement of the upper plane as shown in Figure 2.1.2b [34, 35].

Similar to the stress, the strain can be represented by a symmetric tensor of rank 2 [36]:

$$\epsilon_{ij} = \begin{pmatrix} \varepsilon_{xx} & \gamma_{xy} & \gamma_{xz} \\ \gamma_{yx} & \varepsilon_{yy} & \gamma_{yz} \\ \gamma_{zx} & \gamma_{zy} & \varepsilon_{zz} \end{pmatrix} \tag{2.7}$$

With: $$\gamma_{xy} = \gamma_{yx}, \qquad \gamma_{xz} = \gamma_{zx}, \qquad \gamma_{yz} = \gamma_{zy} \tag{2.8}$$

How matter responses to an applied stress depends on the material mechanical properties and is expressed by the constitutive equations [35]. Some simple, idealistic constitutive equations will be introduced in the following.

2.1.3 Hookean Elastic Solids

Is the response of an elastic solid to a one-dimensional tensile stress linear i.e. obeys Hook's law

$$\sigma = E\varepsilon \tag{2.9}$$

the material is said to be a Hookean material [35]. The proportionality constant E is called the Young's modulus [36]. These materials also show a linear stress-strain relation for shearing so that:

$$\tau = G\gamma \tag{2.10}$$

where G represents the shear modulus [36]. For an isotropic and homogeneous elastic material the generalizes three dimensional Hooke's law corresponds to

$$\varepsilon_{xx} = \frac{1}{E}\left[\sigma_{xx} - \upsilon(\sigma_{yy} + \sigma_{zz})\right], \qquad \gamma_{xy} = \frac{\tau_{xy}}{G}$$

$$\varepsilon_{yy} = \frac{1}{E}\left[\sigma_{yy} - \upsilon(\sigma_{xx} + \sigma_{zz})\right], \qquad \gamma_{yz} = \frac{\tau_{yz}}{G} \tag{2.11}$$

$$\varepsilon_{zz} = \frac{1}{E}\left[\sigma_{zz} - \upsilon(\sigma_{xx} + \sigma_{yy})\right], \qquad \gamma_{xz} = \frac{\tau_{xz}}{G}$$

where ν represents Poisson's ratio (Eq. 2.5) [36]. In this case, the Young's modulus and the shear modulus are related by the equation [36]:

$$E = 2G(1+\nu) \tag{2.12}$$

2.1.4 Newtonian Viscos Fluids

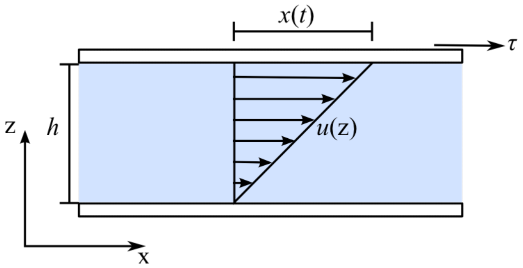

Figure 2.1.3. Shearing of a fluid. The upper plate is moved at a constant velocity u = u (h) relative to the lower stationary plate. For Newtonian viscos fluids the velocity changes linearly across the gap. (inspired by Ref. No. 35)

To describe the flow of a fluid, the strain rate needs to be considered [34]. Figure 2.1.3 illustrates the shearing of a fluid between two parallel plates. The upper plate moves with a constant velocity of *u,* while the bottom plate is stationary. Thus, the flow velocity decreases across the gap, reaching zero at the bottom plate. Considering that a differential element inside the fluid at a time point *t* shows a strain of *dx*(*t*)*/dz*, the strain rate is given by [34, 37]

$$\dot{\gamma} = \frac{d\gamma}{dt} = \frac{d}{dt} \cdot \frac{dx}{dz} = \frac{du}{dz} \tag{2.13}$$

Ideally viscos fluids show a linear relationship between shear stress and strain rate

$$\tau = \eta\dot{\gamma} \tag{2.14}$$

where the proportionality constant η is the viscosity of the fluid [34, 37]. Fluids that obey equation (2.14) are said to be Newtonian fluids [34, 37].

Although these idealized models described the behavior of some materials, at least within limited ranges of stress and strain, the response of most materials to stresses is more complex showing both viscos and elastic behavior [35]. As for the ideal behavior, mechanical models are also designed to describe the stress-strain relation of a viscoelastic material. These models consist of parallel or serial combinations of Hookean elastic solid, represented by a spring, and a Newtonian viscos fluid, represented by a dashpot [35]. As the two elements exhibit an ideal linear behavior, any combination of them shows a linear viscoelastic response [38]. The two simplest models for viscoelastic materials, the Maxwell model and the Kelvin-Voigt model, will be briefly introduced in the following.

2.1.5 Maxwell Model

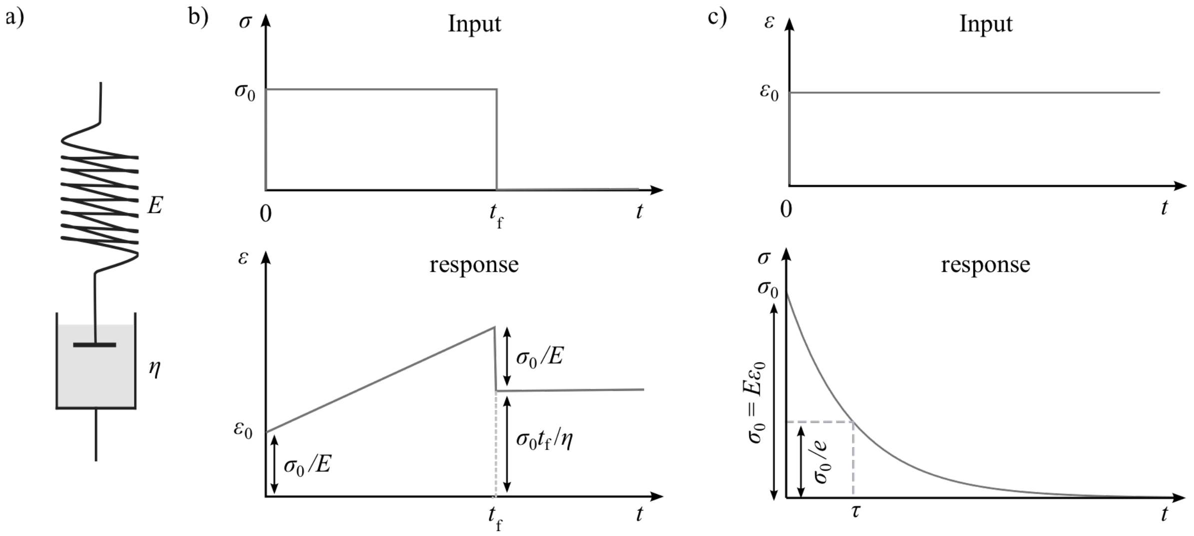

Figure 2.1.4. The Maxwell model for viscoelastic materials is modeled by a) a serial combination of a elastic solid with spring constant E and a Newtonian Fluid with viscosity η. b) Creep and creep recovery of a Maxwell material. Top: applied stress, Bottom: strain response. c) Stress relaxation of a Maxwell material. Top: applied strain, Bottom: stress response.

As shown in Figure 2.1.4a the Maxwell model consists of a serial combination of a Hookean elastic solid, “spring”, with the elastic modulus E and a Newtonian viscos fluid, “dashpot”, with the viscosity η, thus the stress felt by each component equals the total stress σ [37]:

$$\sigma = \sigma_s = \sigma_d \tag{2.15}$$

The indices s and d represent the spring and dashpot, respectively. The total strain ε is given by [37]:

$$\varepsilon = \varepsilon_s + \varepsilon_d \tag{2.16}$$

Using the constitutive equation for a Hookean spring, the strain ε_s can be calculated as

$$\varepsilon_s = \frac{\sigma_s}{E} \tag{2.17}$$

While the strain rate of the dashpot is given by

$$\dot{\varepsilon}_d = \frac{d\varepsilon_d}{dt} = \frac{\sigma_d}{\eta} \tag{2.18}$$

By replacing Eq. (2.17) and (2.18) into Eq.(2.16), the constitutive equation for a Maxwell material is obtained to be [37]:

$$\dot{\varepsilon} = \frac{\dot{\sigma}}{E} + \frac{\sigma}{\eta} \tag{2.19}$$

when a Maxwell material is suddenly subjected to a constant strain σ_0 ($d\sigma_0/dt = 0$), the spring reacts immediately while the response of the dashpot is delayed. Thus, $\varepsilon_0 = \sigma_0/E$ [35, 37]. The change in strain over time is given by

$$\varepsilon(t) = \sigma_0\left(\frac{1}{E} + \frac{t}{\eta}\right) = \sigma_0 J(t) \tag{2.20}$$

Where $J(t)$ is the creep compliance [35, 37]. When the stress is removed at time t_f, the spring recovers immediately, $\varepsilon_s(t_f) = 0$ but the system sustains a permanent strain attributed to the viscos component [35, 37]. The creep-recovery of a Maxwell model is represented in Figure 2.1.4b.

On the other hand, When a Maxwell body is subjected to a sudden constant strain ε_0 ($d\varepsilon_0/dt = 0$), which induces an initial stress $\sigma(t = 0) = \sigma_0$, the stress relaxes over time according to

$$\sigma(t) = \varepsilon_0 E e^{-t/t_r} = \varepsilon_0 E(t); \quad t_r = {}^{\eta}/_{E} \tag{2.21}$$

t_r can be considered as the characteristic relaxation time of the system [37, 38]. $E(t)$ is called the relaxation modulus [37]. The stress relaxation behavior of the Maxwell model is illustrated in figure 2.1.4c.

2.1.6 Kelvin-Voigt Model

The Kelvin-Voigt model consists of a parallel connection of a spring and dashpot (Figure 2.1.5a) [37]. Thus, in contrast to the Maxwell model, in this configuration both spring and dashpot show the same strain:

$$\varepsilon = \varepsilon_s = \varepsilon_d \tag{2.22}$$

,while the stress is given by [37]

$$\sigma = \sigma_s + \sigma_d \tag{2.23}$$

By using the stress-strain relationships for “spring” and “dashpot” (Eqs. (2.17) and (2.18)) the constitutive equation for the Kelvin-Voigt materials is obtained as [37]:

$$\sigma = E\varepsilon_s + \eta\dot{\varepsilon}_d \tag{2.24}$$

The creep-recovery of a Kelvin-Voigt body is shown in Figure 2.1.5b. If a kelvin-Voigt body is subjected to a step stress, the dashpot hinders an immediate deformation of the spring.

Thus $\varepsilon\ (t = 0) = 0$ [37]. Solving the differential equation (2.24) reveals a creep response according to:

$$\varepsilon(t) = \frac{\sigma_0}{E}\left(1 - e^{-t/\tau}\right) \tag{2.25}$$

Thus the creep compliance $J(t)$ is given by [35, 37]

$$J(t) = \frac{\varepsilon(t)}{\sigma_0} = \frac{1}{E}\left(1 - e^{-t/\tau}\right) \tag{2.26}$$

with

$$\tau = \frac{\eta}{E} \tag{2.27}$$

τ is called the retardation time [37]. When the stress is released at time $t = t_f$, the dashpot again hinders the spring from instantaneous relaxation. The dashpot relaxes exponentially with a relaxation time given in Eq. (2.27) [35].

When a Kelvin-Voigt body is subjected to a step strain, the response can be expressed by:

$$\sigma(t) = E\varepsilon_0 + \eta\varepsilon_0\delta(t) \tag{2.28}$$

Where $\delta(t)$ corresponds to the delta Dirac function [35]. Accordingly, at $t = 0$ an infinite stress is necessary to induce a fine strain in the dashpot. At $t > 0$ the constitutive equation reduces to the elastic term $\sigma = E\varepsilon_0$ and a constant stress value is sustained over time with no relaxation is observed (Figure 2.1.5c) [35].

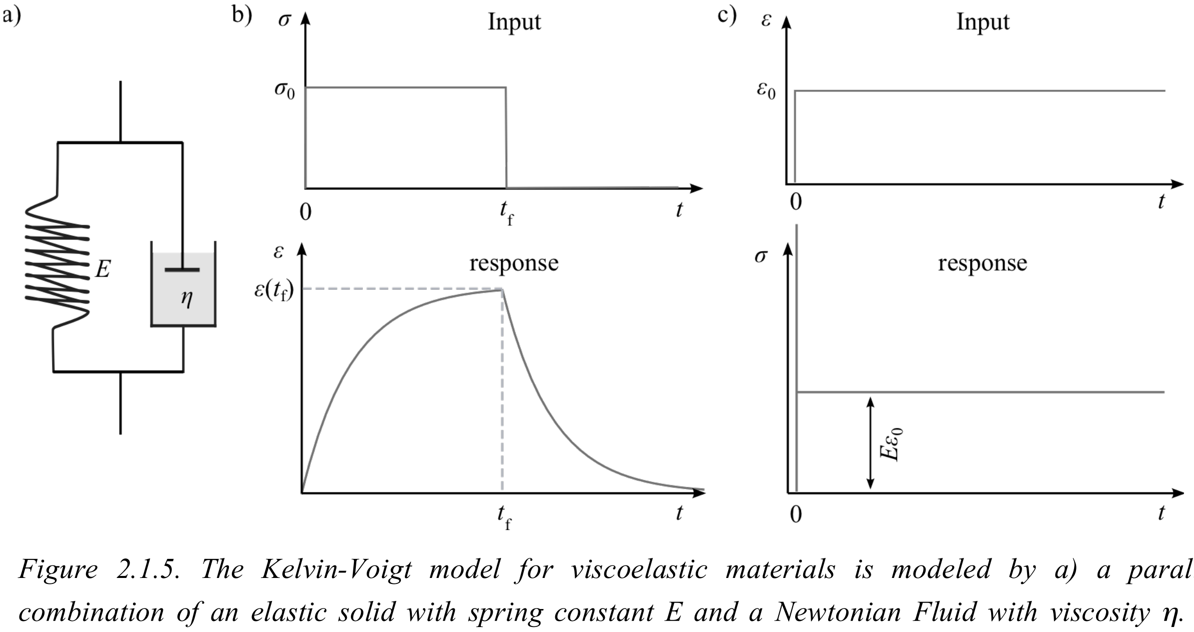

Figure 2.1.5. The Kelvin-Voigt model for viscoelastic materials is modeled by a) a parallel combination of an elastic solid with spring constant E and a Newtonian Fluid with viscosity η. b) Creep and creep recovery of a Kelvin-Voigt body. Top: applied stress, Bottom: strain response. c) Relaxation function of a Kelvin-Voigt material. Top: applied strain, Bottom: stress response.

2.1.7 Response of Deformable Body to Harmonic Strain or Strain

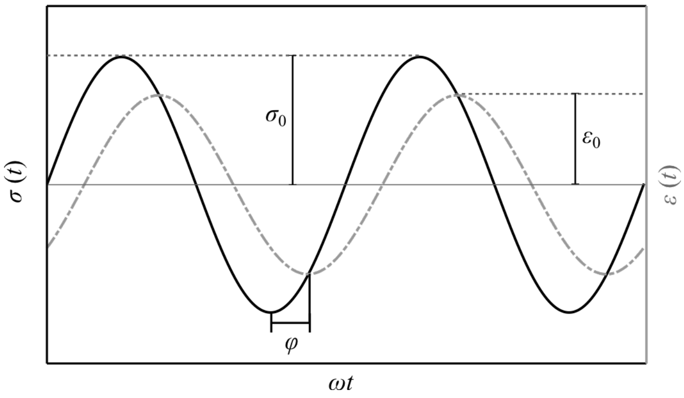

Figure 2.1.6. Stress response of a viscoelastic body to an oscillatory strain ε(t).

The constitutive equations enable the description of more complex material behavior; for example the response to oscillating strain or stress, which is the basic measurement principle of several rheological tests [39].

When an oscillating strain with an angular frequency ω and amplitude ε_0 as

$$\varepsilon(t) = \varepsilon_0 e^{i\omega t} \tag{2.29}$$

$$\dot{\varepsilon}(t) = i\omega\varepsilon_0 e^{i\omega t} = i\omega\varepsilon(t) \tag{2.30}$$

is applied to a general viscoelastic model, the resulting stress changes periodically with time

$$\sigma(t) = \sigma_0 e^{i(\omega t+\varphi)} \tag{2.31}$$

$$\dot{\sigma}(t) = i\omega\sigma(t) \tag{2.32}$$

where φ is the phase angle, which represents a delay of the stress response with respect to the strain input (Figure 2.1.6) [38].

The general stress-strain relation is given by

$$\sigma(t) = G^*(\omega)\varepsilon(t) \tag{2.33}$$

where $G^*(\omega)$ is a complex quantity, called the complex modulus [39]. It is a material property and can be decomposed into a real and an imaginary part according to [38, 39]

$$G^*(\omega) = G'(\omega) + iG''(\omega) \tag{2.34}$$

The real term, $G'(\omega)$ is called the storage modulus and reflects the elastic part, while the imaginary term $G''(\omega)$ is the loss modulus, which represents the viscos response [38, 39].

The origin of the phase shift φ can be clarified by presenting the complex modulus in the complex plane:

$$G^*(\omega) = |G^*(\omega)|e^{i\varphi} \tag{2.35}$$

with a magnitude

$$|G^*(\omega)| = \sqrt{(G'(\omega))^2 + (G''(\omega))^2} \tag{2.36}$$

and a phase angle φ [35, 39]:

$$\tan\varphi = \frac{G''(\omega)}{G'(\omega)} \tag{2.37}$$

Accordingly, the phase shift at a particular frequency ω depends on the material viscoelastic properties. This can be visualized by stress-strain plots as demonstrated schematically in figure 2.1.7 [39]. The stress response of a Hookean solid is in phase with the input strain $\varphi = 0$, thus the stress-strain plot is a straight line [39]. An increase in the viscos term leads to the broadening of the line yielding elliptic patterns for viscoelastic materials [39]. Is the material purely viscos the stress response is out of phase with $\varphi = \pi/2$ resulting in a circular pattern [39].

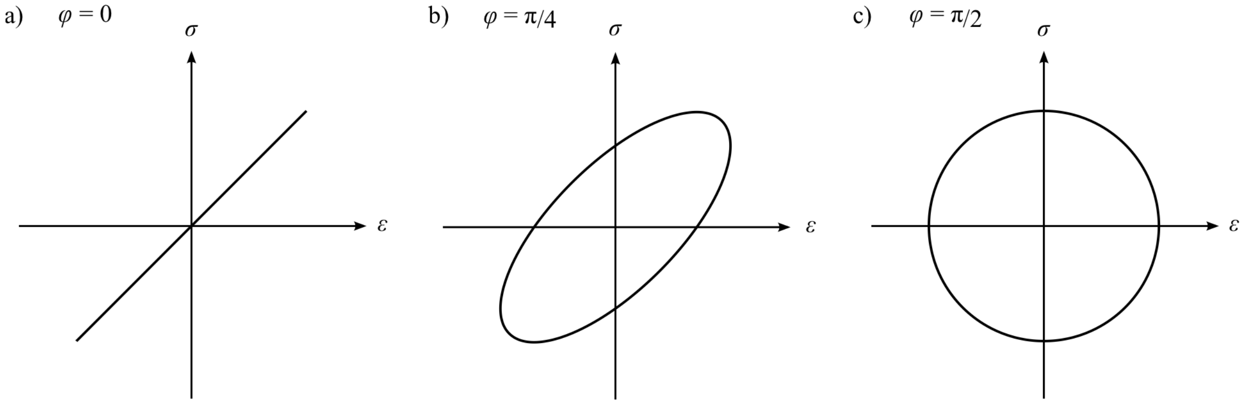

Figure 2.1.7. Stress-strain hysteresis with a) $\varphi = 0$ (Hookean elastic body) b) $\varphi = \pi/4$ (linear viscoelastic body) with and c) $\varphi = \pi/2$ (Newtonian viscos fluid).

2.2 Atomic Force Microscopy: Nano-Indentation

The atomic force microscope (AFM) is a scanning probe microscopy technique that not only allows high-resolution imaging of surface topographies but also enables the determination of surface forces as well as material mechanical properties with a high spatial resolution [40].

The central component of an AFM is a tip attached to the end of a flexible cantilever, which probes the sample surface (Figure 2.2.1a). The tip is scanned over the surface by means of a piezoelectric translator (PZT), which moves, based on the design, either the cantilever (Figure 2.2.1a) or the sample in xyz-direction with sub-nanometer accuracy [41]. The sample is characterized based on interactions between the tip and the sample surface: long-range interactions like magnetic, electrostatic or van der Waals forces or short-range (sub nanometer range) interactions like steric or chemical interactions attract or repel the tip towards or away from the sample surface in a distance dependent manner [41, 42]. The interaction force, F, can be determined from the resultant cantilever deflection (Δz_c) using Hook's law

$$F = k_c \Delta z_c \qquad (2.38)$$

where k_c represents the cantilever spring constant, which depends on the material (Young's modulus) and geometry of the cantilever. The most popular method for the measurement of the cantilever deflection, Δz_c, is the laser beam deflection method in which a laser beam is focused on the backside of the cantilever and the reflected beam is detected using a photodiode [41]. The photodiode is usually split into four sections (Figure 2.2.1.) [41, 42]. Any bending of the cantilever results in a displacement of the reflected beam and a change in the voltage of the four quadrants of the photodiode (Figure 2.2.1). Voltage differences between the upper and lower quadrants measure the vertical deflection, while the lateral deflection is determined by the signal difference between left and right sections [41]. To convert the photodiode signal ΔU [V] into length units the system sensitivity $S = \Delta z_c / \Delta U$ needs to be known [41, 43]. S can be obtained by pushing the cantilever against an infinitely hard sample and will be explained in more detail later. The beam deflection technique amplifies the cantilever

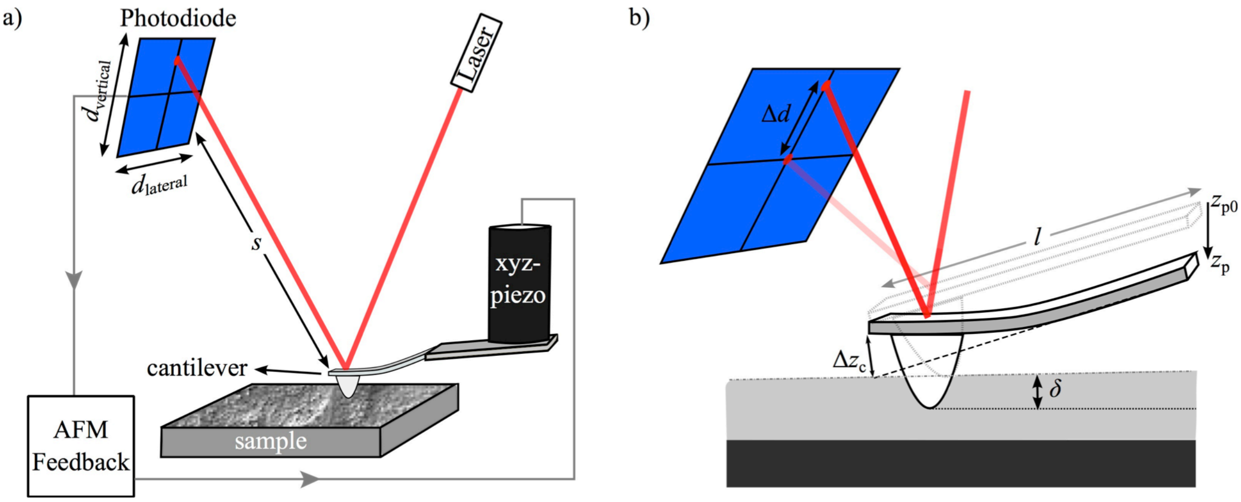

Figure 2.2.1 Scheme of an atomic force microscope. a) The sample is probed by a tip attached to the end of a flexible cantilever. The sample surface is scanned by moving the cantilever in xyz-direction with nm-accuracy using a piezoelectric translator. Tip-sample interactions result in cantilever bending, which is amplified and detected by the beam deflection method. b) Nano-indentation of a soft substrate. The indentation depth δ can be determined from the difference between the distance traveled by the cantilever (z_p - z_{p0}) and cantilever deflection Δz_c. The bending of the cantilever deflects a laser beam that is focused on the cantilever backside by Δd, which is detected by the photodiode. (inspired by Ref. No. 41)

deflection by a factor that depends on the distance, s, of the cantilever to the photodiode and the cantilever length, l: [41]

$$\frac{\Delta d}{\Delta z_c} = \frac{s}{l} \tag{2.39}$$

Where Δd represents the deflection of the laser beam measured on the photodiode (Figure 2.2.1b). This method can achieve a resolution of up to 0.1 Å but the accuracy is usually limited by thermal fluctuations of the cantilever [41, 42].

The photodiode readout serves as an input for a feedback loop that adjusts the cantilever positions and movement according to the operation mode[*] [41].

In this section, the focus is put on force spectroscopy, in particular, on the measurement of the local mechanical properties of soft matter by nano-indentation. In contrast to imaging modes, when the tip scans the surface laterally, in force spectroscopy the tip is moved normal to the surface (z-direction) and the cantilever deflection is recorded as a function of the piezo-position, z_p, or tip-sample distance [44]. Figure 2.2.2 shows a representative example measured on an infinitely hard (not deformable) sample. Here the deflection is represented as the

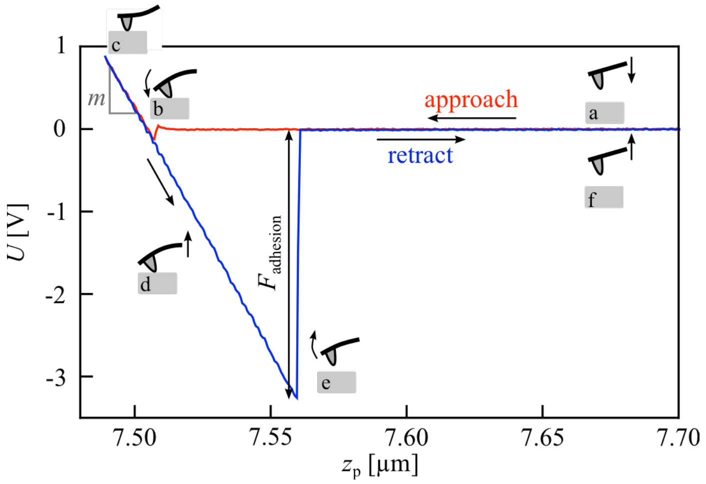

Figure 2.2.2. Photodiode signal as a function of cantilever position (piezo-position) measured on a stiff, non-deformable substrate during approach (red) and retraction (blue) of the tip. a) no tip-sample interaction b) jump into contact due to attractive tip-sample interaction c) further lowering of the cantilever leads to a cantilever deflection but the tip does not indent the sample, d) cantilever is retracted but the tip stays in contact with the substrate due to adhesive forces, e) jump off contact, f) tip is far away from the sample; no tip-sample interactions. The system sensitivity can be obtained from the slope, m, of curves in the contact regime (c-d).

---

[*] The operation modes of AFM can be roughly classified into dynamic and static modes. In the dynamic modes (e.g. amplitude or frequency modulation modes) the cantilever is forced to oscillate at or near the cantilever resonant frequency. Tip-sample interactions are detected via changes in oscillation amplitude or frequency. In contrast, the cantilever does not oscillate in the static operation modes (e.g. contact mode, which also includes force spectroscopy) . (Ref. No. 41)

change in the photodiode signal as a function of z_p. The data consists of an approach part (red) with the tip moving towards the sample surface and a retraction curve (blue) showing the cantilever deflection when the tip is moving away from the surface. Different regimes can be distinguished during a force-spectroscopy cycle [44], which are indicated by the schematics (a-f) in Figure 2.2.2:

- *Region a: non-contact region.* At large distances (micrometers) tip and sample do not interact with each other and the photodiode signal is constant $U = 0$ V [44] (Figure 2.2.2a).
- *Region b: Jump to contact.* When the tip is close to the surface (several nanometers) long-range attractive interactions like van der Waals forces emerge and increase with decreasing distance [42]. When the gradient of these forces overcomes the cantilever spring constant, the tip jumps into contact with the surface [42] (Figure 2.2.2b).
- *Region c: contact region during approach.* Once the tip is in contact with the surface, further downward movement of the cantilever results in its deflection [42] (Figure 2.2.2c).
- *Region d: contact region during retraction.* After reaching a predefined deflection threshold, the tip is retracted from the surface. The cantilever deflection decreases while the tip is still in contact with the sample (Figure 2.2.2d).
- *Region e: Jump off contact.* Adhesion forces keep the tip in contact to the surface so

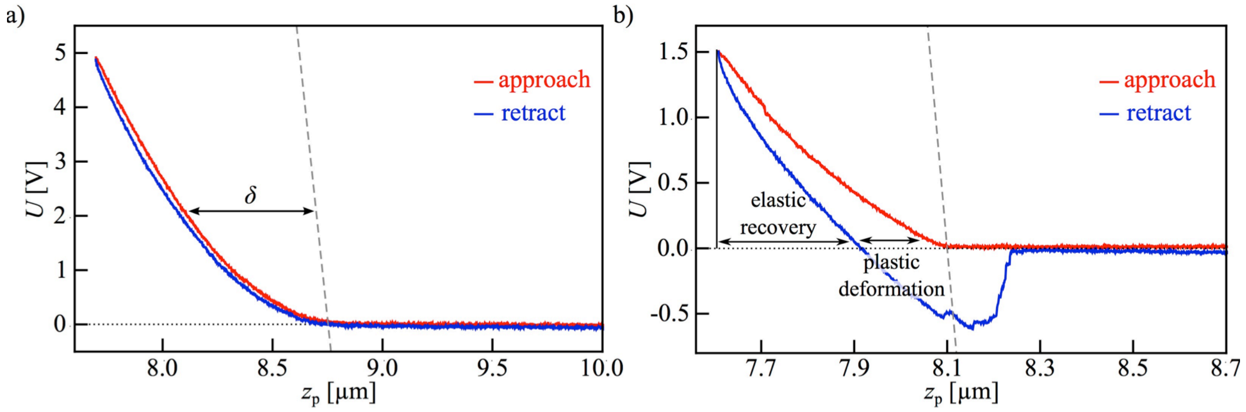

Figure 2.2.3. Nano-indentation of soft materials. Change in photodiode signal as a function of piezo-position measured on hydrogels showing a) nearly pure elastic response: no hysteresis between approach and retraction in the contact regime and b) plastic deformation. The degree of elastic recovery and plastic deformation can be obtained from the indicated regions. The dashed gray line in each panel indicates a deflection-height curve measured on a hard substrate (plastic) using the same cantilever. The indentation depth can be obtained from the difference in piezo-position of the two curves as indicated in panel (a)

that further retraction of the tip results in bending of the cantilever towards the sample surface [44]. When the cantilever spring force overcomes the adhesion forces, the tip jumps off the surface (Figure 2.2.2e).

- *Region f: non-contact region.* Tip and sample do not interact with each other and the photodiode signal is constant [44] (Figure 2.2.2f).

The mechanical properties of the sample can be deduced from the contact region of the approach and retraction curves. When infinitely hard materials are probed, the tip is not able to indent the sample [42]. Assuming that the tip is not deformed, the downward movement of the cantilever in the contact region is directly translated into cantilever deflection, resulting in a linear deflection-height relation (Figure 2.2.2c-d) [42]. Hence, the slope of the linear contact region, m, can be used to determine the system sensitivity $S = 1/m$ (see above) [41].

On the other hand when deformable materials are investigated, the tip indents the sample by an indentation depth δ (Figure 2.2.1b), which results in a non-linear deflection-height relation in the contact regime [42] (Figure 2.2.3). One can distinguish between purely elastic and viscoelastic materials: for purely elastic materials the deformation is reversible, hence retraction and approach curve superimpose [42]. The deflection-height curve of a hydrogel with a nearly pure elastic response is shown in figure 2.2.3a. In contrast, viscoelastic materials can undergo plastic deformation during indentation, which leads to a hysteresis in the contact regime (Figure 2.2.3b). The degree of the plastic deformation can be determined from the area between the approach and retraction curves, while the elastic recovery of the sample is given by the area below the retraction curve indicated in Figure 2.2.3b [42].

The Young's modulus of the sample can be determined from the elastic deformation of the sample in the contact region [42]. Sneddon [45] described the force-indentation relation as follows

$$F = a\delta^b \tag{2.40}$$

Where F is the spring force exerted by the tip and δ is the indentation depth. The exact form of the parameters a and b depends on the tip shape (Table 2.2.1). E^* in table 2.2.1 represents the relative Young's modulus, which depends on both tip and sample properties and is given by [46]:

$$\frac{1}{E^*} = \frac{1-\nu_t^2}{E_t} + \frac{1-\nu_s^2}{E_s} \tag{2.41}$$

With ν representing Poisson's ratio and E corresponding to the Young's modulus. The indices s and t represent of the sample and tip, respectively. When the tip is much harder than the sample, $E_t \gg E_s$, equation 2.41 reduces to

$$\frac{1}{E^*} \approx \frac{1-\nu_s^2}{E_s} \tag{2.42}$$

Thus, the samples Young's modulus can directly be extracted from the constant *a*.

Table 2.2.1. The parameters *a* and *b* of Eq. (2.40) model for common tip geometries.

tip	a	b
Parabolic of radius of curvature R^{+} [46]	$\frac{4\sqrt{R}}{3}E^*$	$^3/_2$
Conical with tip angle 2φ [46, 47]	$\frac{2\tan\varphi}{\pi}E^*$	2
Pyramidal with tip angle 2φ [47, 48]	$\frac{1.4906\tan\varphi}{2}E^*$	2

$^+$ Model also valid for spherical tip of radius R, if the contact radius $\leq R$ [46].

2.3 Langmuir Film Balance: Dilatational Rheology

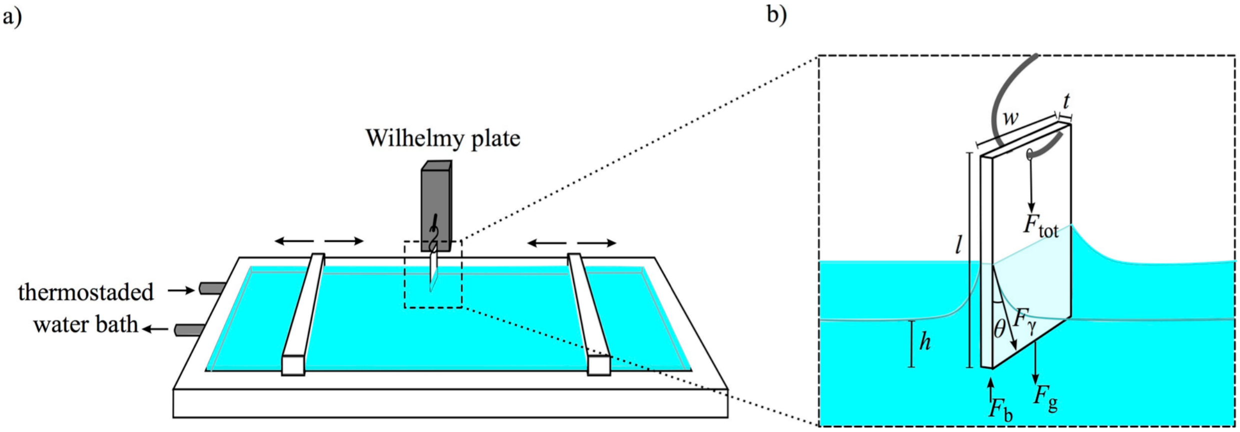

Figure 2.3.1. Schematic representation of a Langmuir film balance. a) The film balance consists of a Teflon trough containing the sub-phase. The surface area is controlled by means of moveable Teflon barriers. Water from a thermostated water bath is circulated through channels below the trough to control the temperature. The surface pressure is measured by b) the Wilhelmy plate method, which measures the vertical pull, F_{tot}, on a thin plate dipped into the sub-phase. The force components are indicated. (inspired by Ref. No. 51)

The Langmuir film balance provides a versatile tool to explore the rheological properties of interfacial systems of soluble and insoluble surfactants like lipids and proteins by applying a dilatational interfacial strain and measuring the change in interfacial tension in response [49].

The Langmuir film balance consists of a trough, which contains the sub-phase (Figure 2.3.1a). For investigations on air/water systems the trough is usually made of Teflon, which prevents the leakage of the aqueous sub-phase due to its high hydrophobicity [50]. The sub-phase temperature is controlled by circulating water from a thermostated bath through channels underneath the Teflon trough [50]. As shown in Figure 2.3.1a, the trough is further equipped with 1 or 2 moveable, motor-driven barriers that allow an accurate variation of the interfacial area A [50].

A common method to measure the surface tension is the Wilhelmy plate method [50]. In this method a thin plate usually made of filter paper or platinum is dipped into the interface [50, 51]. The total force, F_{tot}, acting on the plate in vertical direction is given by

$$F_{tot} = F_g + F_\gamma + F_b \tag{2.43}$$

Here, F_g represents the gravitational force, F_γ is the interfacial tension force and F_b corresponds to the buoyant force [51]. By replacing the exact expressions, equation 2.43 can be written as

$$F_{tot} = \rho_{plate} wtlg + 2(w+t)\gamma\cos\theta - \rho_w wthg \tag{2.44}$$

With w, t and l corresponding to the plate width, thickness and length, respectively [51]. ρ_{plate} represents the mass density of the Wilhelmy plate, g is the gravitational constant of earth, the interfacial tension is given by γ and θ represents the contact angle between the liquid and the plate. h is the depth of immersion, ρ_{w} corresponds to the mass density of the sub-phase, here taken as water (Figure 2.3.1b). In case of complete wetting of the plate $\theta = 0°$ [50]. Hence, variations in the interfacial tension γ can be detected via changes in the vertical pull F_{tot} on the Wilhelmy plate [50, 51]. Changes in surface tension are usually described by the surface pressure π

$$\pi = \gamma_0 - \gamma \tag{2.45}$$

where γ_0 and γ correspond to the surface tension of fluid (water) interface in absence and presence of the surfactant [50, 51].

Viscoelastic properties of interfacial films can be accessed by applying a periodic change in surface area (dilatational strain):

$$A(t) = A_0 \sin(\omega t) \tag{2.46}$$

where A_0 represents the oscillation amplitude, t represents the time and ω corresponds to the oscillation angular frequency [49, 52]. The oscillatory strain results in a periodic response of the surface tension:

$$\gamma = \gamma_0 \sin(\omega t + \varphi) \tag{2.47}$$

The phase shift φ depends on the viscoelastic properties on the monolayer (see section 2.1) [52]. The complex dilatational modulus E can be obtained by (see section 2.1):

$$E = \frac{d\gamma}{dA/A_m} = -\frac{d\pi}{d\ln A} \tag{2.48}$$

where A_m corresponds to the mean surface area [49, 52].

2.4 Grazing Incidence Small Angle X-ray Scattering

Grazing incidence small angle X-ray scattering (GISAXS) is a surface sensitive X-ray scattering technique used to study the morphology of surfaces, interfaces and thin films of hard and soft matter systems [53].

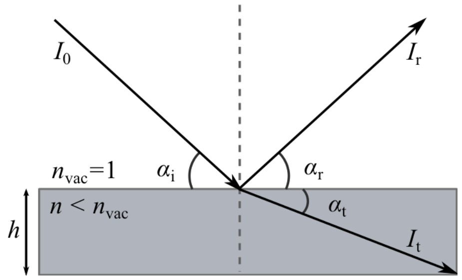

Figure 2.4.1. Reflection/refraction of an X-ray beam at vacuum-material interface. When an X-ray beam with an intensity I_0 impinges the interface at an incident angle α_i, the wave is partially reflected, I_r ($\alpha_\mathrm{r} = \alpha_\mathrm{i}$) and partially transmitted, I_t. For x-ray, the material refractive index $n < 1$ ($n_{vacuum} = 1$), thus the transmitted wave I_t is bent towards the surface $\alpha_\mathrm{t} < \alpha_\mathrm{i}$.

The high surface sensitivity of GISAXS is provided by operating in reflection geometry (in contrast to transmission geometry) [54]. When an X-ray beam of wavelength λ impinges a flat interface, for example between vacuum and bulk material, with an incident angle α_i, reflection and refraction occur at the interface (Figure 2.4.1) [54]. The fraction of the reflected and refracted/transmitted intensities depend on the materials refractive index n ($n_\mathrm{vacuum} = 1$) and the incident angle as described by the Fresnel coefficients:

$$R_f = \frac{I_r}{I_0} = \left|\frac{\sin\alpha_i - \sqrt{n^2 - \cos^2\alpha_i}}{\sin\alpha_i + \sqrt{n^2 - \cos^2\alpha_i}}\right|^2 \tag{2.49}$$

$$T_f = \frac{I_t}{I_0} = \left|\frac{2\sin\alpha_i}{\sin\alpha_i + \sqrt{n^2 - \cos^2\alpha_i}}\right|^2 \tag{2.50}$$

I_0, I_r and I_t represent the intensity of the initial, reflected and transmitted beam, respectively [54]. The reflection/refraction geometry as shown in figure 2.4.1 (note that $n_\mathrm{vacuum} = 1$) is given by the following equations:

$$\alpha_i = \alpha_r \tag{2.51}$$

$$\cos\alpha_i = n\cos\alpha_t \tag{2.52}$$

Where α_r and α_t correspond to the angle of the reflected and transmitted waves, respectively [54]. In case of X-rays the refractive index of a material is given by [55]:

$$n = 1 - \delta - i\beta \tag{2.53}$$

δ and β correspond to the dispersion and absorption terms of the X-ray-material interaction at a wavelength λ [54, 56]:

$$\delta = \frac{\lambda^2 \rho N_A r_e}{2\pi} \frac{\sum_i (Z_i - f_i')}{M} \tag{2.54}$$

$$\beta = \frac{\lambda^2 \rho N_A r_e}{2\pi} \frac{\sum_i f_i''}{M} \tag{2.55}$$

With ρ as the mass density, M the molar mass, N_A the Avogadro number, Z_i the atomic number of the i-th atom and the classical electron radius $r_e = (2.82\times10^{-15})$ m [56]. f_i' and f_i'' are the dispersion corrections [57]. δ and β are positive values and typically in the range of $\delta \approx 10^{-5}$ and $\beta \approx 10^{-6}$, leading to refractive indices $n < 1$ [54, 55]. Hence, according to Snell's law (Eq. 2.52), when the X-ray beam impinges on the vacuum-material interface at α_i, the refracted beam is bend towards the surface $\alpha_t < \alpha_i$ (Figure 2.4.1) [55]. Moreover, a critical incident angle exists below which the beam is totally reflected [55]. This critical angle of total external reflection can be calculated as [54, 55]:

$$\alpha_c = \sqrt{2\delta} \tag{2.56}$$

The critical angle of total external reflection is usually in the order of $\alpha_c \approx 0.1° - 0.5°$ [54, 55].

In GISAXS experiments a monochromatic X-ray beam with a wave vector $|\vec{k}_i| = 2\pi/\lambda$ impinges the surface at a very shallow angle $\alpha_i < 1$ usually close to the critical angle of total external reflection α_c [53]. At $\alpha_i < \alpha_c$, an evanescent wave is formed at the interface, which decays exponentially beneath the surface [55]. As the penetration depth of the evanescent field

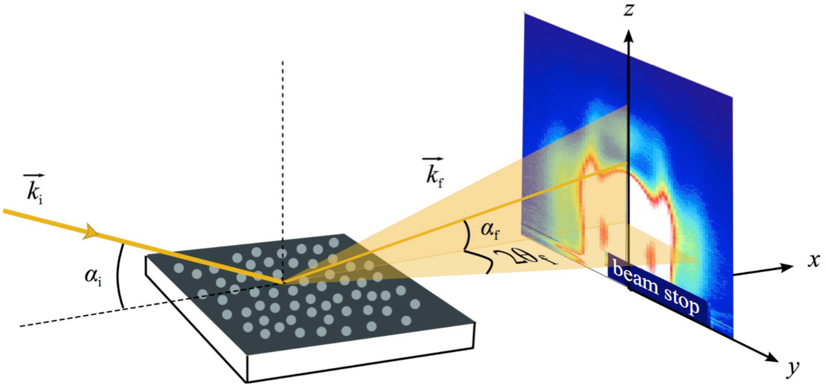

Figure 2.4.2. Experimental geometry of GISAXS. A monochromatic X-ray beam impinges the sample surface at an incident angle α_i. Electron density fluctuations at the interface scatter the incident beam. The scattered intensity is often detected by a 2D- detector. Since the intensity of the scattered beam is weak, a beam stop is used to block the more intense e direct and specular beam.

is in the order of a few nanometers, this scattering geometry provides maximum surface sensitivity [54, 55]. If electron density fluctuations occur at the surface, for example due the presence of nano-particles, the incident beam is scattered in a direction described by scattered wave vector $\vec{k}_\mathrm{f}$ [55]. Since the inelastic scattering is negligible as such shallow incident angles $|\vec{k}_\mathrm{f}| = |\vec{k}_\mathrm{i}| = 2\pi/\lambda$. Hence, the wave vector transfer $\vec{q}$ can be calculated by:

$$\vec{q} = \vec{k}_f - \vec{k}_i = \frac{2\pi}{\lambda}\begin{pmatrix} \cos\alpha_f \cos 2\theta_f - \cos\alpha_i \\ \cos\alpha_f \sin 2\theta_f \\ \sin\alpha_f + \sin\alpha_i \end{pmatrix} \tag{2.57}$$

where α_c and $2\theta_\mathrm{f}$ represent the out-of-plane and in-plane scattering angles, respectively (Figure 2.4.2.) [55]. The scattering waves are often collected by a 2D-detector. The obtained scattering pattern depends on the sample morphology. The surface or interface morphology i.e. shape, size and lateral order of the nano-particles is reflected by the in-plane component of the intensity profile $I(q_{\|})$,[*] which is given by the equation:

$$I(q_{\|}) = A \cdot |F(q_{\|})|^2 S(q_{\|}) \tag{2.58}$$

where A is a constant, $F(q_{\|})$ and $S(q_{\|})$ correspond to the form and structure factor, respectively [55].

2.4.1 Form Factor

The shape and size of the nano-particles at the interface are described by form factor $F(q)$.

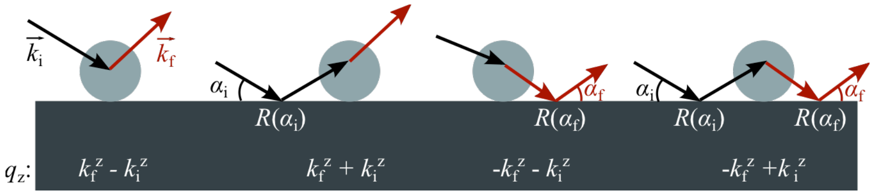

Figure 2.4.3. Refraction/reflection terms considered in the Distorted Wave Born Approximation. The beam before and after scattering is indicated in black and red, respectively. The resulting out-of-plane wave vector transfer is shown below each refraction/reflection term. The simple refraction event shown at the outermost left side corresponds to the Born approximation. $R_\mathrm{f}(\alpha)$ represents the corresponding Fresnel reflection coefficient. (inspired by Ref. No. 58)

Within the framework of the Born approximation, when multiple scattering is neglected, the form factor corresponds to the Fourier transform of the particles shape function integrated over the particles volume V:

---

[*] The intensity profile along q_z mirrors the structural order perpendicular to the surface (Ref. No. 55). But in this section the focus is put on the characterization of surface morphologies and only the in-plane scattering intensity $I(q_{\|})$ is considered.

$$F(\vec{q}) = \int_V \rho(\vec{r}) e^{-i\vec{r}\cdot\vec{q}}\, dV \tag{2.59}$$

where $\rho(\vec{r})$ is the electron density at position $\vec{r}$ [54, 57]. In GISAXS experiments when small incident and scattering angles are of interest, the Born approximation is not valid [58]. Multiple scattering events are accounted for by application of the Distorted Wave Born Approximation (DWBA). Within the framework of DWBA, the full scattering process is represented by the sum of four processes shown in figure 2.4.3. The form factor is thereafter given by [58]:

$$\begin{aligned} F\left(q_{\parallel}, k_i^z, k_f^z\right) = {} & F\left(q_{\parallel}, k_f^z - k_i^z\right) \\ & + R(\alpha_i) F\left(q_{\parallel}, k_f^z + k_i^z\right) \\ & + R\left(\alpha_f\right) F\left(q_{\parallel}, -k_f^z - k_i^z\right) \\ & + R(\alpha_i) R\left(\alpha_f\right) F\left(q_{\parallel}, -k_f^z + k_i^z\right) \end{aligned} \tag{2.60}$$

The first term corresponds to the simple refraction of the incident beam by a particle as in the Born approximation [53]. The remaining three processes that include additional reflection of incident and/or refracted beam are weighted by the corresponding Fresnel reflection coefficients $R(\alpha_x)$ ($x = i, f$) (eq. 2.49).

2.4.2 Structure factor

When very dilute systems of nano-particles are studied, the interference of the waves scattered by individual particles is negligible [54, 55]. In this case the scattering pattern is related to the form factor only [55]. But at high surface densities the scattering pattern is also governed by the interference of the scattered waves [54]. This interference depends on size and shape distribution of the nano-objects, their structural organization as well as possible coupling between particle type and position [55].

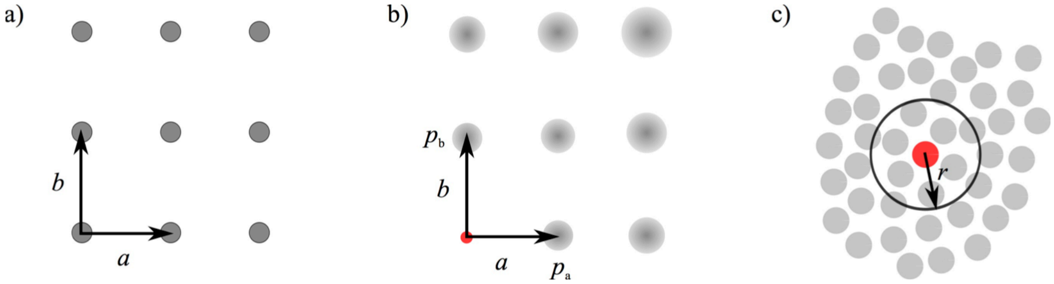

Figure 2.4.4. Schematic representation of a) crystal: the structure is described by the lattice basis vectors $\vec{a}$ and $\vec{b}$, b) paracrystal: p_a and p_b, respectively represent the probability of having a particle at a distance a or b from the red particle. The gray circles correspond to regions with highest probability. b) disordered structure: the mutual arrangement is described by the pair correlation functions. (inspired by Ref. No. 58)

The spatial arrangement of the objects is considered by the interference function $S(q)$ also called structure factor. Three cases can be distinguished: highly ordered lattices, paracrystals and disordered structures [58].

In case of a highly ordered periodic structure as in perfect crystals, the lateral order is described by the lattice basis vectors $\vec{a}$ and $\vec{b}$ (Figure 2.4.4a) [58]. The structure factor can be described using the corresponding reciprocal lattice vectors [58]

$$\overrightarrow{a^*} = 2\pi \frac{\vec{b}\times\vec{n}}{\vec{a}\cdot[\vec{b}\times\vec{n}]} \qquad \overrightarrow{b^*} = 2\pi \frac{\vec{a}\times\vec{n}}{\vec{b}\cdot[\vec{a}\times\vec{n}]} \tag{2.61}$$

Here $\vec{n}$ corresponds to the surface normal and × represents the vector product.

A partial disorder is introduced into the system in the paracrystal model. Here the long-range order is destroyed gradually and in a probabilistic way [58]. The structure is described by the distance probability $p(x)$ between two neighboring particles (Figure 2.4.4b) [58]. This model provides a link between the highly ordered lattice and the disordered system [58].

In the disordered structure the mutual arrangement of the particles is described by a pair correlation function (Figure 2.4.4c) [58]. The structure factor is given by

$$S(q_{\|}) = 1 + \varrho \int (g_{\alpha\beta}(r_{\|}) - 1)\, e^{-ir_{\|}\cdot q_{\|}} dr_{\|} \tag{2.62}$$

With $g_{\alpha\beta}(r_{\|})$ as the partial pair correlation function and ϱ corresponds to the particle surface density [55].

2.4.3 Coupling Between Form and Structure Factor

According to eq. (2.63) the exact calculation of the structure factor requires the knowledge of all $g_{\alpha\beta}(r_{\|})$, which is usually not the case. Hence, some models have been introduced to approximate $g_{\alpha\beta}(r_{\|})$ considering possible coupling between particle type, i.e. size and shape, and position [55].

The Decoupling Approximation (DA) is the simplest approximation, assuming that particle type and position are not correlated [58]. Thereafter, the lateral arrangement of the particles can be described solely by the relative position of the particles [58]. Hence, the partial pair correlation function in eq. (2.62) is replaced by a general correlation function $g_{\alpha\beta}(r_{\|}) = g(r_{\|})$ (Figure 2.4.5a) [55, 58].

The Local Monodisperse Approximation (LMA) partially accounts for the coupling between particle type and position by assuming that the particle ensemble consists of monodisperse domains (Figure 2.4.5b) [57].

The Size-Spacing Correlation Approximation (SSCA) is a one dimensional model that considers a correlation between particle sizes and the distance between them (Figure 2.4.5.c)[55,59].

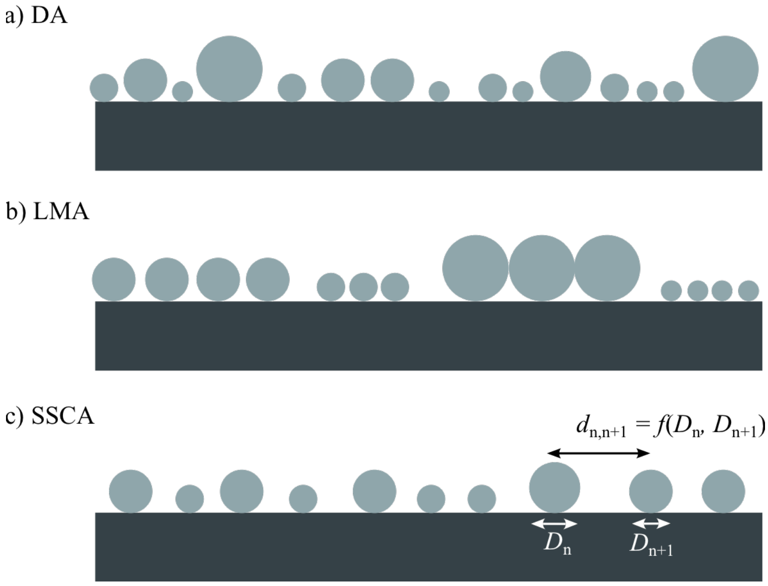

Figure 2.4.5 Schematic representation of a) the decoupling approximation, b) the local monodisperse approximation and c) the Size-Spacing Correlation Approximation. (inspired by Ref. Nos. 53, 59)

Chapter3

Spatio-Temporal Evolution of Mechanical Patterns in Extracellular Matrix of Hydra

The extracellular matrix (ECM) is a unique non-cellular component of animal tissue [14]. Besides providing mechanical stability, the ECM also plays an important role in the regulation of cell function, which is not only mediated via chemical cues like soluble growth factors or cell receptor ligands [14]; the mechanical properties of the ECM strongly influence stem cell migration, proliferation and differentiation strongly as has been demonstrated by extensive *in vitro* studies [5, 9, 12, 60, 61]. Accordingly, each organ has a unique ECM, which is dynamically remodeled and adapted to the tissue requirements during growth and development or in the course of diseases [14]. Abnormally high ECM stiffness has, for example, been reported in fibrotic human lungs [13]. However, little is known about the mutual regulation of local mechanical properties of ECM and stem cell behavior during development of living organisms. In this chapter the freshwater polyp Hydra is used as an ancient and simple model to study stem cell functions in order to explore the mechanical properties of the native ECM, so called mesoglea, *ex vivo* during maturation and development.

3.1 Introduction: The Freshwater Polyp Hydra

The freshwater polyp Hydra has a simple sack-like body column flanked by tentacles surrounding a mouth opening at the apical tip and a foot process at the basal end (Figure 3.1.1.a) [62]. The body wall consists of two cell layers, an outer ectodermal and an inner endodermal cell layer, that sandwich an intervening sheet of extracellular matrix, called mesoglea (Figure 3.1.1a) [62]. Cell process holes in mesoglea allow cell-cell contacts between endo- and ectodermal layers [63].

Hydra's cell population comprises three specific stem cell lineages, which continuously undergo cell division in the body column: i) the ectodermal and ii) endodermal epithelial-muscular stem cells as well as iii) the interstitial stem cell lineage [64-66]. The steady gain in tissue caused by the continuous division of the stem cells results in a constant tissue movement towards the oral and aboral ends of the body (Figure 3.1.2 left panel), where the tissue is eventually sloughed off at the mouth, end of tentacles and basal disc [67, 68]. However the progressive growth of tissue is most effectively compensated by incorporating the tissue into new evaginating buds during the asexual reproduction of Hydra polyps (Figure 3.1.1a) [67, 68]. The extensive recruitment of tissue from the parental Hydra results in a rapid grow of the bud in size during the early stages of the budding process (~ 24 h), which is also considered as the fast growing phase [20, 69]. A simplified scheme of the budding process is shown in figure 3.1.2.

As a member of the ancient phylum *cnidarian,* Hydra is considered to bear one of the earliest forms of extracellular matrices in evolution [62]. However, its molecular composition shows a high degree of similarity to vertebrate ECM; heparan sulfate proteoglycans, laminin and fibronectin-like molecules as well as fibrillar (type I and II) and non-fibrillar (type IV) collagens are examples of mesoglea core ingredients [62]. Spatial confinement of these components has lent Hydra mesoglea a trilaminar structure: two thin sub-epithelial zones, basal laminae, containing collagen type IV and laminin sandwich a central fibrous zone, the interstitial matrix which is crossed by a grid of collagen type I, Hcol-I, fibrils (Figure 3.1.1b) [63]. Accordingly, Hydra's mesoglea combines two major ECM functions, which are separated in higher animals: 1) mechanical support, which is provided by the connective tissue with its collagenous fibers and 2) cell-cell communication usually mediated by the

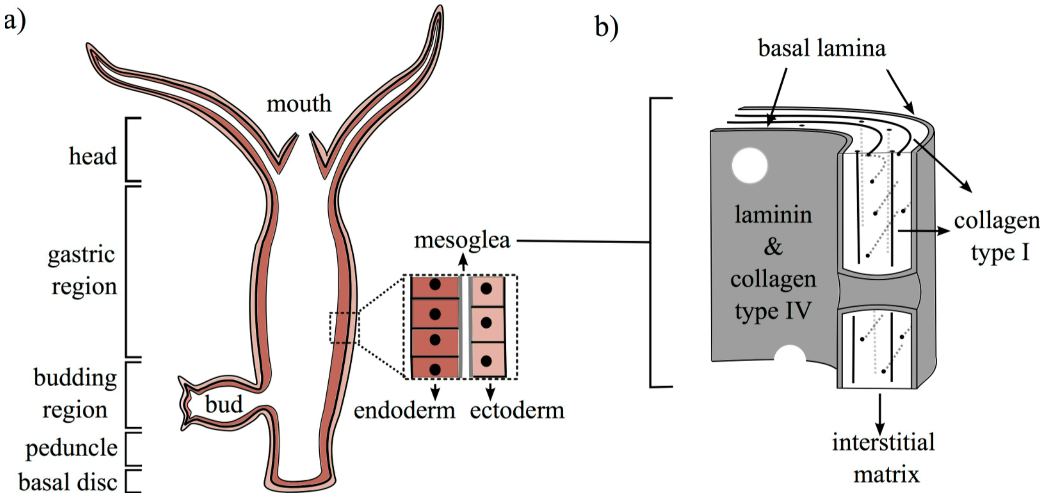

Figure 3.1.1. Schematic representation of Hydra body plan. a) Hydra has a sack-like body comprising a mouth opening and tentacles at the apical and a foot process at the basal end. The body column can be divided into 5 regions as indicated. The body wall consist of two cell layers, ecto- and endoderm, and an intervening sheet of extracellular matrix, mesoglea. b) Hydra mesoglea has a multilayered structure: Two sub-epithelial basal laminae, containing laminin and collagen type IV, sandwich the interstitial matrix, which is crossed by collagen type I fibers. Holes inside mesoglea allow for cell-cell contact between the two ecto- and endodermal cell layers.

basal lamina.

Being the most abundant fibrillar collagen in mesoglea of Hydra, the type I collagen Hcol-I [62] can be considered as a key determinant of mesogleal mechanical strength. Hcol-I is a polypeptide of 1412 amino acids that assembles into homotrimers [70]. Similar to vertebrate collagen type I, Hcol-I consists of a triple helical domain of 340 Gly-X-Y repeats, flanked by a C-terminal propeptide and a N-terminal propeptide-like domain [70]. However, Hcol-I exhibits a less extensive cross-linking compared to its vertebrate homologue, which is ascribed to a lower proline content, lack of typical lysine cross-linking sites as well as altered post-translational processing [70]. These unique features of Hcol-I makes hydra mesoglea highly flexible so that it can be stretched reversibly by a factor of 7-8 along the main body axis without rupturing [71, 72]. This high degree of flexibility perfectly supports the dynamic contractions and extensions of the Hydra polyp in combination with its hydro-gastrovascular system [73].

Besides providing mechanical support, mesoglea also plays a crucial role in cell differentiation, morphogenesis as well as regeneration processes [74-76]. Mesoglea is continuously remodeled and modified spatially and temporally throughout Hydra lifetime: for example, Hausman and Burnett reported that the mesoglea fiber system disintegrated in the gastric region when the feeding regime was increased from two to five times weekly [77], which

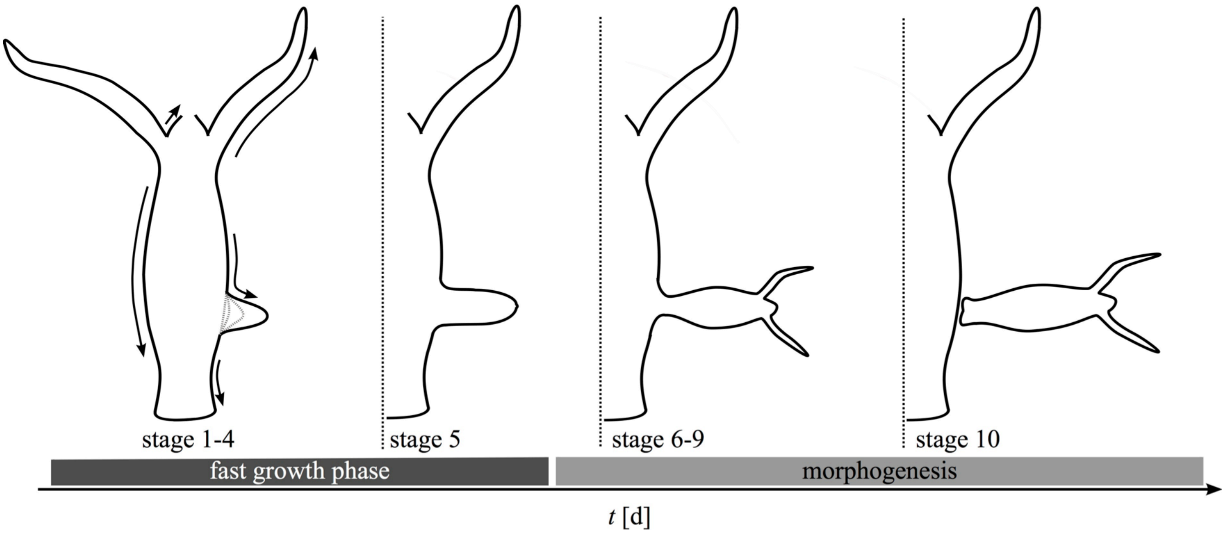

Figure 3.1.2. Schematic representation of tissue movement and budding in hydra. Hydra tissue is continuously displaced along the body column towards the apical and basal ends (left panel, arrows indicate direction of movement) or is incorporated into new developing buds. During the early stages of bud formation (stages 1-5), also called the fast growing phase, the bud grows rapidly in size by recruiting cells and mesoglea from the parent. Later developmental stages (stages 6-10) are marked by tissue morphogenesis. At stage 10 the bud is fully matured and only loosely attached to the parent. The Budding process takes ~ 3 d. Bud stages according to Otto and Campbel (Ref. No. 20)

could be correlated to the onset of budding [77, 78]. A more recent study demonstrated that mesoglea was displaced along the Hydra body column together with the two cell layers within the scope of the continuous tissue movement [21]. Moreover, mesoglea was reported to expand or contract when passing different regions of the body [21]. If mesoglea was incorporated into a new bud, it was rigorously stretched and thinned in the evaginating bud during the fast growing phase so that is became almost invisible to light microscopy [21]. On the other hand, the mesoglea structure was reestablished and resembled the parental mesoglea at later developmental stages [21]. These drastic morphological changes suggest that mesoglea is mechanically modified during hydra morphogenesis. Nevertheless, there have been no quantitative studies on the biophysical properties of mesoglea in relation to growth and development.

The main thrust of this chapter is to shed quantitative light on mesoscopic structure and mechanical properties of Hydra mesoglea. Moreover, by tracking the spatio-temporal changes of mesoglea mechanics during morphogenesis the ECM stiffness is correlated to morphogenesis and the stem cell activity.

3.2 Results and Discussion

3.2.1 Mesoscopic Structure of Hydra Mesoglea

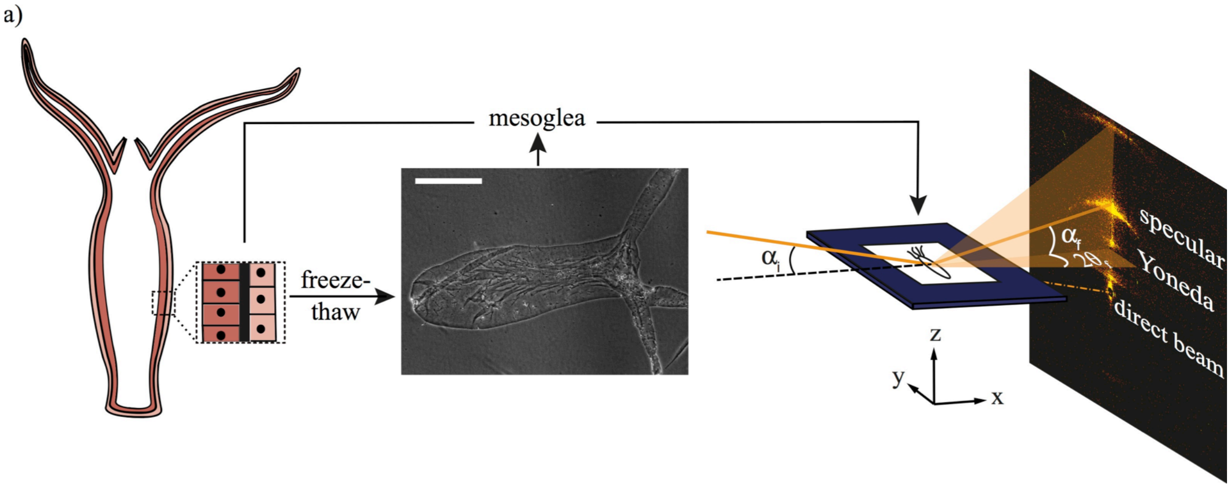

Figure 3.2.1. Nano-focused GISAXS of Hydra mesoglea: experimental setup. Hydra mesoglea (phase contrast microscopy image in middle panel, Scale bar 500 µm) was isolated by a freeze-thaw process and placed on a silicon nitride window (right panel). A monochromatic, nano-focused X-ray beam (orange line) impinged the mesoglea at a grazing incidence angle α_i*. The scattered intensity was detected by a 2D-detector.*

The mesoscopic structure of Hydra mesoglea was investigated by grazing incidence small-angle X-ray scattering (GISAXS) using a monochromatic X-ray beam with a diameter of 200 nm. This technique, called “nano-GISAXS” [79], provided a beam footprint much smaller than an isolated Hydra mesoglea this technique and allowed for scanning the mesoglea in different directions. The experimental procedure is depicted schematically in figure 3.2.1. Ecto- and endodermal cells were removed from mesoglea by freeze-thawing and subsequent mechanical shearing (section 3.4.2). The mesoglea sustained its structural integrity throughout the isolation procedure and exhibited all morphological features of the Hydra polyp e.g. tentacles, buds, etc. as shown in figure 3.2.1 (middle panel). Isolated mesogleas were placed on a silicon nitride membrane and subjected to the nano-focused X-ray beam, which impinged on mesoglea at an incident angle of $\alpha_i = 0.46°$ beyond the critical angle of total external reflection ($\alpha_c = 0.14°$ for silicon nitride). The mesoglea was examined in directions parallel and perpendicular to the oral-aboral axis. In both directions several scattering patterns were obtained showing one or more arcs arranged concentrically around the direct beam, accompanied by additional satellite peaks located on the arcs (Appendix III). Two representative patterns obtained with the beam parallel (left) and perpendicular (right) to the OA-axis are shown in Figure 3.2.2. The obtained patterns indicate the presence of rod-like objects with a highly ordered, crystalline-like packing aligned parallel to the substrate surface. The white grid overlaid on each pattern represents the reconstructed reciprocal lattice and shows that the fibers 1) have a distorted hexagonal packing order and 2) are anisotropically arranged with respect to the OA-axis: parallel to the main body axis the calculated real lattice parameters correspond to $a_{\parallel} = (17.6 \pm 3.6)$ nm, $b_{\parallel} = (6.7 \pm 0.8)$ nm and $\gamma_{\parallel} = (97.1 \pm 2.4)°$, while perpendicular to the OA-axis $a_{\perp} = (11.8 \pm 0.5)$ nm, $b_{\perp} = (4.3 \pm 0.4)$ nm and $\gamma_{\perp} = (100.3 \pm 9.3)°$ were obtained (Figure 3.2.2c, left and middle panel). As type I collagen is the most abundant fibrillar compartment of mesoglea [62], these patterns can be ascribed to the packing order of Hcol-I fibers. A comparison to vertebrate type I collagen from rat-tail tendon [80, 81] (Figure 3.2.2c, right panel) shows that the packing order of collagen type I in Hydra is comparable to its vertebrate homologue. The slight distortion observed in the packing of Hcol-I fibers refers to a weaker intermolecular interaction in comparison to the vertebrate type I collagen, which is in good agreement with previous predictions based on the molecular structure of Hcol-I [70] as described in section 3.1. These finding is further supported by former electron microscopy studies showing that Hcol-I tends to form a network of thin fibrils rather than thick, banded fibers [70, 73].

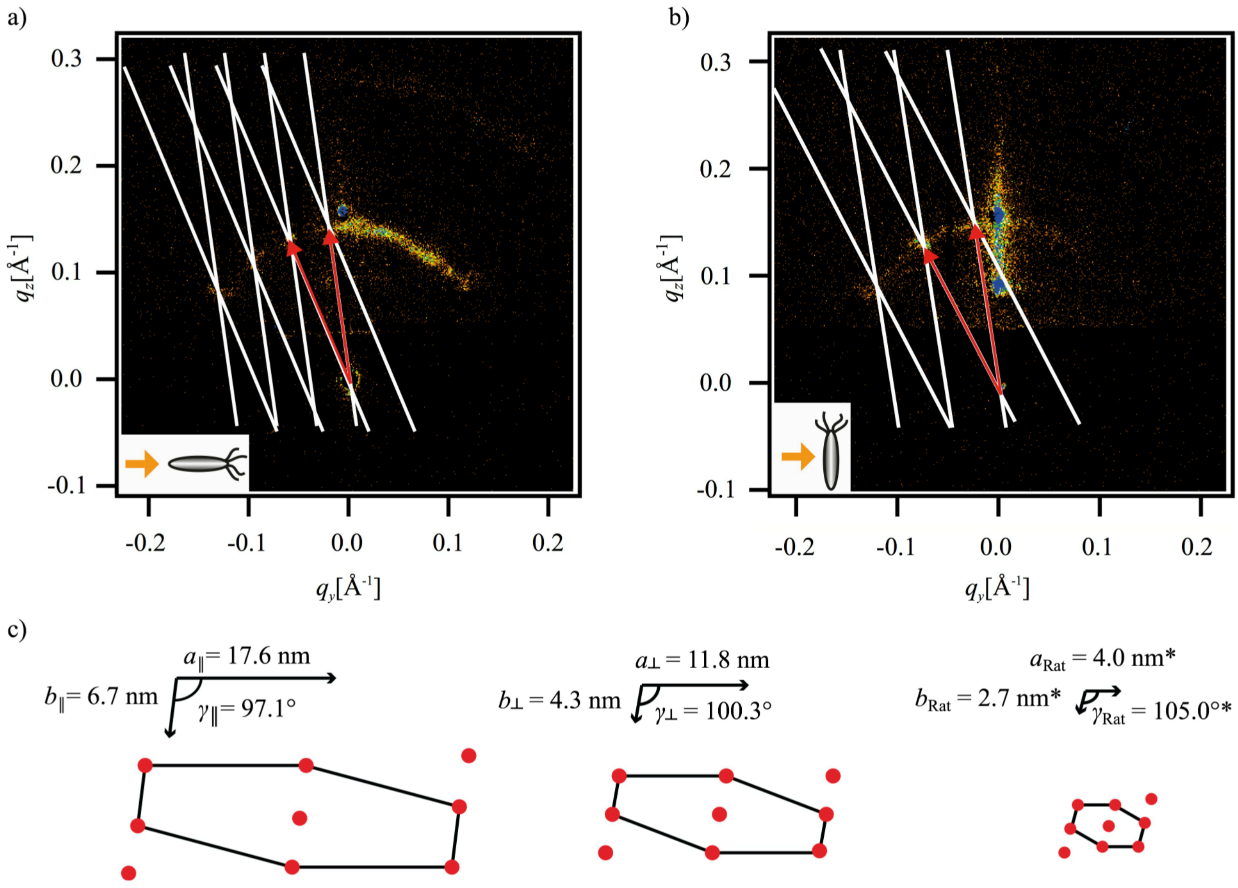

Figure 3.2.2. Nano-GISAXS of isolated Hydra mesoglea. Scattering patterns obtained with the beam a) parallel and b) perpendicular to main body axis. The white grid represents the reciprocal lattice with the lattice vectors indicated in red. c) Lattice parameters (a, b, γ) *in real space calculated from scattering pattern obtained with beam (left) parallel and (middle) perpendicular to main body axis. The right panel shows the lattice parameters of vertebrate collagen type I from rat-tail tendon for comparison. The real lattices are represented schematically in the bottom line. (*Ref. No. 80)*

Shimizu et al. [63] showed that Hcol-I fibers are aligned in two distinct directions in mesoglea: one set of fibers runs parallel to the OA-axis, while the others encircle the body column and are perpendicular to the first group [63]. Accordingly, the scattering patterns obtained parallel and perpendicular to the body axis might be assigned to the packing order of the parallel and circumferential Hcol-I fibers, respectively. In this regard, the poorer order of the fibers aligned along the OA-axis can be related to the extensive stretching and contractions of the hydra polyp along this axis. Thereafter, the anisotropy in packing order of the fibrillar proteins might reflect an intrinsic body design of Hydra, which supports the dynamic movements of the body column.

3.2.2 Mechanical Properties of Hydra Mesoglea

Hydra mesoglea was probed along the OA-axis by means of nano-indentation using an AFM. For this purpose, mesogleas were allowed to dry after isolation in order to collapse the hollow ECM tube and facilitate the nano-indentation. The drying time was found to influence the overall elastic modulus; the values rose on average from 30 kPa to 170 kPa by increasing the drying time from a few hours to 2 days (Figure 3.2.1). All values mentioned hereinafter refer to over-night dried mesogleas.

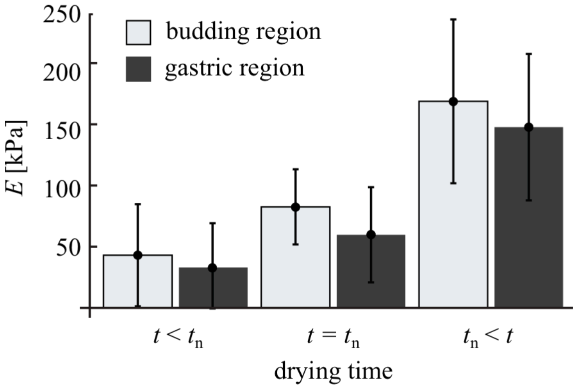

Figure 3.2.1. Influence of drying time on elastic modulus of budding and gastric region of isolated mesoglea. t_n *corresponds to over night drying. The elastic modulus increased with increasing drying time.*

To obtain reproducible and statistically reliable measurements a synchronized Hydra culture with a daily feeding regime was established and used for experiments. This allowed, first, the accurate determination of sample history and second, eliminated possible fluctuations associated with starvation periods.

Mesoglea Elasticity Patterns

By measuring the local elasticity along the OA-axis and as a function of the indentation position, elasticity maps could be constructed for several mesogleas obtained from Hydras at different ages and developmental stages. The elasticity maps were standardize by normalizing the indentation positions, measured from mesoglea foot, by the body column length to obtain the relative position *d* (Figure 3.2.2). Using this approach allowed the direct comparison of different elasticity maps regardless of individual size differences by defining specific regions along the body column with regard to *d*:

a) $0.0 \leq d < 0.1$: peduncle region
b) $0.1 \leq d \leq 0.3$: budding region, which included the bud junction at $d = 0.22 \pm 0.05$ (average over 9 samples)
c) $0.6 \leq d \leq 1.0$: gastric region.

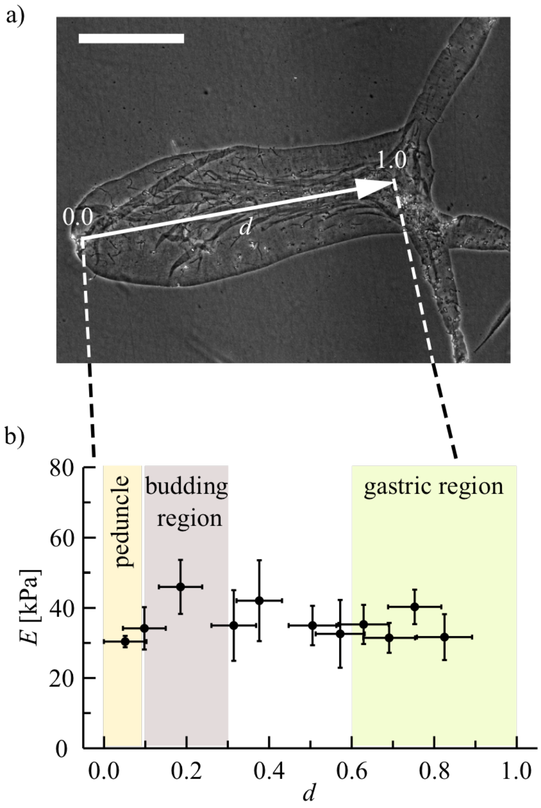

Figure 3.2.2. Constructing the elasticity map of Hydra mesoglea. a) Phase contrast microscopy image of an isolated Hydra mesoglea. Scale bar corresponds to 500 µm. The local elastic moduli were measured along the main body axis as indicated by the white arrow to obtain b) elasticity map of an isolated mesoglea. Young's modulus is plotted against the relative position d. Depending on d three regions were defined along the body column: peduncle, budding and gastric region.

A total number of $n = 38$ mesogleas were examined. The obtained elasticity maps could be categorized into three main groups (Figure 3.2.3a-c):

a) Type A: mesoglea was uniformly elastic along the entire body column showing an average elastic modulus of $\langle E\rangle$= 40-90 kPa. (Figure 3.2.3a)
b) Type B: mesoglea was soft in the gastric region with elastic moduli $\langle E\rangle \geq$ 15 kPa and stiff in the lower body (peduncle and budding region) with $\langle E\rangle \leq$ 120 kPa. (Figure 3.2.3b)
c) Type C: mesoglea was, similar to type B, soft in the gastric and stiff in the budding region. But the elastic modulus decreases to $\langle E\rangle \geq$ 40 kP towards the foot, $d = 0.0$. (Figure 3.2.3c)

A schematic overlay out of 9 samples in provided in figure 3.2.3d.

In order to classify the elasticity maps in an objective and reproducible manner a simple and straightforward algorithm was developed. Briefly, the elastic moduli of gastric and peduncle region were normalized by the modulus of the budding region. These ratios ($\langle E_{\text{gastric}}\rangle/\langle E_{\text{budding}}\rangle$ and ($\langle E_{\text{peduncle}}\rangle/\langle E_{\text{budding}}\rangle$) were used as criteria for identification of the pattern as A, B or C as described in detail in section 3.3.4. This algorithm allowed the classification of elasticity maps irrespective of individual differences in overall mesoglea stiffness and thus irrespective of the drying time. According to this procedure the majority (66%) of investigated mesoglea showed a type A pattern. Within remaining mesogleas type B (18%) and type C (13%) patterns were observed at almost equal fractions*.

The observed elasticity patterns show some correlations to fiber patterns previously observed in mesoglea of Hydras by Hausman and Burnett [77, 78]. They reported that young and non-budding Hydras had a fiber system homogenously developed throughout the body column, which correlates well with the uniformly elastic type A pattern [78]. On the other hand, polyps with young buds exhibited a well-developed fiber system extending from the foot to the bud junction but lacked a fiber net in the gastric region. This fiber pattern seems to correlates with type B and C phenotypes obtained in this section [78]. Leontovich et al. [76] reported a high level of metalloproteases in the foot, which describes the low elastic modulus observed in the vicinity of the foot ($d \rightarrow 0.0$) in type C patterns (Figure 3.2.3c) (see below).

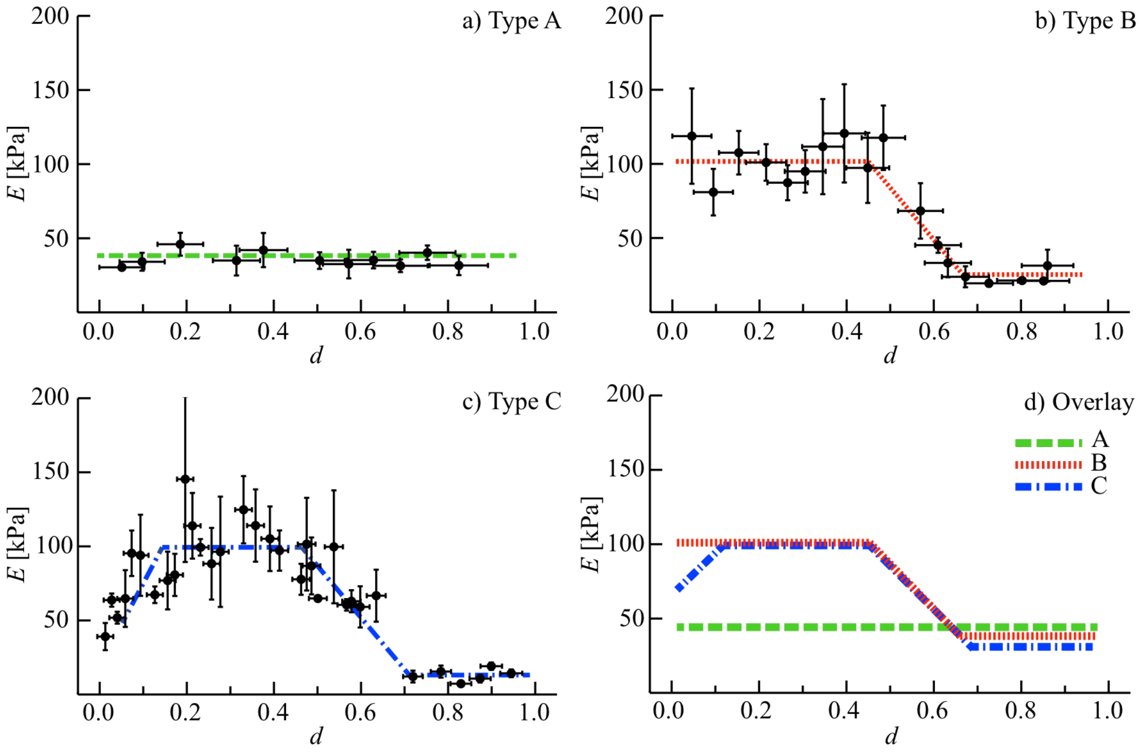

Figure 3.2.3. Classification of representative mesoglea elasticity maps. a) Type A: uniformly low elasticity along the body column. b) Type B: mesoglea is soft in the gastric region but shows high elastic moduli in the lower body. c) Type C: mesoglea shows maximum elastic modulus in the budding region $0.1 \leq d \leq 0.3$*. d) Schematic overlay of the three elasticity patterns. Each curve is an average over 2-4 samples.*

---

* One map could not be clearly identified as type B or C due to lack of data in the peduncle region

Mechanical Patterning of Mesoglea and Bud Formation

The correlation of individual mesoglea elasticity patterns with the characteristic fiber patterns of non-budding or budding Hydras observed in previous studies [77, 78] suggests that the mechanical patterning of mesoglea is closely related to the budding process. Therefore, the elasticity maps were sorted as a function of Hydra's age. Young hydras tended to start budding within ~ 3 days after the detachment from their parental polyp[*]. Hence, in order to track mesoglea patterning during the transition from matured, freshly detached buds towards budding polyps of the next generation, the elasticity pattern distribution was studied for mesogleas of up to 3 days old hydras, the age class containing the first sample with 2 buds (Figure 3.2.4):

- *Age = 0 d*: freshly detached buds exhibited exclusively type A elasticity patterns (100%) i.e. uniformly soft mesoglea along the body column ($n = 5$)
- *Age = 2 d*: 2 days after the detachment from parental Hydra the fraction of type A decreased to 40%, type B (40%) and C (20%) appeared ($n = 5$).
- *Age = 3 d*: The 3 days old Hydra population showed only a minor fraction of type A mesogleas (14%) while type B and C patterns were widely spread ($n = 7$).

The gradual shift in the elasticity pattern distribution from type A in freshly detached buds toward type B and C in 3 days old Hydras, indicates that the maturation of young hydras is strongly correlated with a stiffening of mesoglea in the presumptive budding zone.

Remarkably, when the tissue is displaced into a new bud during the early stages of budding, the cells slide over the mesoglea of the budding zone into the new forming body axis [21]. In

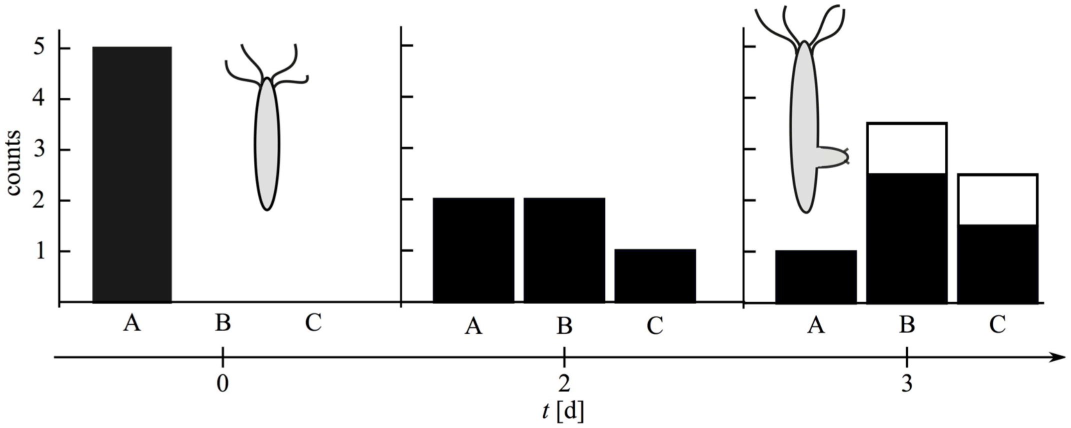

Figure 3.2.4 Elasticity pattern distribution as a function of age. Young, freshly detached polyps (t = 0 d) show a uniformly elastic mesoglea. By time type B/C patterns appear. At t = 3 d the majority of polyps show type B/C elasticity patterns. Black: Hydras with no apparent buds. White: hydras with buds at stage 3 or higher.

---

[*] See Appendix III for budding probability.

contrast, cells and mesoglea move together in the gastric region [21]. These observations suggest some correlation between the changes in mesoglea elasticity and the migratory behavior of the cells. In fact, it has been shown that High substrate stiffness promotes both single cell and collective tissue movements [4, 60, 82]. Hence, the stiffening of mesoglea in the budding region might facilitate the required cell movement from the parental Hydra into the new forming bud during the early fast growing phase of bud formation.

Mesoglea Proteomics

The mechanical patterning of mesoglea can be conducted either by a differential expression of ECM core proteins along the body column or by posttranslational modifications. To identify the underlying mechanism, a comparative quantitative proteomic analysis of mesoglea was performed using the method of stable isotope labeling with amino acids in cell culture (SILAC) [83] (in collaboration with Dr. H. O. Petersen, Laboratory of Prof. T. W. Holstein, Centre for Organismal Studies, University of Heidelberg). This method is based on the metabolic incorporation of stable heavy isotope labeled amino acids (^{13}C-lysine) into Hydra

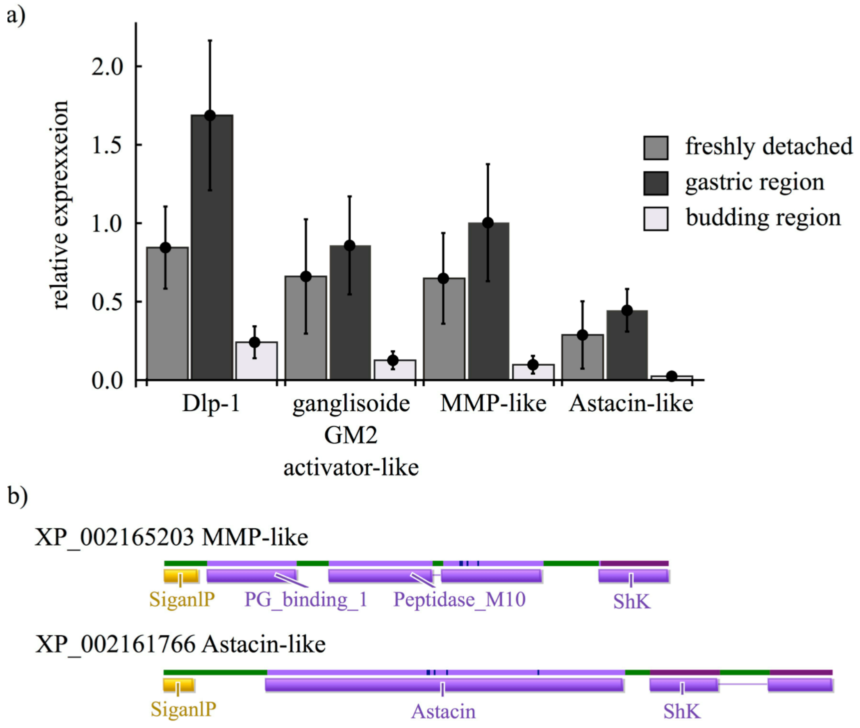

Figure 3.2.5 Mesoglea proteome analysis. (A) Protein expression differences in the mesoglea were analyzed between the gastric (dark grey) and budding (middle grey) region of mature animals and between the mesoglea of freshly detached animals. Multiple sample ANOVA analysis, using a p-value threshold of 0.05, revealed significant expression differences of four proteins between the samples. Among these, two are extracellular proteases (MMP-like and astacin-like proteases). (b) Domain structure of the differentially expressed proteases.

proteins. Control samples from SILAC Hydras are then used as an internal standard to detected differences in protein expressions by mass spectrometry [84].

The mesoglea from a) freshly detached buds was compared to the mesoglea of b) gastric and c) budding region of three days old polyps. Isolated mesoglea from SILAC Hydra containing all developmental stages was used as internal control. The Quantitative analysis revealed that the three samples did not differ in the compositions of mesoglea core proteins. However, four proteins were significantly up-regulated in freshly detached buds and the gastric region of three days old Hydras: 1) Dickkopf-like protein 1 (Dlp-1), an extracellular protein, which is known to be gradually expressed along the OA-axis [85, 86], 2) a ganglioside activator GM2-like protein and two matrix proteases i.e. 3) a metalloprotease and 4) an astacin-like protease (Figure 3.2.5).

The differential expression of the two proteases correlates well with the observed mechanical patterns: both are strongly abundant in the soft mesoglea of freshly detached buds and the gastric region of 3 days old hydras but show a low level in the stiff budding region of the 3 days old polyps. The results indicate that mechanical patterning of mesoglea is not due to a spatial change in expression of ECM core proteins but is rather conducted by a posttranslational processing of ECM proteins. This finding is in accord with the emergence of low stiffness in the foot of type C patterns due to the reported high level of metalloproteinase in this region [76], as already described above.

Mesoglea Mechanics and β-Catenin Signaling

How the mechanical modification of mesoglea is regulated on the molecular level is still unclear. The budding in hydras is closely related to the Wnt/β-catenin signaling (canonical Wnt-pathway), which plays a central role in the axial patterning and formation of the head organizer in Hydra [87]. In young non-budding Hydras, β-catenin (Hyβ-cat) is expressed at a low level throughout the body column. Prior to bud formation, the Hyβ-cat is significantly up regulated in a ring-like domain in the presumptive budding region [87]. This change in spatial expression is reminiscent of the transition from a uniformly elastic type A mesoglea to type B and C during maturation of young Hydras and implies a direct correlation between Hyβ-cat expression and matrix stiffness. Moreover, matrix metalloproteinases (MMP) are known to be regulated in a Wnt dependent manner [88-90], suggesting Wnt/β-catenin as a possible candidate for regulation of mesoglea mechanics. Therefore, in the next step the influence of Hyβ-cat on mechanical properties of mesoglea was investigated by 1) inducing an increase of β-catenin level by treating Hydras with alsterpaullone (Alp), which activateds the Wnt-signalling pathway and 2) investigating the mesoglea mechanics of β-catenin overexpressing mutants.

1) Impact of alsterpaullone treatment on mesoglea mechanics: Alsterpaullone is a specific glycogen synthase kinase 3 beta, GSK-3, inhibitor [91]. In the canonical Wnt-pathway, GSK-3 is part of a β-catenin destruction complex, which, in the absence of Wnt, targets cytoplasmic β-catenin for degradation [92] (Figure 3.2.6a). By inhibiting GSK-3, Alp prevents the β-catenin degradation and leads to its accumulation in the cytoplasm; β-catenin is then trans-located into the nucleus where it functions as a transcriptional co-activator [92] (Figure 3.2.6a). Hence, Alp-treatment of Hydra increases the β-catenin level and activates the Wnt signaling along

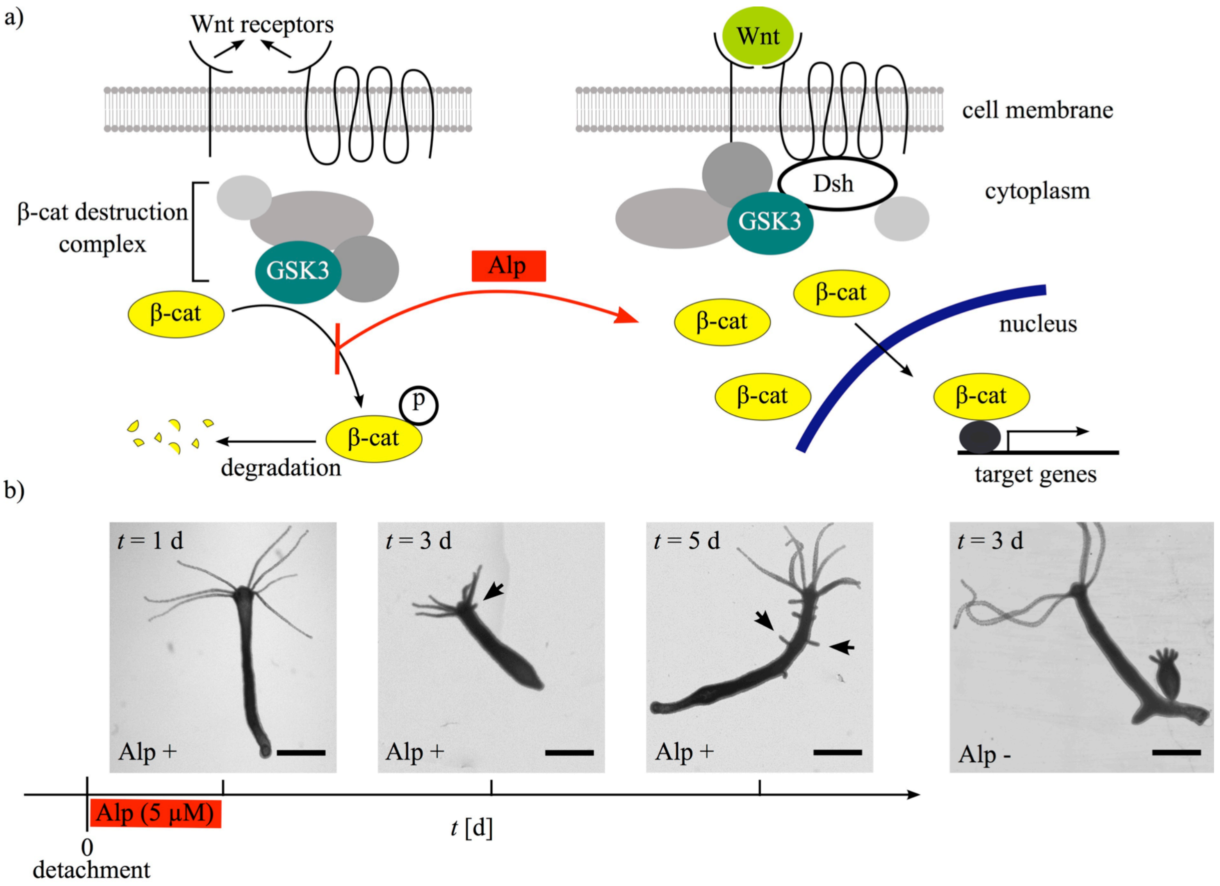

Figure 3.2.6. Activation of Wnt-signaling by Alp-treatment. a) Simplified scheme of the canonical Wnt-pathway (inspired by Ref. No. 92). In the absence of Wnt, cytoplasmic β-catenin is targeted for degradation by the β-catenin destruction complex (left panel). The binding of Wnt to the extracellular part of the receptor complex (right panel) deactivates the destruction complex via the Dishevelled protein (Dsh) leading to an accumulation of β-catenin and finally the activation of its target genes. A similar effect is achieved by Alp treatment, which specifically inhibits GSK3, a member of the destruction complex. b) Alp-treatment of Hydras. Freshly detached hydras were treated with Alp for 24h (red bar) and subsequently transferred to Hydra medium. 3 days after the detachment, first rudiments of ectopic tentacles were observed (arrows). At t = 5 d the body column was covered by several ectopic tentacles. An image of an untreated 3 days old polyp is shown for comparison (outermost left panel). Scale bars correspond to 1 mm.

the body column, which leads to an increases head activation potential and formation of ectopic tentacles along the body column [93] (Figure 3.2.6b).

To study the impact of an increased level of Hyβ-cat, young polyps were treated with Alp (5 µM) for 24 h immediately after detachment from parental Hydra (Figure 3.2.6b). Elasticity maps were recorded from mesogleas of a) 1 day old polyps, i.e. directly after the Alp-treatment, b) 3 days old Alp-treated Hydras ($t = 3$ d) and c) 5 days old polyps ($t = 5$ d), i.e. 4 days after Alp-treatment. The first group ($t = 1$ d) showed no significant morphological abnormalities. First rudiments of ectopic tentacles were observed at $t = 3$ d, whereas the body column of 5 days old Alp-polyps was covered by several ectopic tentacles (Figure 3.2.6b).

Two elasticity patterns were identified: 1) the uniformly elastic type A pattern and 2) a novel type of pattern with low and almost uniform elastic modulus $\langle E \rangle \approx 35^{*}$ kPa in the upper body extending into the budding region. The elastic modulus increased towards the foot reaching $\langle E \rangle \approx 60$ kPa at $d = 0.0$ (Figure 3.2.7a). This pattern is referred to as type Alp. No type B or C patterns were obtained. Figure 3.2.7b shows a schematic overlay of Alp-type with type A, B and C patterns obtained before. The fraction of Alp-type mesogleas increased by time. While immediately after Alp-treatment ($t = 1$ d), Alp-treated Hydras showed mainly (4 out of 5 samples) type A elasticity patterns, at $t = 3$ and 5 days the majority of polyps (5 out of 6 samples for both age groups) exhibited an Alp-type mesoglea.[†]

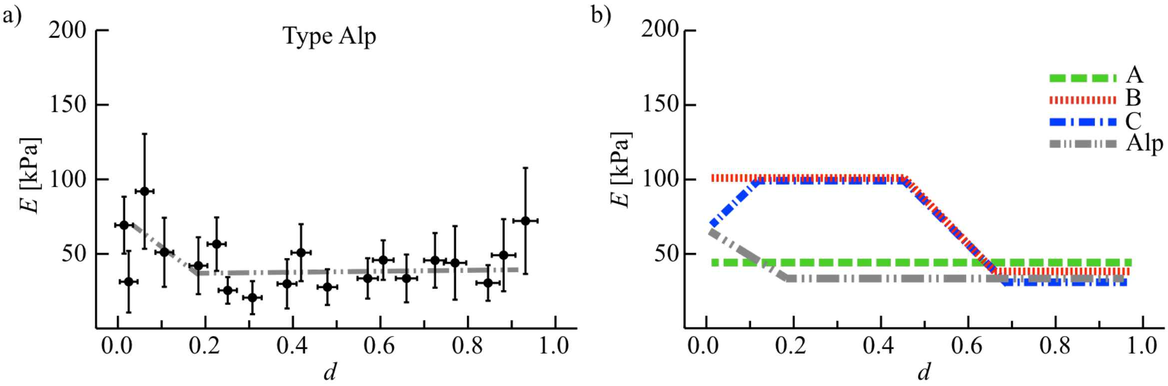

Figure 3.2.7. Mesoglea elasticity of Alp-treated Hydras. a) representative elasticity pattern of a hydra 2 days after Alp treatment (age = 3 d). b) Schematic overlay of wild-type and Alp-type mesoglea elasticity patterns. Each curve corresponds to an average of 2-5 independent elasticity maps.

---

[*] The values correspond to an average of 4-5 elasticity patterns.

[†] The temporal evolution of the mean elastic moduli is shown in Appendix III

2) Mesoglea mechanics of β-catenin overexpressing mutants [94, 95]: the higher level of β-catenin in the epithelial cells endows the body column tissue with high head organizer capacity, which results in the formation of heads and secondary body axes along the body column[94] (Figure 3.2.8a).

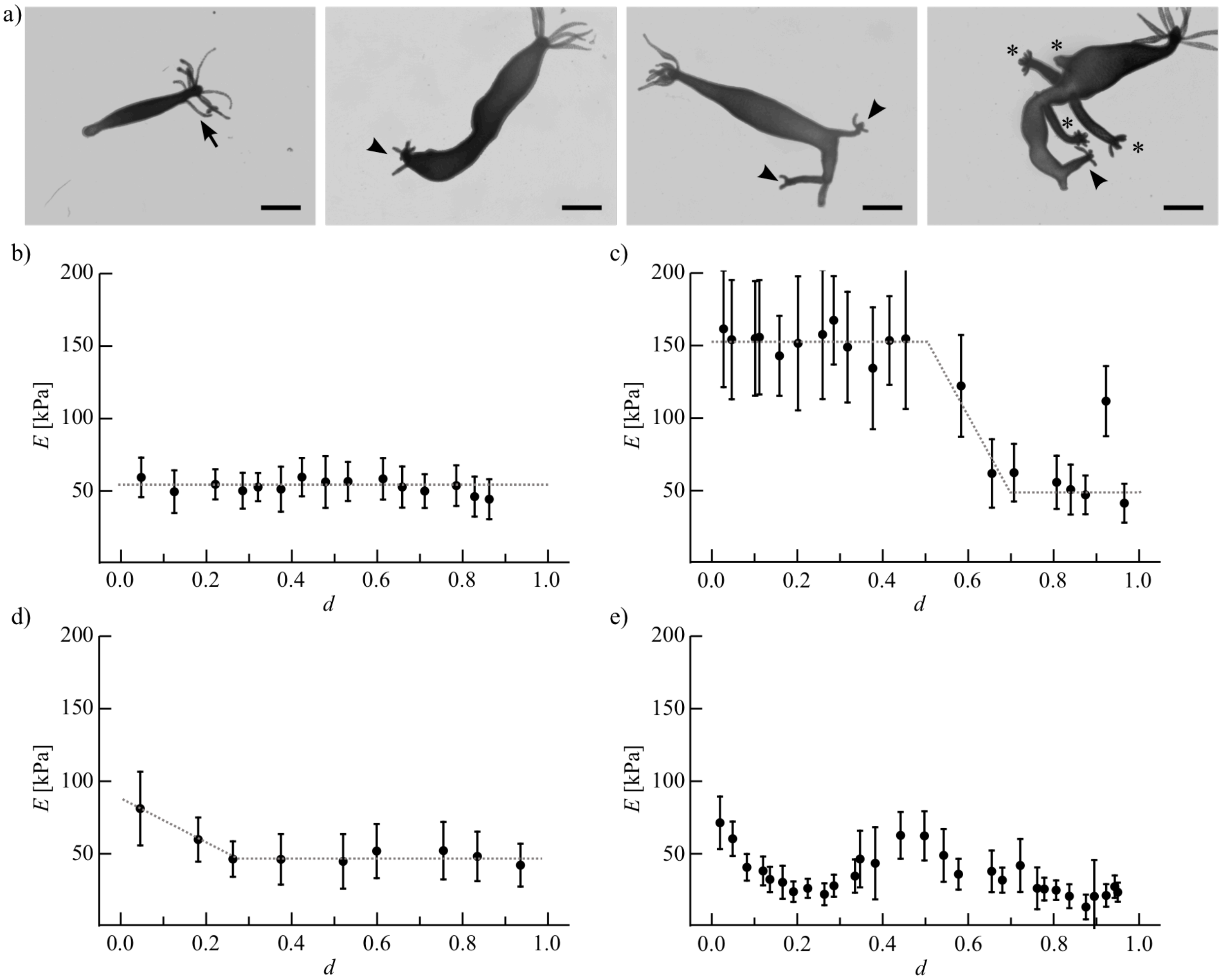

Figure 3.2.8. Genetically modified β-catenin overexpressing hydras. a) Representative microscopy images of β-catenin hydras. β-cat mutants show a broad diversity of morphological phenotypes. The higher head activation potential results in formation of ectopic tentacles (arrows) and secondary body axes (arrow head). Buds are indicated by asterisks (lower right panel). Scale bar corresponds to 1 mm. β-cat mutants also showed a large variety of mesoglea elasticity maps including b) Type A, c) Type B, d) Type Alp but also e) novel elasticity patterns.

To study the evolution of mesoglea mechanics, a daily fed synchronized culture of β-cat Hydras was established as described in section 3.4.1. Elasticity maps were recorded for up to 8 days old β-cat Hydras (n = 27). The results revealed a large variety of patterns: besides type A, B and type Alp also novel patterns were observed (Figure 3.2.8b-e). No simple correlation between age or morphological phenotypes and the elasticity patterns could be identified. The wide variety of mesoglea mechanical patterns can be attributed to the broad morphological diversity. It should also be considered that differential in Hyβ-cat expression levels along the body axis as well as between individual samples [94] might also influence the mechanical properties of mesoglea. In this regard, in order to compare β-cat Hydras with Alp-treated animals, the elastic moduli were averaged over all phenotypes. The results revealed tendency very similar to type Alp patterns (Figure 3.2.9). [*]

The results show that increasing the β-catenin level in epithelia cells significantly affected the mechanical properties of mesoglea and led to the emergence of new mechanical patterns. In contrast to wild-type Hydras, Alp-treated polyps showed no sign of mesoglea stiffening in the presumptive budding zone by time (up to 5 days after the detachment). Instead the Alp-type elasticity pattern was marked by a low elastic modulus extending from the gastric region into the budding zone. If the β-catenin expression level was directly correlated to mesoglea stiffness, as suggested in the last section, a uniform increase in elastic modulus along the body column would have been observed in Alp-treated and β-cat mutants. Nevertheless, the significant change in the elasticity pattern compared to wild-type polyps suggests at least an indirect correlation of mesoglea mechanical patterning with Wnt/β-catenin signaling.

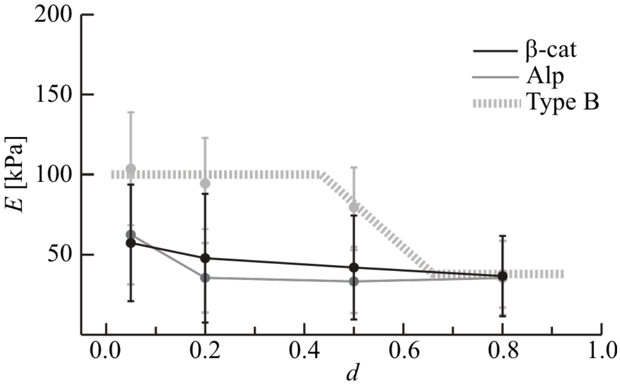

Figure 3.2.9. Average elastic modulus along the body column of β-catenin overexpressing Hydras (black). Although β-catenin overexpressing Hydras showed a broad variety of elasticity patterns in consent with a large phenotype diversity, the average elastic moduli (n = 27) over 8 days compare well with those of Alp-type Hydras (gray). Type B elasticity pattern obtained for wild-type Hydras is shown by dashed gray line for comparison. Each data point represents the mean elastic modulus over the following regions: peduncle ($0 \leq d < 0.1$), budding region ($0.1 \leq d \leq 0.3$), center ($0.4 \leq d < 0.6$) and gastric region ($0.6 \leq d \leq 1.0$).

Moreover, the migratory behavior of the cells at the base of tentacles is similar to that observed in the budding zone during the early stages of bud formation; i.e. cells slide over the mesoglea into the tentacles [21]. Hence, if the increased stiffness in budding region of wild-type polyps would, as implied before, solely reflect the mechanical requirements for tissue

---

[*] See Appendix III for the temporal evolution of the elastic moduli.

evagination, tentacle base tissue should show high elastic moduli similar to the budding zone. But generation of tentacle base tissue in the body column by Alp-treatment led to a softening of mesoglea in the body column.

It is remarkable that the region of high mesoglea stiffness correlates with the region of high stem cell activity and proliferation [96]. Both epithelial and interstitial stem cell lineages in this region continuously divide and give rise to several differential products i.e. neuronal, gland and germ cell precursors [64, 96]. By comparison the soft upper gastric region is characterized by a strict turning off stem cell renewal of both stem cell lineages [64, 96]. Thus, a main function of the differential matrix stiffness might be the regulation of the differential stem cell activity in combination with various cues from different signaling molecules such as BMP [97, 98] (bone morphogenetic protein).

3.3 Summary

The extracellular matrix (ECM) of the freshwater polyp Hydra, called mesoglea, is considered as one of the earliest extracellular matrices in evolution. Besides providing structural support, mesoglea also plays an important role in regeneration and morphogenesis of hydra polyps and is dynamically remodeled during hydra lifetime. But there has been no quantitative study on the interplay between the biophysical properties of mesoglea and Hydra's stem cell behavior during growth and development.

In this chapter, the mesoscopic structural order of an intact isolated Hydra-ECM was investigated in directions parallel and perpendicular to the oral-aboral axis (OA-axis) using nano-focused grazing incidence small-angle X-ray scattering (nano-focused GISAXS). The results revealed that fibrillar proteins in Hydra mesoglea take a highly ordered, crystalline-like packing with a distorted hexagonal lattice, which was attributed to Hydra collagen type I (Hcol-I). The packing order of the fibers was comparable to vertebrate type I collagen from rat-tail tendon. The ordering of the Hcol-I fibers was anisotropic with respect to the OA-axis with lattice parameters $a_{\parallel} = (17.6 \pm 3.6)$ nm, $b_{\parallel} = (6.7 \pm 0.8)$ nm and $\gamma_{\parallel} = (97.1 \pm 2.4)°$ parallel and $a_{\perp} = (11.8 \pm 0.5)$ nm, $b_{\perp} = (4.3 \pm 0.4)$ nm and $\gamma_{\perp} = (100.3 \pm 9.3)°$ perpendicular to the OA-axis, which supports the extensive contractions and extensions of the body column along the OA-axis.

In the next step, Hydra mesoglea was probed along the OA-axis with regard to its mechanical properties by means of nano-indentation using an atomic force microscope (AFM). By measuring the local elastic moduli as a function of relative distance from the foot, standardized elasticity maps were constructed for several mesogleas. Three distinct elasticity patterns were identified along the OA-axis. Time resolved experiments using a synchronized Hydra culture showed that polyps freshly detached from parental Hydra exhibit a uniformly soft ($E = 40$-90 kPa) mesoglea. By time mesoglea is softened in the upper gastric region ($E \geq 15$ kPa), but stiffened in the middle and lower body, corresponding to the budding zone and foot ($E \leq 120$ kPa). Comparison to protein expression obtained by a quantitative proteome analysis showed that the mechanical modification of mesoglea is realized by significant changes in protease expression profile along the OA-axis. These mechanical changes were found to be closely related to the onset of the asexual reproduction via bud formation. Moreover, the region of high ECM stiffness correlated with the region of high stem cell activity.

Therefor, the body column tissue was transformed into head tissue to see how the altered cell behavior affects the ECM mechanics. For this purpose impact of an increase in β-catenin level, a key component in formation of the head organizer, on the mechanical patterning of mesoglea was investigated by 1) treating Hydras with alsterpaullone, a specific GSK3-β inhibitor and 2) using β-catenin overexpressing mutants. The results revealed significantly altered elasticity patterns: the mesoglea exhibited low elastic moduli in the upper and middle body (gastric and budding region) ($\langle E\rangle \approx 35$ kPa), which increased slightly towards the foot ($\langle E\rangle \approx 60$ kPa). Hence, transforming the body column tissue into head tissue resulted in a softening of the underlying ECM. The results are consistent with a model suggesting that high ECM stiffness facilitates high stem cell activity.

3.4 Materials and Methods

3.4.1 Animal Culture

Hydra culturing

Hydra *magnipapillata* and *β*-catenin overexpressing Hydra *vulgaris* were cultured in modified Hydra medium [99] (1.0 mM $CaCl_2$, 1.0 mM Tris-HCl, 1.0 mM $NaHCO_3$, 0.1 mM KCl, 0.1 mM $MgCl_2$, pH = 7.4) and kept at (18±0.5)°C. Animals were fed daily with freshly hatched *Artemia* and cleaned a few hours after feeding. (Chemicals were purchased from Carl Roth, Karlsruhe, Germany)

Culture synchronization

Hydras with buds at different developmental stages were collected from a culturing box, which was fed for at least 2-3 weeks on a daily regime and transferred to 24-well-plates (1

Hydra/ well). The new culture of collected hydras was kept on a daily feeding regime further on and checked for newly detached buds twice per day. To obtain a synchronized culture the freshly detached buds were collected and transferred to new 24-well-plates (1 Hydra/ well). The day of detachment served as zero time point for age determination.

3.4.2 Mesoglea Isolation

Single mesoglea isolation for GISAXS and AFM studies

1 day starved Hydras were transferred to a 2 ml test tube with Hydra medium (1 Hydra per tube). Hydra medium was replaced by 1.5 ml of a 0.5% w/v solution of N-Lauroylsarcosine sodium salt (Sigma Aldrich, St. Louis, United States) in water. The sample was immersed in in liquid nitrogen for 10 min. Frozen Hydras were either used directly or stored at -80 °C. To extract the mesoglea, Hydras were transferred to distilled water after thawing and forced through a Pasteur pipette 20 to 40 times. The washing water was exchanged 3 times. Subsequently the isolated mesoglea was transported to a dry petri dish with a drop of water and allowed to dry at room temperature and ambient pressure. All elastic moduli mentioned in this study refer to over-night dried mesogleas. Budding stages were determined prior to freezing and according to Otto and Campbell [20].

Mass mesoglea isolation for proteome analysis

Large numbers of mesogleas were isolated by a modification of the method used by Shostak et al. [100]. In order to inhibit proteolytic degradation during isolation, protease inhibitor cocktail tablets (cOpmlete Ultra tablets, mini, *EASYpack*, Roche, Basel, Switzerland) were used according to the procedure protocol provided by the supplier. Pellets of 90-150 frozen Hydras were transferred to protease inhibitor cocktail and allowed to thaw at room temperature. After thawing, Hydras were transferred to a glass test tube with 3-4 ml protease inhibitor cocktail and cells were removed by successive pipetting using a Pasteur pipette. To prevent the mesogleas from sticking to the glass bottom 1-2 ml of an 80% sucrose solution were gently injected below the suspension. The mixture was then centrifuged at 300g for 5 min using a swing-out bucket rotor at 4°C. After centrifugation mesogleas were collected from the sucrose-water interface. The procedure was repeated 7-10 times.

3.4.3 Nano-Focused GISAXS

Experimental procedure

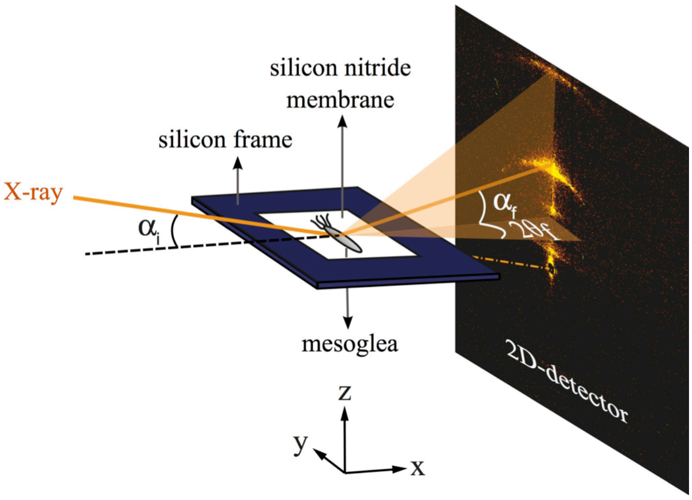

Figure 3.4.1. Experimental setup of nano-GISAXS. Isolated Hydra mesoglea was placed on a silicon nitride membrane supported by a silicon frame. The X-ray beam hit the sample at a grazing incident angle α_i *beyond the critical angle of total external reflection. The scattered intensity at each position defined by the exit angles* ($2\theta_f$, α_f) *was detected by a two-dimensional pixel-detector.*

Nano-GISAXS Experiments were performed at the European Synchrotron Radiation Facility (ESRF) beamline ID13 (Grenoble, France). Single isolated mesoglea was deposited on a 100 nm thick silicon nitride window surrounded by a silicon frame (SPI supplier, West Chester, United States) 2-3 days before experiments (Figure 3.4.1). Experiments were performed on dehydrated samples and at ambient temperature and ambient pressure. Mesogleas were probed with a 200 nm beam with a wavelength of 0.81 Å (15.3 keV) and at an incident angle of $\alpha_i = 0.46°$. Data was collected with a 2D-detector (Maxipix, ESRF, France) [101]. Silver behenate was used for calibration.

Data analysis

The scattering patterns obtained for silver behenate were used for spatial calibration of the 2D-detector readouts [102]. The wave vector transfer in parallel, q_y, and perpendicular, q_z, directions were obtained by:

$$q_y = \frac{2\pi}{\lambda}\left[\cos(\alpha_f)\sin(2\theta_f)\right] \tag{3.1}$$

$$q_z = \frac{2\pi}{\lambda}\left[\sin(\alpha_f) + \sin(\alpha_i)\right] \tag{3.2}$$

where λ is the wavelength, α_i is the incident angle, α_f and $2\theta_f$ correspond to the in- and out-of-plane scattering angles, respectively (Figure 3.4.1) (see section 2.4). Since the scattering patterns showed arcs concentrically arranged around the direct beam, the axes origin was set at the direct beam position. After background subtraction and deadtime correction [101], satellite peak positions were determined using 2D-gaussian fit in order to obtain the reciprocal lattice vectors $\overrightarrow{a^*}$ and $\overrightarrow{b^*}$ (Figure 3.4.2). The error was estimated as the half width at half maximum. The angle γ^* between $\overrightarrow{a^*}$ and $\overrightarrow{b^*}$ was determined from the dot product

$$\cos\gamma^* = \frac{\overrightarrow{a^*}\cdot\overrightarrow{b^*}}{|\overrightarrow{a^*}||\overrightarrow{b^*}|} \tag{3.3}$$

The real space lattice parameters were then derived from following relations:

$$\gamma = \pi - \gamma^* \tag{3.4}$$

$$\vec{a}\cdot\overrightarrow{a^*} = 2\pi \tag{3.5}$$

$$\vec{b}\cdot\overrightarrow{b^*} = 2\pi \tag{3.6}$$

The third dimension lattice vector in reciprocal space, which is infinitesimally large, was assumed to be perpendicular to the a^*b^*-plane.

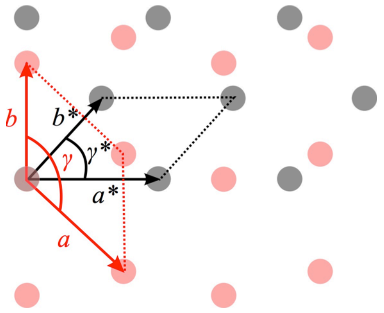

Figure 3.4.2. Reciprocal and real space lattice. The reciprocal lattice is schematically illustrated by light gray dots. The reciprocal lattice parameters (a^*, b^*, γ^**) are obtained from the scattering pattern. Red dots show the real lattice represented by the lattice parameters (*a, b, γ*) shown in red. The corresponding unit cells are indicated with dashed lines.*

3.4.4 Nano-Indentation of Hydra Mesoglea

Experimental procedure

Nano-indentation was performed utilizing a JPK-Nanowizard atomic force microscope (JPK Instruments, Berlin, Germany) mounted on a Zeiss Axiovert 200 microscope (Zeiss, Oberkochen, Germany). Silicon nitride cantilevers with a nominal spring constant of 10 mN/m and tip-radius of 20 nm were used (MLCT-Probes purchased from Bruker, Billerica United States). Indentation experiments were carried out in 150 mM sodium chloride solution. The spring constant of each cantilever was determined prior to measurements using the thermal noise method. A total number of n = 38 Hydras out of a daily fed synchronized culture were examined. Sampled Hydras were between 0 and 10 days old and bore no more than 3 buds. Depending on the size each mesoglea was indented at 7-37 different positions along the body column. indentation was performed with a speed of 2-6 µm/s and up to a cantilever deflection of 0.8 V relative to the baseline. At each position along the Hydra body axis 4 points with a distance of 5 µm were indented. Each spot was indented two times. Subsequent measurements at the same spot with a standard deviation larger than 10% were discarded. Local elastic moduli at each position on measoglea were determined by averaging over the 8 measurements. Data points with standard deviation larger than 40% were discarded. The relative measurement position was determined using ImageJ [103].

Data analysis

The obtained deflection-height curves were analyzed using the Bilodeau model for a pyramidal tip [48]. The force, *F*, is given by

$$F = a * \delta^2 \tag{3.7}$$

The parameter a corresponds to

$$a = \frac{1.4906 \cdot E \cdot \tan\varphi}{2(1-\mu^2)} \tag{3.8}$$

where, *E* represents the sample's Young's modulus, φ is the half opening angle of cantilever tip. For the asymmetric quadratic pyramidal tip used in this study φ was calculated as the mean angle. Poisson's ratio was set to $\mu = 0.5$.

The indentation depth, δ, can be expressed as a function of cantilever deflection, *d*, and height, *z*:

$$\delta = (z - z_0) - s \cdot (d - d_0) \tag{3.9}$$

The sensitivity, s, is a conversion factor to convert the cantilever deflection, measured in volts, into units of length and was determined during calibration prior to each experiment. z_0 and d_0 represent the cantilever height and deflection at the point of the first tip-sample contact, respectively.

By replacing equations (3.8) and (3.9) into equation (3.1) and applying Hook's law, $F = k.s.(d - d_0)$, the following relation is obtained [104]:

$$z = z_0 + s \cdot (d - d_0) - \sqrt{\frac{2 \cdot (1-\mu^2) \cdot k \cdot s \cdot (d - d_0)}{1.4906 \cdot E \cdot \tan\varphi}} \tag{3.10}$$

where *k* corresponds to the spring constant of the cantilever.

The identification of the first tip-sample contact point (z_0, d_0) is crucial for data analysis and particularly prone to errors for soft materials [104]. This source of error, which is mainly caused by the gradual increase of the slope near the onset point, diffuse interfaces and a the high level of noise associated with small cantilever spring constants, can be overcome by a sequential search [47]. The procedure described below is a modification of the algorithms introduced by Lin et al. [47] and Dimitriadis et al. [105]. Briefly, the contact point candidate is marched over all data points within a predefined "marching Range". The fits are compared with regard to their mean sum of square residuals. The best fit yields the Young's modulus.

The fitting algorithm consists of the following steps:

1. **Importing the Data**: a dataset of the length n is imported as a list of point coordinates in the form (z [m], d [V]):

$$data = ((z,d)_1, (z,d)_2, \cdots, (z,d)_n) \tag{3.11}$$

2. **Defining the Marching Range**: in the absence of strong repulsive interactions the first contact point is in the vicinity of the onset point. Thus, the marching range is constrained to this part of the data set. For this purpose two lines are fitted to the outermost part of the contact, $r_{contact}$, and non-contact, $r_{noncontact}$, regions defined by

$$r_{noncontact} = \left\{(z,d) \in data \middle| \left(\frac{z_{max} + z_{min}}{2}\right) < z\right\} \tag{3.12}$$

$$r_{contact} = \left\{(z,d) \in data \middle| \left(\frac{d_{max} + d_{min}}{2}\right) < d\right\} \tag{3.13}$$

z_{min} and z_{max} correspond to the minimum and maximum cantilever height and d_{min} and d_{max} represent the minimum and maximum cantilever deflection, respectively. The data point closest to the interception of the two fitted lines is chosen as the center of the marching range (z_c, d_c). The marching range is defined as data points within a specific distance R from this center (Figure 3.4.3):

$$r_{marching} = \left\{(z,d) \in data \middle| \sqrt{(z - z_c)^2 + (d - d_c)^2} \le R\right\} \tag{3.14}$$

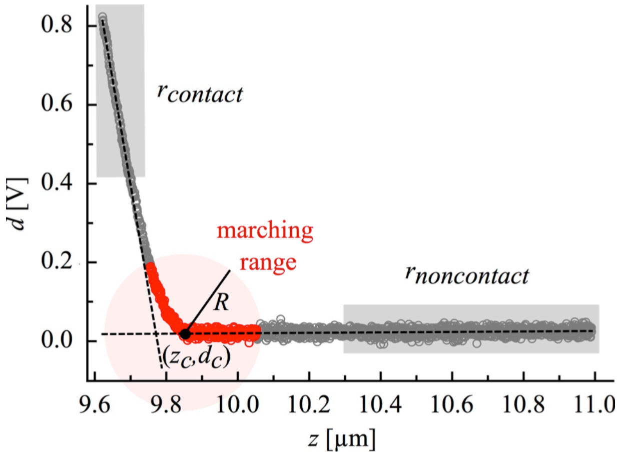

Figure 3.4.3. Defining the "marching range". Light gray circles show a representative deflection-height curve measured on isolated mesoglea. The center of the marching range (z_c, d_c) is determined as the data point closest to the interception of two lines (dashed black lines) fitted to the regions $r_{noncontact}$ *and* $r_{conatct}$ *(gray rectangles). The marching range (red circles) consists of all data point within a distance R from (z_c, d_c).*

3. **Marching**: for each potential first contact point $(z_0^*, d_0^*) \in r_{marching}$ equation (3.10) is fitted to the contact region of the data set as defined by

$$r_{fit} = \{(z,d) \in data | z < z_0^* \wedge d < d_e\}. \tag{3.15}$$

d_e defines the end of the fitting range. In this study force curves were fitted up to a cantilever deflection of 0.5 V.

4. **Extraction of Young's modulus**: The fits obtained in step 3 are compared with regard to their mean square residuals:

$$f_{goodness} = \frac{1}{n}\sum_{m=1}^{n}(z_{data}(d_m) - z_{fit}(d_m))^2 \tag{3.16}$$

where n is the number of data points in the corresponding fitting range. The normalization by n compensates for the change in the number of data points contributing to the sum of square residuals, which is associated with the marching process. The Young's modulus is obtained from the best fit showing the minimum $f_{goodness}$ (Figure 3.2.4).

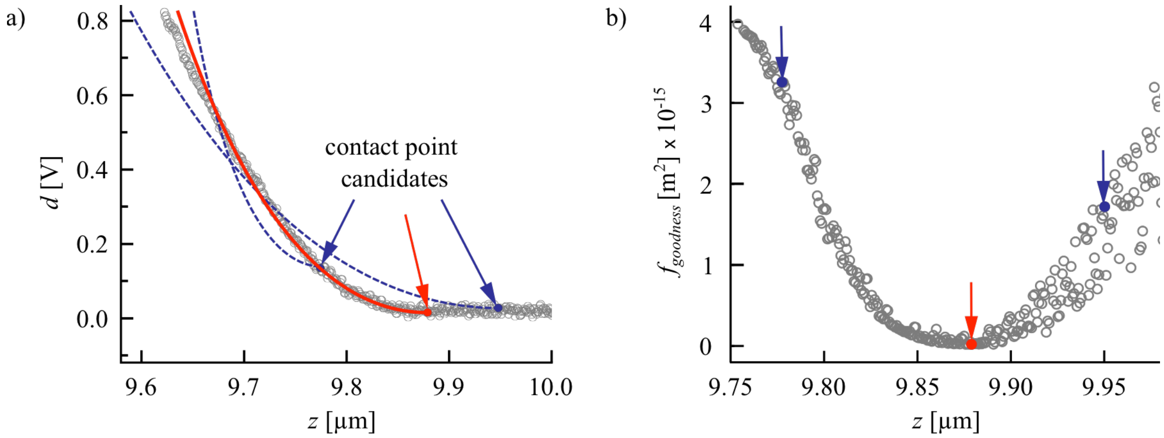

Figure 3.4.4. Marching of contact point candidate. a) The model (equation (3.10)) is fitted to the deflection-height curve for all contact point candidates within the marching range. Three representative fits are shown (blue dashed and solid red line). Young's modulus is extracted from the best fit (red) with the minimum f_{goodness} *. b) Change of the fit goodness,* $\mathrm{f}_{\mathrm{goodness}}$*, during marching. The blue and red points correspond to the contact point candidate indicated in panel (a). The red contact point candidate leads to the best fit.*

Elasticity pattern classification (wildtype)

Average elastic moduli of gastric region $0.6 \le d \le 1.0$, and peduncle $0.0 \le d < 0.1$ were normalized by the mean elastic modulus of the budding region $0.1 \le d \le 0.3$. The distribution of $E_{gastric}/E_{budding}$ and $E_{peduncle}/E_{budding}$ are shown in figure 3.4.5a and b. Each histogram was fitted with a sum of two Gaussians. The intersection point of the two curves was used as a threshold for discrimination between different patterns as describes by the flow chart in Figure 3.4.5c. Elasticity maps with $E_{gastric}/E_{budding} \ge 0.71$ were considered as uniformly elastic, i.e. type A patterns. The remaining patterns were compared with regard to the elasticity of peduncle, i.e. $E_{peduncle}/E_{budding}$. In this case the intersection point of the fitted Gaussians at $E_{peduncle}/E_{budding} = 0.85$ (Figure 3.4.5b) served as criterion for discrimination between pattern B, $E_{peduncle}/E_{budding} \ge 0.85$, and pattern C, $E_{peduncle}/E_{budding} < 0.85$.

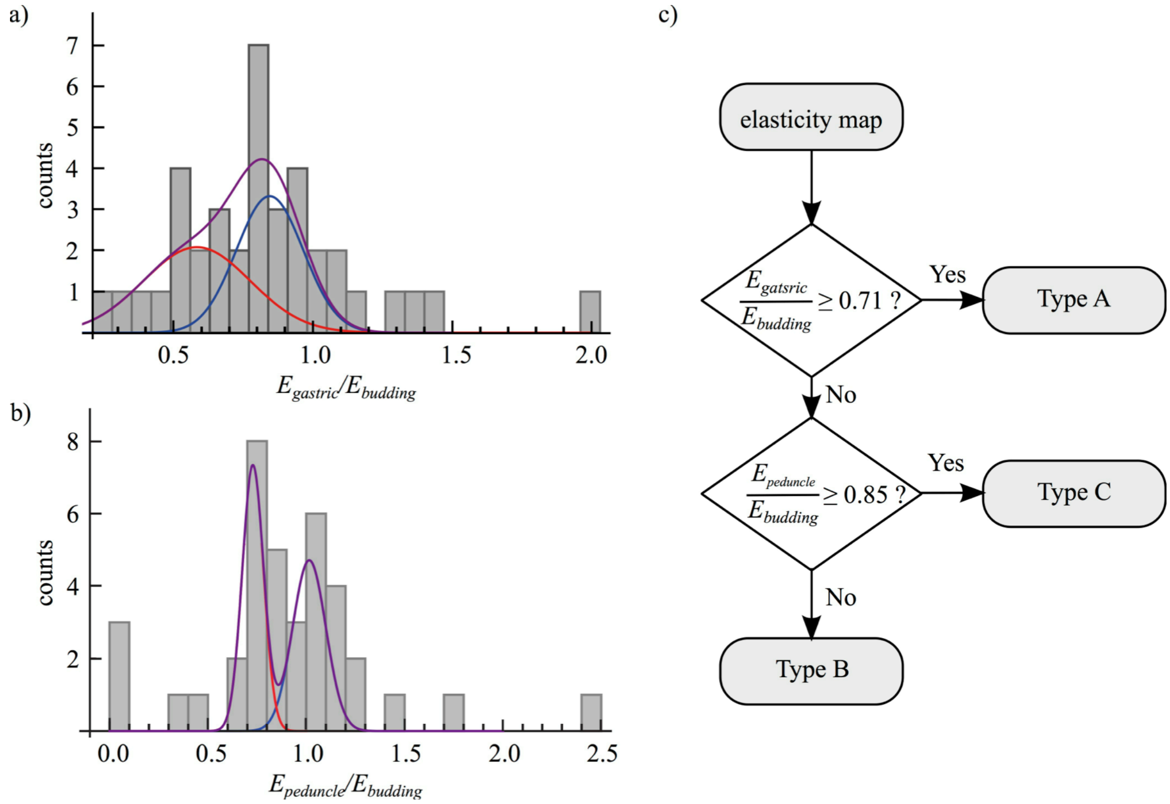

Figure 3.2.5. Classification of mesoglea elasticity maps of wild-type Hydra magnipapillata. a) Distribution of gastric elasticity normalized by elasticity of the budding region. The histogram was fitted (purple) with a sum of two Gaussian functions. The two Gaussian functions (red and blue curves) intersected at $E_{peduncle}/E_{budding}$ = 0.71, which served as threshold for identification of uniformly elastic patterns (tape A). b) Distribution of peduncle elasticity normalized by elasticity of budding region. The intersection of the two Gaussians at $E_{peduncle}/E_{budding}$ = 0.85 was chosen as threshold for discrimination between type B and C patterns. c) Flow chart for categorization of elasticity maps as type A, B or C patterns based on the thresholds obtained in (a) and (b).

3.4.5 Mesoglea Proteomics

Sample preparation for proteome analysis

SILAC Hydra were produced as described in Petersen et al. 2015 [84]. Mesogleas were isolated as described in section 3.4.2. Isolated mesoglea from wild-type and SILAC Hydra were precipitated by adding 4 volumes of -20°C 80% acetone and stored over night at -20°C. Samples were washed with 80% acetone and the pellet were dissolved in 50 mM Tris.HCl, containing (pH = 8.4) 6 M guanidinium hydrochloride. Dithithreitol (DTT) were added to a final concentration of 10 mM and the samples were incubated for 5 min at 95°C. For alkylation of reduced cysteins, iodoacetamide were added to a final concentration of 20 mM and stored for 30 min at room temperature. To quench the remaining iodoacetamide additional DTT was added to a final concentration of 10 mM. Samples were diluted 1:6 with

50 mM Tris.HCl (pH = 8.4). Lys-C (Wako Pure Chemical Industries, Osaka, Japan) was added in an enzyme sample ratio of 1:50 and incubated at 25°C for 18 hours. After digestion, samples were acidified with trifluoroacetic acid (TFA) and desalted with homemade solid phase extraction (SPE) cartridges using POROS R2 material (Applied Biostystem, Thermo Fisher Scientific, Waltham, United States). Peptides were eluted with 80% acetonitrile, dried in a speed vac and subsequently re-suspended in water. Peptide concentrations were measured at 205 nm wavelength on a NanoDrop instrument and non-labeled and SILAC samples were mixed in a 1:1 ratio.

Mass spectrometry (MS)

Proteome samples were analyzed in three biological replicates on an LTQ-Orbitrap XL mass spectrometer (Thermo Fisher scientific, Waltham, United Stated) coupled to a nanoAcquity ultra performance liquid chromatography (UPLC) system (Waters GmbH, Eschborn Germany). The reverse phase-LC system consists of a 5 µm Symmetry C18 pre-column (Waters GmbH, Germany) and a 1.7 µm BEH130 C18 analytical column (Waters GmbH, Eschborn, Germany). Peptide mixtures were loaded on the pre column at a flow rate of 7 µL/min and were then eluted with a linear gradient at a flow rate of 0.4 µL/min. The mass spectrometer was operated in the data-dependent mode to automatically measure MS and tandem mass spectrometry (MS/MS). LTQ-Orbitrap XL was set to acquire a full scan at 60000 resolution at 400 m/z from 350 to 1500 m/z and simultaneously fragment the top 6 peptide ions in each cycle in the LTQ (Linear Trap Quadropole). The selected ions were excluded from MS/MS for 35 seconds.

Mass spectrometry data analysis

LC-MS/MS raw data were analyzed with MaxQuant version 1.4.0.3 [106] with default settings. Proteins were identified using NCBI Hydra magnipapillata proteome database (Annotation release.101). Cysteine carbamidomethylation was used as a fixed modification and methionine oxidation, protein N-terminal acetylation as variable modifications. For the identification, the false discovery rate was set to 0.01 for peptides and proteins (the minimal peptide length allowed was six amino acids).

Protein ratios were normalized by its own “Spike-in” ratio as described in [107]. Using Perseus, protein ratios were additionally normalized for systematic errors by dividing with the median ratio. Protein IDs were filtered for proteins with at least 3 quantitative values in at least one time point.

3.4.6 Alsterpaullone Treatment

Freshly detached buds collected from a synchronized culture were incubated in a 5 µM solution of alsterpaullone (Sigma-Aldrich, United States) in 0.025% dimethyl sulfoxide (DMSO) (Sigma-Aldrich, United States) in Hydra Medium for 1 day. Hydras were subsequently washed several times with hydra medium and cultured for up to further 4 days on a daily feeding regime. Mesoglea was isolated from 1 day starved Hydras.

Elasticity pattern classification (Alp-treated)

The average elastic modulus of the gastric region $0.6 \leq d \leq 1.0$, and peduncle $0.0 \leq d < 0.1$ were compared to the budding region $0.1 \leq d \leq 0.3$. $E_{gastric}/E_{budding}$ was fitted with only one Gaussian while $E_{peduncle}/E_{budding}$ was fitted with a sum of two Gaussians (Figure 3.4.6). The intersection point of the fits at $E_{peduncle}/E_{budding} = 1.01$ served as a threshold for discrimination between type A and Alp-type ($1.01 \leq E_{peduncle}/E_{budding}$) elasticity maps.

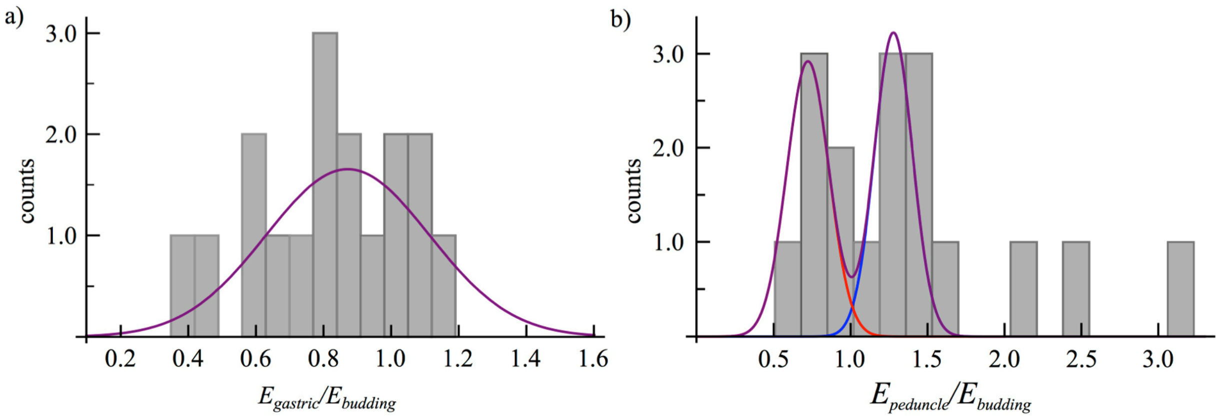

Figure 3.4.6. Elasticity pattern classification of Alp-treated Hydra mesoglea. a) Distribution of the mean elastic modulus of the gastric region normalized by the budding region's elasticity. The Histogram could be fitted with only one Gaussian. b) Distribution of the mean elastic modulus of peduncle relative to the budding region showed two peaks. A multi-peak Gaussian was fitted to the histogram (purple). Red and blue curves represent the Gaussian functions contributing to the multi-peak fit. The intersection point was determined to be at $E_{gastric}/E_{budding} = 1.01$.

Chapter 4

Tracking Mechanical and Morphological Dynamics of Regenerating Hydra Tissue Fragments Using a Two Fingered Micro-Robotic Hand[*]

The regeneration of Hydra from small pieces of tissue or cell re-aggregates begins with the formation of a hollow sphere, which undergoes successive expansion-contraction cycles during the course of regeneration [26]. These extensive shape fluctuations are essential for a complete and successful regeneration and proposed to drive the pattern formation via mechanogenetic or mechanochemical processes [109]. Nevertheless, there is almost no quantitative study on the mechanics of hydra regeneration. In this chapter a highly sensitive (~ 1 nN) two-fingered micro-robotic hand is used to 1) determine the viscoelastic properties of regenerating hydra tissue and 2) measure the force fluctuations actively generated in association with the morphological fluctuations in a quantitative and non-invasive manner.

4.1 Introduction: Hydra Regeneration

The freshwater polyp Hydra is famous for its almost unlimited regenerative capability. In fact it was the enormous regenerative potential, first discovered by Abraham Trembley [110] that won them the name Hydra after the Larnaean Hydra, the Greek mythical beast killed by Hercules in the second of his twelve labors [111].

Hydra polyps can readily regenerate injured or missing body parts like tentacles, head or foot [112]. But their regenerating potential is not only restricted to head or foot; intact Hydras

---

[*] This chapter is based on the work: Ref. No. 108.Veschgini, M., et al., *Tracking mechanical and morphological dynamics of regenerating Hydra tissue fragments using a two fingered micro-robotic hand.* Applied Physics Letters, 2016. **108**(10): p. 103702.

can regrow from pieces of tissue (regenerate) as small as ~ 300 epithelial cells (compared to ~10^5 cells in an intact hydra) [113]. Even aggregates of dissociated single cells (re-aggregate) give rise to intact Hydra polyps within a few days [114]. This outstanding regenerative capability is attributed to the stemness of the epithelial cells, which continuously proliferate in the body column and respond to positional information [112] that are provided by gradients of morphogens along the body column, which set up the oral-aboral polarity (OA-polarity) [115]. Large pieces of tissue (radius ≥ 250 µm) were observed to sustain their initial OA-polarity during regeneration so that the head always forms at the formal apical and the foot at the formal basal end of the tissue fragment [26]. However, small pieces of tissue (radius 100-200 µm) were reported to lose their positional information and require *de novo* pattern formation during regeneration [26]. The regeneration process starts with the folding of the tissue fragment into a hollow sphere with ectodermal epithelial layer on the outer and the endodermal cells on the inner surface separated by a sheet of ECM, called mesoglea (Figure 4.1.1a) [113]. During further regeneration the tissue sphere undergoes successive expansion-contraction cycles [109] (Figure 4.1.1b), which were found to be driven on an osmoregulatory basis so that they were accelerated or decelerated depending on the osmolarity of the external medium [26, 116]. Similar variation of contraction frequency of the body column with osmolarity of the external medium has also been observed for intact Hydra polyps [117]. In both cases, the epithelial bilayer creates a hyperosmotic fluid (relative to external medium) in the gastric cavity [118]. The consequent inflow of water results in the inflation of the tissue but in contrast to intact polyps, which release the excess water through the mouth opening during contraction of the body column, hydra regenerates inflate until the tissue shell ruptures and the internal fluid is

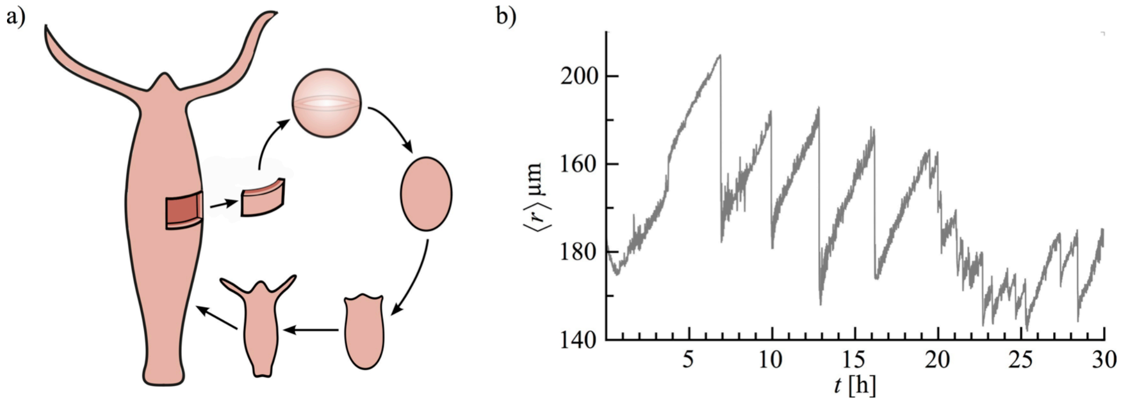

Figure 4.1.1. Regeneration of hydra tissue fragments. a) Schematic representation of the regeneration process. The tissue piece rounds up and forms a hollow sphere, the regenerate. The spherical symmetry breaks during the regeneration process, locking the future oral-aboral axis. Head and foot are formed at later developmental stages. b) Changes in the mean radius of the regenerate over time.

released by a sudden contraction of the tissue sphere (Figure 4.1.1b[*]) [109].

Based on the amplitude and frequency of the size fluctuations, Soriano et al. classified the regeneration process of hydra regenerates into two main phases: 1) Phase I: the early stages of regeneration (~ 20 h) were marked by fluctuations of large (up to 25% increase in radius) amplitude and low frequency. During this phase the rupture of the tissue was reported to occur at different positions, 2) Phase II: later regeneration stages were characterized by size oscillations of small amplitudes and high frequencies [26]. Soriano et al. attributed the small fluctuation amplitude observed in phase II to the formation of a, in contrast to phase I, permanent weak spot in the tissue shell that released the excess water at a lower threshold pressure [26]. Intriguingly, the transition from phase I to phase II was found to be accompanied by an elongation of the regenerate, whereby the major axis correlated with the future oral-aboral axis [26]. This finding led to the assumption that the transition between phase I and phase II coincided with the formation of the head organizer and was defined as the symmetry breaking and axis locking moment [26, 109]. This hypothesis was supported by the fact that the direction of the future body axis could be affected by external cues, like temperature gradients, only during phase I, whereas the preset axis of phase II regenerates was not influenced [119].

Phase I oscillations are essential for symmetry breaking and hence a successful regeneration. For instance, slowing down the expansion rate by increasing the osmolarity of the external medium was reported to delay the symmetry breaking time up to a complete failure in regeneration [26]. Moreover, large tissue fragments that sustain the OA-polarity were found to lack phase I oscillations during regeneration [26], leading to the assumption that the extensive size fluctuations are closely related to signaling and pattern formation. This was supported by the finding that a drug-induced delay in head differentiation resulted in a significant prolongation of phase I [26]. On the other hand, induction of OA-polarity by implantation of small cell clusters with high head activation potential [120] led to a shortening of phase I [26]. Previous studies have proposed that the size fluctuations drive the pattern formation via mechano-genetic or mechano-chemically coupled processes mediated for example via mechano-sensitive channels [26, 119, 121]. Although, these considerations emphasize the importance of regenerate mechanics and active forces involved in symmetry breaking for a quantitative understanding of the underlying mechanisms there has been no quantitative study on mechanics of regenerating Hydra tissues.

---

[*] Data kindly provided by Florian Gebert.

The main goal of this chapter is to determine the viscoelastic properties of Hydra regenerates during the early stages of regeneration (3-5 h after cutting) using a two-fingered micro-robotic hand with a high force sensitivity of ~1nN [27]. Moreover, the force fluctuations of a regenerate are monitored with a time resolution of 1 s and compared to shape fluctuations of a free regenerating Hydra.

4.2 Results and Discussion

In this chapter the mechanical properties of regenerating Hydra tissues were studied during the early stages of regeneration (phase I). Small pieces of tissue were cut off the gastric region, as demonstrated in Figure 4.2.1a and allowed to curl up by time. The resultant hollow tissue sphere, the Hydra "regenerate", was subjected to a two-fingered micro-robotic hand [27] 3-5 h after cutting (in collaboration with N. Khangai, Laboratory of Prof. T. Arai, Graduate School of Engineering Science, Osaka University).

The micro-hand consisted of two glass needles, "fingers", coupled via two stories of parallel mechanism modules that enable the independent movement of the two fingers (Figure 4.2.1b). Each finger is endowed with 3 degrees of freedom in translational motion facilitating a dexterous grasping of micro-objects. Moreover, piezo-electric motors ensure a precise control of the separation distance *D* between the fingers (Figure 4.2.1c) [27]. In order to minimize the force felt by single cells and prevent a damage of the tissue, plate-shaped end effectors [122] were used in this study (Figure 4.2.1c).

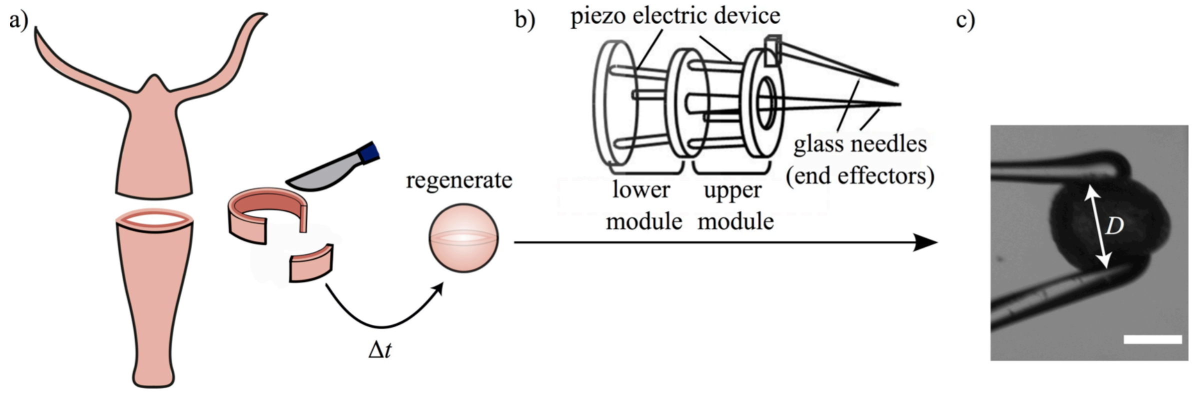

Figure 4.2.1. Schematic illustration of experimental setup. a) A ring-like tissue fragment cut off from the gastric region of a Hydra polyp is quartered. Each fragment was allowed to rounds up by time forming a "Hydra regenerate". b) Schematic representation of the two-fingered micro-robotic hand. Two parallel mechanism modules allow an independent movement of two glass needles, "end effectors". c) Microscopy image of a Hydra regenerate clamped between plate-shaped end effectors at a separation distance D. Scale bar corresponds to 200 µm.

One micro-finger is attached at its base to a highly sensitive force sensor (resolution of $\square F \sim 1$ nN; RMS noise level of 15 nN), which measures the deflection of the sensing finger by means of a strain gauge [27, 122]. This high force sensitivity makes the micro-hand a versatile tool for precise and quantitative measurements of small forces or mechanical properties of soft micro-objects in a non-invasive manner as was demonstrated before on human lung epithelial cells [123].

4.2.1 Viscoelastic Properties of Regenerating Hydra Tissue

In order to determine the viscous and elastic modulus of Hydra regenerates, samples were clamped between the end-effectors and compressed by linearly decreasing the distance D (red curve in 4.2.2). The force increased almost linearly during the compression (blue curve in 4.2.2). After reaching a predefined force level $F_{\max}$, the compression was stopped and the force relaxation was observed over time at a separation distance D_{const}. 11 measurements were performed on three regenerates.

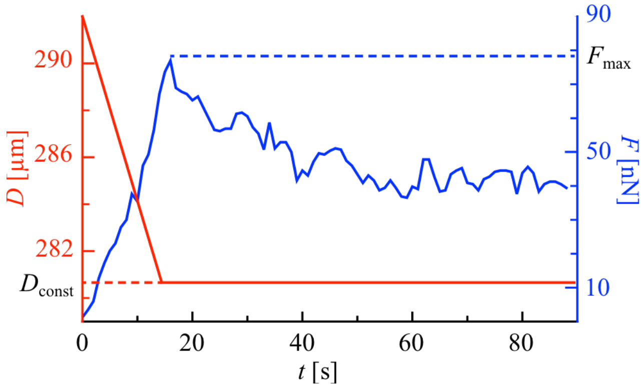

Figure 4.2.2. Compression and force relaxation of a Hydra regenerate. After clamping, the Hydra regenerate was compressed by linearly decreasing the separation distance D (red). The force was monitored in parallel (blue). After reaching F_{max}*, the force relaxation was observed at a constant separation distance,* D_{const}.

Bulk Elastic Modulus of Hydra Regenerates

To obtain the bulk elastic modulus of Hydra regenerates, the response of the regenerate was studied during the linear compression down to D_{const}. As shown in Figure 4.2.2 the force increased almost linearly during the compression. In order to verify a linear response of the system, measurements were performed with varying $F_{\max}$ and $\Delta D = |D_{\text{const}} - D|$ (Figure 4.2.3a). The corresponding stress, σ, and strain, ε, were determined according to:

$$\sigma = \frac{F_{\max}}{A} \quad , \qquad \varepsilon = \frac{\Delta D}{D_0} \tag{4.1}$$

where A represents the contact area between the regenerate and micro-finger and D_0 corresponds to the initial diameter of the regenerate. Both values were determined from microscopy images recorded during each experiments. The obtained stress-strain relationship is illustrated in Figure 4.2.3b. The results clearly indicated a linear elastic response of the regenerates within the considered strain range of $\varepsilon < 0.15$. A bulk elastic modulus of:

$$E = \frac{\sigma}{\varepsilon} = (185 \pm 13)\ \text{Pa} \tag{4.2}$$

was obtained from a linear fit to the stress-strain curve (red line Figure 4.3.3b). The linear response of the system further allowed for the calculation of a Hookean spring constant, k, for Hydra regenerates from the $F_{\max}$- ΔD relation (Figure 4.2.3) according to:

$$k = \frac{F_{\max}}{\Delta D} = (8.1 \pm 0.7)\ \text{mN/m} \tag{4.3}$$

Force relaxation of Hydra regenerates

To gain further insight into the viscoelastic properties of the regenerates, the force relaxation at constant D was studied in the next step. As demonstrated in figure 4.2.4 the force relaxation behavior of the regenerates could be modeled with a single exponential function of the form (red curve in Figure 4.2.4):

$$F(t) = a.e^{-bt} + c \tag{4.4}$$

where $F(t)$ represents the force as a function of the time t and $c = \lim_{t\to\infty} F(t)$. The parameter b is a measure of the relaxation kinetics and enables the calculation of a characteristic relaxation time $\tau = b^{-1}$. 9 force relaxation curves were analyzed, yielding an average

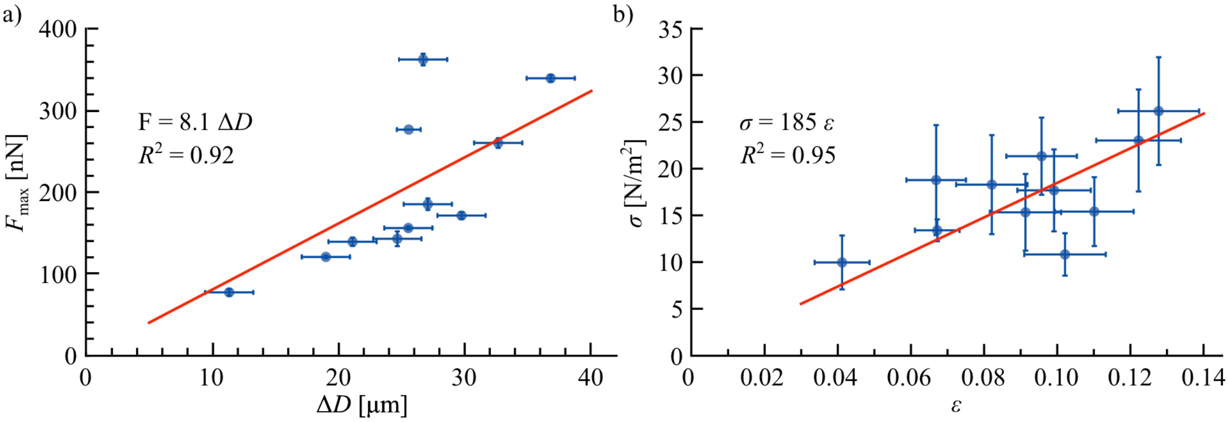

Figure 4.2.3. Compression experiment of Hydra regenerates. a) Change in maximum force, F_{max}*, as a function of compression level measured at a micro-finger displacement ΔD. A Hookian spring constant of* k *~ (8.1 ± 0.7) mN/m was determined from a linear fit (red line). b) The corresponding stress-strain relationship showed a linear response of the system with a bulk elastic modulus of* E *~ (185 ± 13) Pa obtained from the linear fit (red line).*

characteristic relaxation time of $\langle \tau \rangle = (19 \pm 8)$ s.

The force relaxation at a constant D can be translated as stress relaxation behavior of Hydra regenerates at a constant strain. The simplest model describing such a single exponential stress relaxation behavior is the Maxwell model for viscoelastic materials (inset figure 4.2.4). Thus, the Maxwell model (see section 2.1) was applied in order to obtain the viscous modulus, η, and the Stokes frictional coefficient, γ, for Hydra regenerates according to:

$$\eta = E \cdot \langle \tau \rangle = (3.6 \pm 1.5) \times 10^3 \text{ Pas} \qquad (4.5)$$

$$\gamma = k \cdot \langle \tau \rangle = (0.17 \pm 0.08) \text{ Ns/m} \qquad (4.6)$$

Where E and k correspond to the elastic modulus and spring constant obtained above, respectively.

It is noteworthy that the mechanical properties of Hydra regenerates are governed by both the tissue shell and the fluid core. The experimental setup used in this study does not allow for a de-convolution of these two contributions. Nevertheless, the obtained elastic modulus ($E \sim 185$ Pa) is in good agreement with previous findings on chicken embryonic cell aggregates that estimated a shear modulus of ~ 100 Pa using the two-plate method [124].[*] But the relaxation behavior of Hydra regenerate was clearly different; while the relaxation of embryonic cell aggregates was reported to be governed by a fast elastic and a slow viscos contribution with two characteristic relaxation times ($\tau_1 \sim 2$ s and $\tau_2 \sim 20$ s), the relaxation of Hydra regenerates could be reproduced by a single exponential fit with a relaxation time of $\langle \tau \rangle = (19 \pm 8)$ s

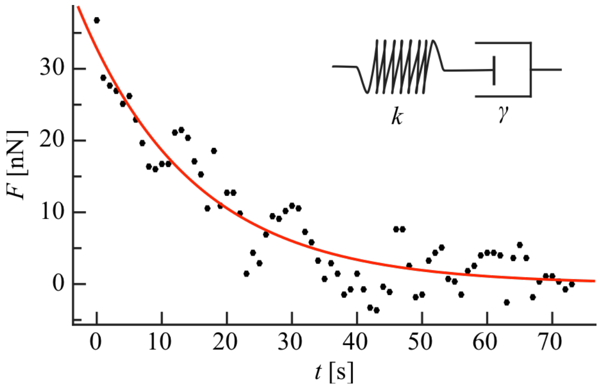

Figure 4.2.4. Representative force relaxation curve of a Hydra regenerate over time. The force relaxation was monitored at the constant separation distance D_{const}. *The data could be fitted with a single exponential function (red curve), which can be reproduced with the Maxwell model (inset) consisting of a serial connection of a spring with the spring constant* k *and a dashpot with a Stokes frictional coefficient of* γ.

---

[*] For an isotropic and homogenously elastic material the elastic modulus E is related to the shear modulus G via $E = 2G(1+\mu)$, where μ corresponds to Poisson´s ratio.

comparable to τ_2. Moreover, Hydra regenerates showed an almost one order of magnitude smaller viscos modulus compared to the embryonic cell aggregates ($\eta \sim 10^4$ Pas [124]). These deviations might be attributed to the structural differences: void Hydra tissue sphere with a fluid core versus compact embryonic cell aggregates (see above).

Notably, an advantage of the micro-robotic hand used in this study compared to the conventional two-plate method [124, 125] is that the contact area A between micro-finger and regenerate can be considered to be constant throughout the measurement. This is ensured by the small contact area of the micro-finger tip ($A \sim 1 \times 10^4$ µm^2) compared to the cross sectional area of the regenerate (9×10^4 µm^2), facilitating a robust measurement of the sample viscoelasticity regardless of morphological changes and active fluctuations. Moreover, the higher force resolution ($\Delta F \sim 10^{-9}$ N) of the micro-hand in comparison to the two-plate method ($\Delta F \sim 10^{-6}$ - 10^{-7} N) allows for more precise measurements.

4.2.2 Active Force Fluctuations During Hydra Regeneration

As illustrated in Figure 4.2.4. the force relaxation curves of Hydra regenerates were superimposed by oscillatory force fluctuations indicating the generation of active forces. In

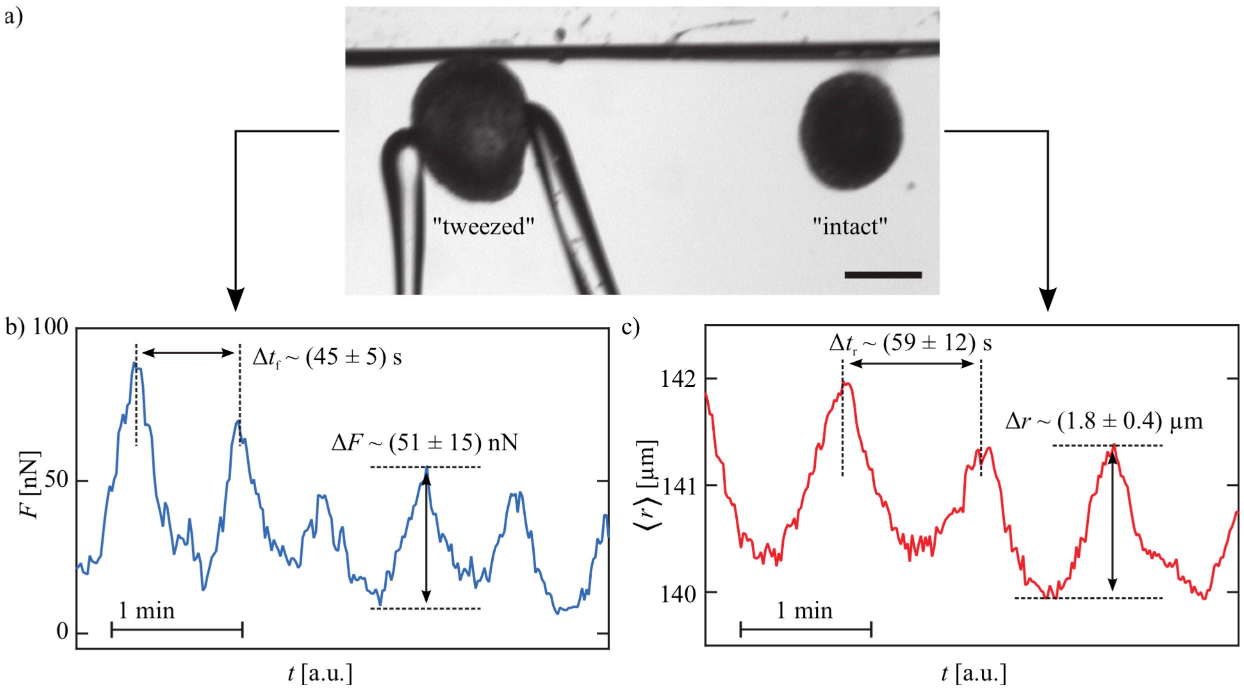

Figure 4.2.5. Active force fluctuations during regeneration. a) Parallel observation of a "tweezed" (left) and an "intact" Hydra regenerate allows for comparison of force fluctuation recorded by the micro-hand and size fluctuations of a free regenerating sample. Scale bar, 200 µm. b) Typical force response of a Hydra regenerate showing periodic force oscillation. c) Typical morphological fluctuations observed for the "intact" regenerate represented by the change in the man radius. All values correspond to an average over 10 oscillations.

order to understand the relation between force fluctuation and morphological oscillations, two regenerates were prepared from the same Hydra and observed simultaneously (Figure 4.2.5a): 1) one regenerate was subjected to grasp-release cycles by the micro-hand, in order to monitor the force fluctuations ("tweezed" regenerate): clamping periods of 90-350 s with a force of ~ 100 nN were followed by 20-100 s intervals of releasing. The periodic clamping was necessary due to the occasional slipping of regenerates and a temporal drift of the force sensor's baseline. 2) The second regenerate was placed next ("intact" regenerate) to the "tweezed" specimen and allowed to regenerate freely in order to track the morphological dynamics without external disturbance. Figure 4.2.5b and c show representative segments of the observed force and size fluctuations over time, respectively. Both parameters showed regular oscillations with characteristic period and magnitude. The "tweezed" regenerate showed force oscillations with a periodicity of Δt = (45 ± 5) s and magnitude of $\Delta F_{\mathrm{tweezed}} = (5 \pm 2) \times 10^{-8}$ N, which is well below the rupture force of 190 nN estimated by Kücken et al. [116]. The "intact" regenerate exhibited size oscillations with a periodicity Δt = (59 ± 12) s comparable to that observed for force oscillations. The values correspond to an average over 10 periods. In order to compare the magnitude of the size to force oscillations, the active force deforming the intact regenerate was estimated from the magnitude of the size oscillation Δr = (1.8 ± 0.4) µm. The corresponding strain $\varepsilon = \frac{\Delta r}{\langle r \rangle}$ = (0.013 ± 0.003) (with a mean radius $\langle r \rangle$ = (142 ± 2) µm) was within the linear viscoelastic regime, $\varepsilon < 0.15$ (Figure 4.2.2b). Hence, the force was calculated by the following equation:

$$\Delta F_{\mathrm{inatct}} = \varepsilon \cdot E \cdot A \approx (3 \pm 1) \times 10^{-8}\ \mathrm{N} \tag{4.7}$$

Where E corresponds to the elastic modulus (Eq. 4.2) and A is the contact area. The results show that both magnitude and periodicity of size oscillations were in good agreement with force oscillations that were directly measured at the tweezed sample demonstrating a direct correlation between force and morphological fluctuations. These findings verify that using the two-fingered micro-hand the force fluctuations could be precisely determined without disturbing the morphological dynamics of the regenerate and guarantees the non-invasive character of the assay developed in this study. Moreover, this experiments represents the first quantitative study of the short time oscillations of regenerating Hydra tissues.

4.2.3 Summary

The freshwater polyp Hydra has an almost unlimited regeneration capacity. Small fragments of tissue can regenerate into intact polyps. The regeneration process is governed by extensive morphological oscillations, suggesting the generation of active forces. These shape fluctuations are proposed to direct the patterning and symmetry breaking of the tissue via mechano-chemically and mechano-genetically coupled processes.

In this chapter a highly sensitive two-fingered micro-robotic-hand was used to measure the viscoelastic properties of Hydra tissue fragments during the early stages of regeneration (~ 3-5 h). Hydra regenerates were first compressed linearly to different force levels. The obtained stress-strain relation clearly indicated a linear elastic response of the system with an elastic modulus of $E = (185 \pm 13)$ Pa. A Hookean spring constant of $k = (8.1 \pm 0.7)$ mN/m was determined from the force-displacement relationship.

The force relaxation behavior of hydra regenerates could be fitted with a single exponential function with characteristic relaxation time of $\langle\tau\rangle = (19 \pm 8)$ s. Adapting the simple Maxwell model for viscoelastic materials yielded a viscous modulus of $\eta = (3.6 \pm 1.5)$ Pas and a Stokes frictional coefficient of $\gamma = k \cdot \langle\tau\rangle = (0.17 \pm 0.08)$ Ns/m.

Moreover, the force oscillations of a Hydra regenerate were tracked over time and compared to size fluctuation of a freely regenerating sample. The results showed that the active forces oscillated with a periodicity of $\Delta t = (45 \pm 5)$ s and a maximum-to-minimum difference of $\Delta F = (5 \pm 2) \times 10^{-8}$ N. Both the periodicity and magnitude of force oscillations were in good agreement with the size fluctuations of the free specimen ($\Delta t = (59 \pm 12)$ s and $\Delta r = (1.8 \pm 0.4)$ µm corresponding to $\Delta F = (3 \pm 1) \times 10^{-8}$ N). These findings clearly indicated that using the micro-robotic-hand the active forces were precisely and quantitatively determined without disturbance of the natural morphological dynamics, which guarantees the non-invasive character of the assay developed in this chapter.

4.3 Materials and Methods

4.3.1 Hydra Culture

Hydra *magnipapillata* were cultured at (18 ± 1) °C in modified hydra medium [99] (1.0 mM $CaCl_2$, 1.0 mM Tris-HCl, 1.0 mM $NaHCO_3$, 0.1 mM KCl, 0.1 mM $MgCl_2$, pH = 7.4). They were fed with newly hatched *artemia* 5 days per week and cleaned a few hours after feeding each day. All experiments were performed in Hydra medium and at room temperature.

4.3.2 Micro-Robotic Hand

Technical details of the micro-robotic device are described in Khangai et al. [122] A brief description of the end-effector preparation and calibration will be presented here only.

Glass end-effectors were prepared and calibrated before the experiments. The end-effectors were prepared by pulling a glass rod with a diameter of 1 mm. In order to form plate-shaped end-effectors, the sharp end of the pulled glass was heated to obtain a spherical or drop-like tip a few 100 µm in diameter, which was grained into a plate-shaped tip. The end-effectors were mounted on the micro-hand. In order to calibrate the force sensor, a bead with a known weight was attached to the "sensing" end-effector. The end-effector was then rotated around its own axis while monitoring the electric signal due to the finger's deflection.

4.3.3 Sample Preparation

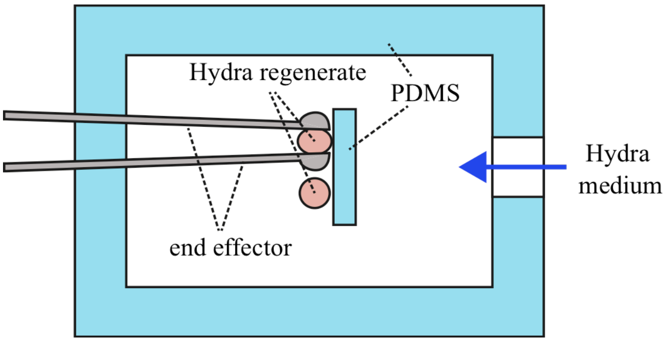

Figure 4.3.1. Schematic illustration of experimental setup (top view). The experimental chamber consists of a PDMS container placed on a glass slide. An additional "wall" of PDMS prevents the "tweezed" Hydra regenerate from escaping the force exerted by the end-effectors of the micro-hand. A second Hydra regenerate served as a reference sample. An inflow of Hydra medium prevents the samples from drying out.

A ring-like slice of tissue was removed from the upper half of the body column (gastric region). The ring was then quartered and the obtained tissue fragments were then left at room temperature to curl up into hollow spheres.

For each experiments, the Hydra regenerate was placed in self-made chamber made with a polydimethylsiloxane (PDMS) (SILPOT 184, Dow Corning Toray Co., Ltd., Ichihara, Japan) container on a glass slide (C050701, Matsunami glass ind. Ltd., Kishiwada, Japan), as shown in Fig. 4.3.1. There was an additional PDMS "wall" inside the chamber to make the tweezing of the Hydra easier. Here, the chamber was not sealed at the top so that the micro-hand can be applied. For this reason, the drying of the Hydra medium was prevented by constantly adding Hydra medium using the siphon principle.

4.3.4 Viscoelastic Properties of Hydra Regenerates

Hydra tissue fragments (regenerates) with a diameter of 200-300 µm were compressed by the two-fingered micro-hand 3-5 h after cutting. After the Hydra regenerates sank to the bottom of the dish, they were caught with the micro-hand tips. Plate-shaped end-effectors were used for all experiments. The contact area was assumed to be circular. In order to prevent the hydra ball from escaping the force exerted by the end-effectors, they were positioned up against a "wall" of PDMS (see Figure 4.3.1). After clamping, the separation distance, D, between the micro-fingers was decreased linearly within 15 s. After reaching the desired level, D_{const}, the strain was kept constant in order to monitor the force relaxation. The force relaxation was studied at different strain levels $\Delta D = | D_{\text{const}} - D | = 11\text{-}37$ µm for 30-150 s. All movies of the experiments were acquired with a frame rate of 1 fps. Only compression periods where the slipping of the regenerate was negligible were used for analysis.

4.3.5 Measurement of Active Force Fluctuations

In order to measure the active forces generated by the hydra tissue during the regeneration process, a hydra regenerate was compressed over a period of 94 min. Occasional slipping of hydra regenerate from the micro-fingers and the temporal drift of the force sensor's baseline made it necessary to release and re-grasp the sample periodically. The regenerate was compressed to a maximum force of 100 nN and kept at constant strain for 90-350 s and released for 20-100 s. Again, only compression periods where the slipping of the regenerate was negligible were used for analysis.

A second regenerate obtained from the same hydra was allowed to regenerate freely next to the "tweezed" tissue and observed simultaneously in order to determine the size fluctuation during regeneration (Figure 4.3.1). The entire experiment was acquired with a rate of 1 fps.

Chapter 5

Counteracting the Inhibitory Effect of Serum Albumin on the Lung Surfactant[*]:

A Film Balance Study

During the acute respiratory distress syndrome (ARDS), serum proteins leak from the blood capillaries into the alveolar air space [32]. The surface active proteins adsorb to the liquid-gas interface of the alveoli lining fluid (ALF), hinder the adsorption of the natural lung surfactants and lead to an increase in the surface tension of the ALF [32]. Decreased lung compliance, hypoxia and alveoli collapse are some of the dire consequences [126]. Unfortunately, the usual therapeutic approaches, applying lung surfactant substitutes, achieve only marginal improvements for the adsorbed proteins also affect theses surfactants [32, 33]. A promising approach is the ventilation with perfluorocarbon gases [32]. In this chapter, the impact of perfluorohexane vapor is studied on the competitive adsorption of a Gibbs-like DPPC monolayer in the presence of bovine serum albumin as a simplified model for lung surfactant inactivation during ARDS.

5.1 Introduction: Lung Surfactant Function and Diseases

The gas exchange in the lung takes place across the alveolar-capillary membrane. Alveoli are sac-like structures with a diameter of ~ 200 µm [127, 128] that are connected to the outside air via the airways and expand and contract during in- and exhalation. Their inner surface is lined with an aqueous fluid, called the alveolar lining fluid (ALF) [33]. (Figure 5.1.1)

During inspiration, contraction of the diaphragm generates a vacuum outside the alveoli, p_{out}, resulting in alveoli inflating [126]. The inflation of the alveoli, in turn, creates a negative pressure in the alveolar airspace, p_{alv}, with respect to the outside atmosphere, resulting in the inflow of air into the lung [126]. The pressure difference, $\Delta p = |p_{\mathrm{out}} - p_{\mathrm{alv}}|$, required to inflate an

---

[*] This chapter is related to the work: (Ref. No. 142) Nguyen P.N., Veschgini M., Tanaka M., Waton G., Vandamme T., Krafft M.P., *Counteracting the inhibitory effect of proteins towards lung surfactant substitutes: a fluorocarbon gas helps displace albumin at the air/water interface.* Chemical Communications, 2014. **50**(78): p. 11576-11579

alveolus of radius R depends, according to the Laplace equation, $\Delta p = |p_{out} - p_{alv}| = 2\gamma / R$, on the surface tension, γ, of the alveolar lining fluid [126]. In the lung the surface tension of ALF is regulated by a surfactant complex, called the lung surfactant (LS) [32]. By reducing the ALF surface tension, the lung surfactant 1) minimizes the work of alveoli inflation during inhalation and 2) prevents the alveolar collapse by decreasing the surface tension to near zero values at maximum compression upon expiration [32, 33, 126]. 90 wt% of the lung surfactant is composed of a mixture of unsaturated and anionic phospholipids, neutral lipids and cholesterol. Dipalmitoyl-phosphatidycholine (DPPC) is the major compartment of this fraction [31, 32] (Figure 5.1.1). The remaining 10 wt% of LS consist of specific surfactant proteins SP-A, SP-B, SP-C and SP-D [31, 32]. These proteins are involved in host defense and control of lung inflammation as well as biogenesis and recycling of the lung surfactant [32, 33]. Remarkably, pure DPPC monolayers can reduce the surface tension of an aqueous solution to near zero values by formation of a liquid condensed phase [32, 33]. However, the monolayer re-spreads only slowly upon expansion [31, 33]. The interplay between the surfactant proteins and various lipids in the lung surfactant assures 1) a fast adsorption of the surfactant to the interface, 2) near zero surface pressures upon expiration and 3) a fast re-spreading to keep the surface tension low during inhalation [31]. The latter has been attributed to surface bound reservoirs that form during adsorption or compression of the interfacial film [31]. Intriguingly, prolonged periodic expansions and compressions of the interface, as observed in the alveoli, have been reported to promote the decrease in the surface tension of Gibbs-like DPPC monolayers by facilitating the liquid expanded-liquid condensed (LE/LC) transition [129]. This effect, which was demonstrated by a bubble tensiometric assay, showed the maximum efficacy at oscillation frequencies f ~ 0.03-0.1 Hz comparable to breathing frequency [129].

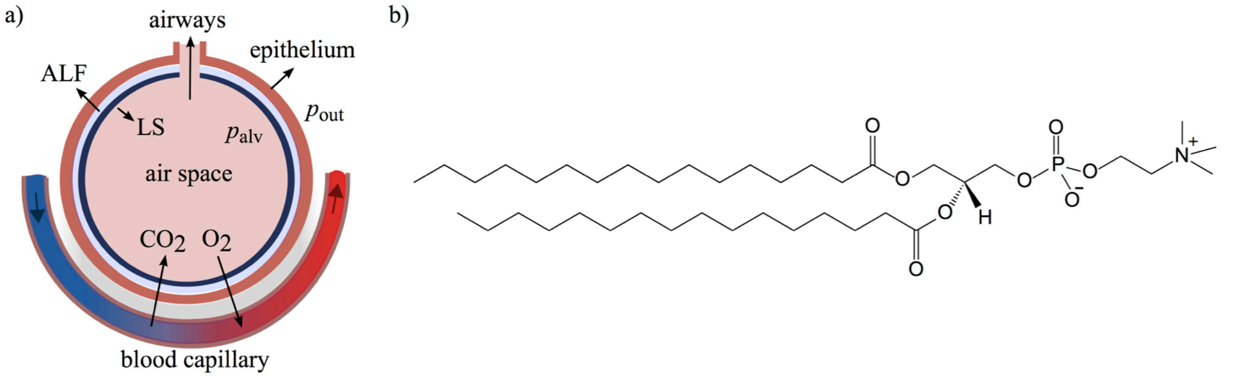

Figure 5.1.1. a) Schematic illustration of an alveolus. The inner surface of alveoli is lines with the alveoli lining fluid (ALF) containing the lung surfactant (LS), which decreases the surface tension of ALF and minimizes the work of breathing. b) Molecular structure of Dipalmitoyl-phosphatidycholine (DPPC) is the major lipid component in the LS.

In light of the aforementioned, any perturbation of lung surfactant functioning due to either surfactant absence or inactivation leads to critical diseases. The neonatal respiratory distress syndrome, NRDS, for example is ascribed to the absence of the lung surfactant in underdeveloped lungs of preterm neonates [32, 126]. NRDS manifests itself with alveolar collapse, decreased lung compliance, reduced functional residual capacity, hypoxia and lung edema [32]. In these cases the replacement of the LS by surfactant substitutes of either animal or synthetic origin is an effective treatment [33]. The acute respiratory distress syndrome, ARDS, on the other hand is attributed to the inactivation of the LS[32, 126]. The inactivation can, amongst others, be induced by the leakage of serum proteins like albumin or fibrinogen into the alveoli airspace as revealed by analysis of the bronchoalveolar lining fluid [33, 130]. A 5-16 folds increase of the serum albumin concentration was found in the lining fluid of ARDS patients compared to healthy lungs [130, 131]. Albumin is a surface-active protein and competes with the lung surfactant components for the adsorption to the liquid-air interface [126]. Once at the interface, albumin creates a steric and electrostatic barrier that kinetically hinders the adsorption of the LS from the sub-phase and, moreover, inhibits the re-spreading of LS components during inspiration [33, 126, 132, 133]. Hence, ARDS and NRDS share several symptoms [32, 33]. However, in the case of ARDS the inactivation mechanism affects both endo- and exogeneous surfactants so that the usual treatment with lung surfactant substitutes achieves only a moderate and transient improvement of lung function in ARDS patients [32, 126]. Different strategies are thus necessary to induce and accelerate the reversion of LS inactivation in ARDS.

One promising approach is the ventilation with perfluorocarbon gases (gPFC), which has already shown positive results in animal models [134, 135]. Fluorocarbons are highly stable and chemically and biologically inert [136]. The low polarizability of the fluorine atom leads to weak van der Waals interactions that result in high vapor pressures and low surface tensions [136]. Moreover, they adsorb to the air-water interface [137, 138]. When monolayers of DPPC or lung surfactant substitute were exposed to gPFCs, PFC molecules were incorporated into the monolayer and altered the phase behavior drastically [137, 138]. Fluorescence microscopy and grazing incidence X-ray diffraction studies revealed that, the PFCs incorporation hindered the formation of semi-crystalline domains of the liquid condensed phase and led to a fluidization of the surfactant film [137, 138]. Moreover, gPFCs were also reported to promote the re-spreading of DPPC monolayers in the presence of BSA [139]. Nevertheless, little is known about how gPFC influence the displacement of serum proteins by the lung surfactant.

In this chapter, the impact of vaporized perfluorohexane (PFH) is investigated on the co-adsorption of a Gibbs-like DPPC monolayer in the presence of bovine serum albumin (BSA), using a Langmuir film balance.

5.2 Results and Discussion

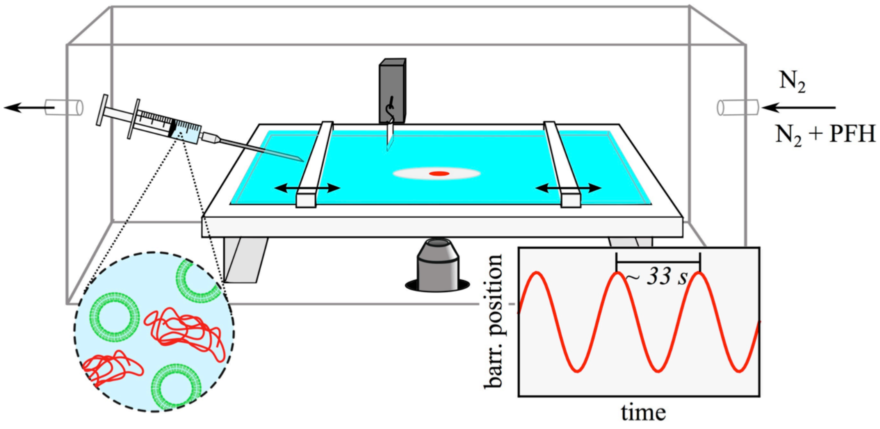

Figure 5.2.1. Schematic representation of the experimental setup. A Langmuir film balance was mounted on top of an inverted microscope and enclosed in a gastight box with gas in- and outlet. The surface pressure was measured using the Wilhelmy plate method. Highly concentrated solutions of DPPC vesicles (green) and BSA (Red) were injected into the sub-phase (circle lower left). The interfacial area was periodically changes during the experiments (box lower right).

The experimental setup is depicted schematically in Figure 5.2.1. Experiments were performed using a Langmuir film balance equipped at the bottom with a glass window, which was mounted on an inverted microscope in order to visualize the interfacial structural changes by means fluorescence microscopy. The setup was enclosed in a gastight box with gas in- and outlet that allowed the saturation of the gaseous phase with PFH. To better simulate the alveolar condition, the interfacial area was subjected to sinusoidal oscillations with a frequency of $f = 30$ mHz ($T \approx 33$ s) and an amplitude of $\Delta A = 15\%$, comparable to breathing movements. These conditions had been shown to accelerate the displacement of BSA by DPPC from the surface of oscillating bubbles most effectively [140]. BSA and DPPC vesicles ($D \sim 60\text{-}80$ nm, Appendix IV) were injected into the HEPES buffered sub-phase (pH = 7.4) to final concentrations of 7.5×10^{-4} mM for BSA and 1 mM or 3 mM for DPPC, close to the Albumin/DPPC ratio found in the native lung [31, 140]. The surface pressure, π, variations were studied at 37 °C and recorded over time, t, using a Wilhelmy-plate.

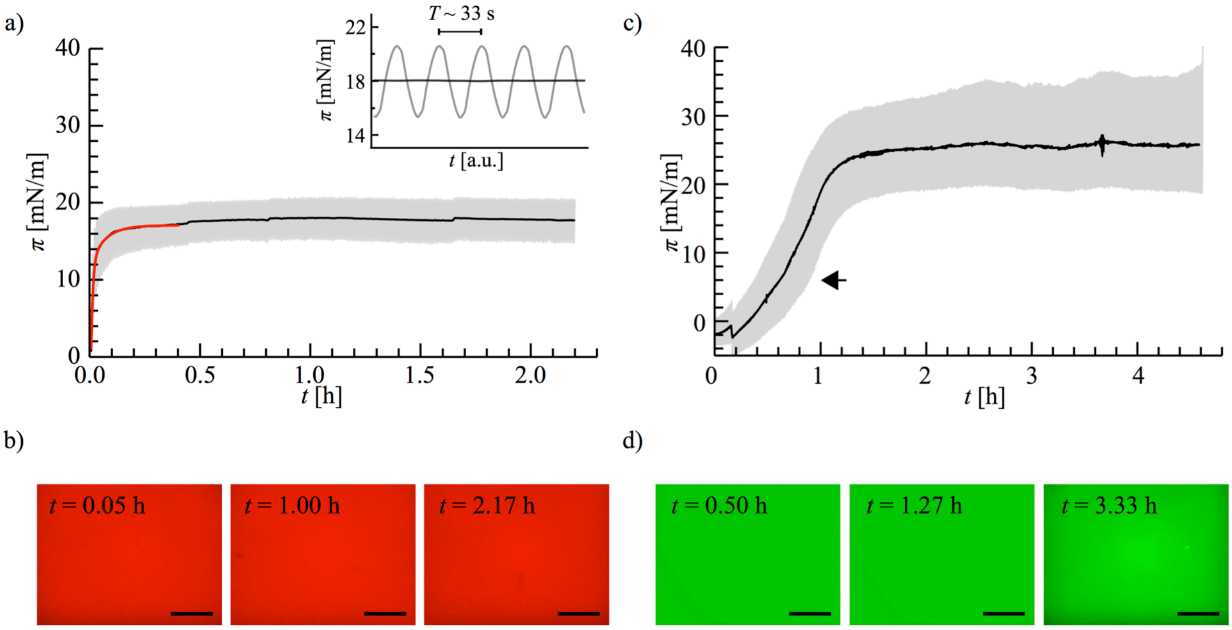

Figure 5.2.2. Adsorption of BSA and DPPC to the air/water interface under sinusoidal oscillations of the surface area. a) Surface pressure dynamics during the adsorption of BSA. The surface pressure (gray) changed periodically in correlation with the surface area oscillations (inset). The black curve represents the mean surface pressure. The adsorption kinetics was elucidated by an exponential fit (red curve). BSA was doped with 2 mol% BSA-Texas red to obtain b) Fluorescence micrographs of the BSA interfacial film at different time points. c) Surface pressure dynamics during the adsorption of DPPC. The arrow indicates a LE/LC phase transition at $\pi \sim 7$ mN/m. d) Fluorescence micrographs of the DPPC interfacial film doped with 0.03 mol% DHPE-Oregon green DPPC/ DHPE-Oregon green. Scale bar: 100 µm.

5.2.1 Adsorption Kinetics of Pure BSA and DPPC

Figure 5.2.2 shows the isotherms of pure BSA and DPPC (1 mM) studied under nitrogen atmosphere. In case of BSA, the surface pressure rapidly increased to a saturation value of $\pi_{sat} \sim 18$ mN/m within a few minutes after injection (Figure 5.2.2a), which is in good agreement with studies performed on an oscillating bubble interface [140]. In the plateau region a surface pressure amplitude of $\Delta\pi \sim 3$ mN/m was observed, which remained constant throughout the observation time. The isotherm could be fitted (red curve) with a sum of two exponential functions of the form $\pi(t) = a \cdot (1 - e^{-t/\tau})$, thus, yielding two characteristic adsorption times of $\tau_{BSA,1} \sim 12$ min and $\tau_{BSA,2} \sim 1$ min, corresponding to an average over 3 independent measurements. The result suggests that the increase in the surface pressure in case of BSA was governed by a slow and a fast process, which might be attributed to a slow adsorption of BSA to the interface followed by fast unfolding of the adsorbed proteins [141].

Figure 5.2.2b shows the temporal evolution of the surface pressure during the adsorption of DPPC from a 1mM vesicle dispersion to the oscillating air/water interface. The increase in the

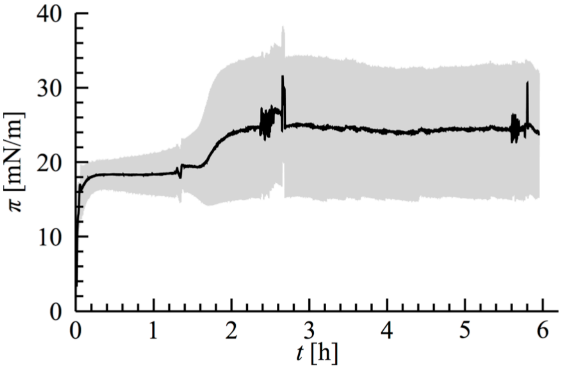

Figure 5.2.3. Surface pressure dynamics during the competitive adsorption of BSA and DPPC, presented as 1 mM vesicle dispersion, to an oscillating N_2/water interface. Gray "area" shows the changes in the surface pressure by time. The black line represents the mean surface pressure.

surface pressure was considerably slower compared to BSA. The mean surface pressure plateaued after approximately 1.5 h at $\pi_{sat} \sim 26$ mN/m with an maximum to minimum difference of □$\pi \sim 12$ mN/m, which increased slightly by time to ~ 16 mN/m, implying a change in the compressibility of the monolayer. The obtained saturation surface pressure was lower than the value observed previously using the bubble configuration ($\pi \sim 40$ mN/m [129, 142]). A threefold increase in DPPC concentration led only to a slight increase in the saturation surface pressure to ~ 27 mN/m but accelerated the adsorption significantly (Appendix IV). As indicated by the arrow in Figure 5.2.2c, the DPPC isotherm exhibited a kink at $t \sim 0.7$ h and $\pi \sim 7$ mN/m, which, although poorly pronounced, may indicate a phase transition of the DPPC monolayer from liquid expanded to liquid condensed phase (LE/LC). A dilute to condensed phase transition was reported for the bubble configuration after ~1 h and at a surface pressure ~ 20 mN/m [129, 142]. The discrepancies between the bubble tensiometric assay and the configuration used in this chapter might be attributed to the different experimental geometries as the Langmuir film balance provides a much larger surface area per volume of solution.

Furthermore, in order to track interfacial structural changes by time, BSA and DPPC were doped with BSA-Texas Red and DHPE-Oregon green, respectively. Fluorescence microscopy images taken at several time points during the experiment revealed homogeneous and featureless interfacial films throughout the observation time for both BSA and DPPC (Figure 5.2.2b and d).

5.2.2 Competitive Adsorption of BSA and DPPC

The competitive adsorption of BSA and DPPC was investigated by injecting both compounds simultaneously into the sub-phase. Figure 5.2.3 shows the surface pressure evolution when DPPC was presented in a concentration of 1mM. Early after the injection, the surface pressure dynamics was dominated by BSA adsorption ($\pi \sim 18$ mN/m). Remarkably, the surface pressure amplitude was observed to increase slowly by time, indicating a change in the compressibility of the interfacial film, which might be due to the adsorption of small amounts of DPPC [143] (see below). Eventually, at $t \sim 1.6$ h the mean surface pressure increased rapidly and plateaued at $\pi_{sat} \sim 25$ mN/m (maximum to minimum $\Delta\pi \sim 16$ mN/m) within ~ 40 min, indicating the displacement of BSA from the interface by DPPC. The competitive BSA/DPPC adsorption was also studied in the presence of 3 mM DPPC. Figure 5.2.4a shows the corresponding isotherm measured under a nitrogen atmosphere. In this case, the BSA displacement was considerably faster so that the increase in the mean surface pressure set in already at $t \sim 0.7$ h. Moreover, a higher plateau surface pressure of $\pi \sim 30$ mN/m was reached. Figure 5.2.4b shows fluorescence microscopy images of the corresponding BSA/BSA-Texas red interfacial film recorded at different time points. Interestingly, small dark domains appeared in the BSA film already at $t \sim 0.5$ h, i.e. 0.2 h before the mean surface pressure

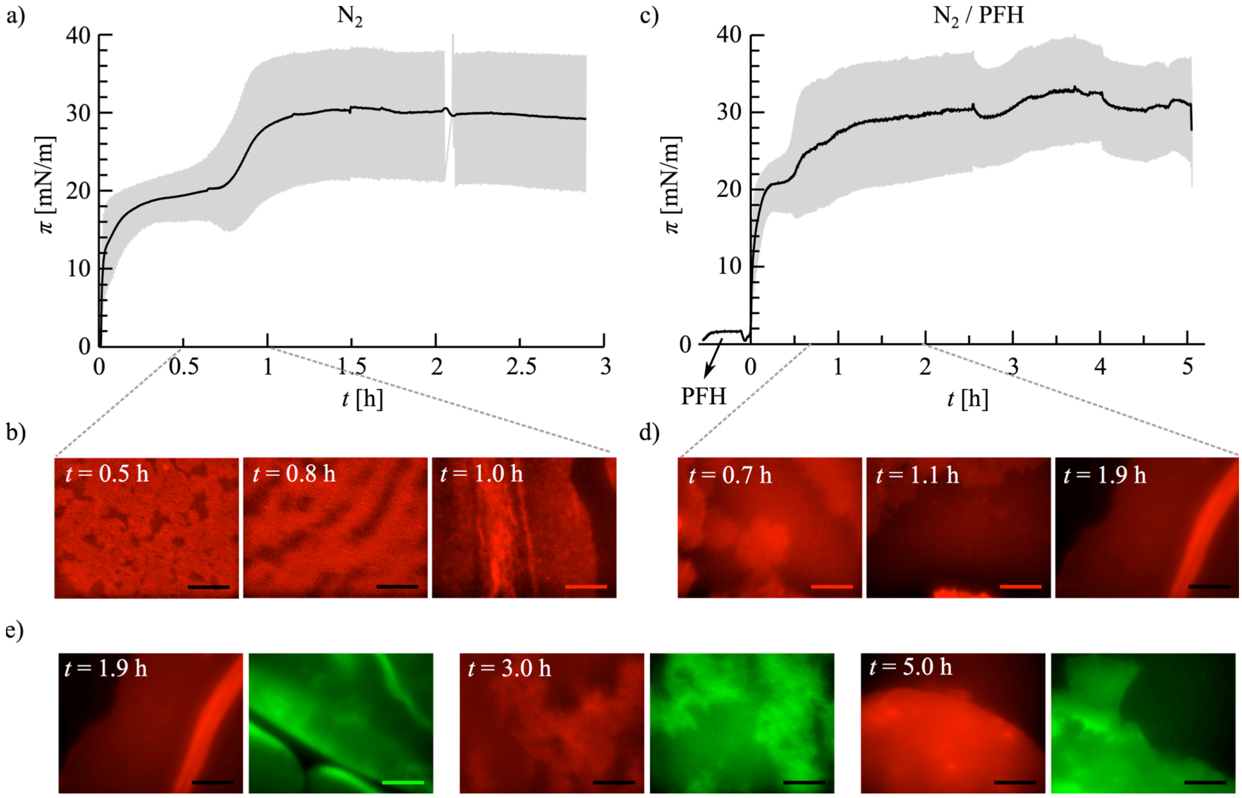

Figure 5.2.4. Competitive adsorption of BSA and DPPC ([DPPC] = 3 mM) a) temporal evolution of the surface pressure measured under a N_2 atmosphere. The structural changes of the interfacial layer by time are shown in b) fluorescence microscopy images of BSA/BSA-Texas red layer adsorbed at the N_2/water interface. c) Surface pressure as a function of time measured under a PFH saturated atmosphere. d) Fluorescence microscopy images showing the temporal changes of the structural BSA/BSA-Texas red interfacial film in the presence of PFH. e) Fluorescence microscopy images of BSA (red) and DPPC (green) taken at different time point in the second plateau region of isotherm shown in panel (c). Scale bar: 100 µm.

started to increase. These domains increased in size by time and can be ascribed to interfacial DPPC, explaining the increase in oscillation amplitude (see above). However, the nature of the domains could not be confirmed by the fluorescence signal of DPPC/DHPE-Oregon green due to the high fluorescence intensity of the sub-phase. Since the plateau surface pressure obtained with higher DPPC concentration (3 mM), was closer to the results obtained by bubble tensiometry [142], this concentration was used for the following experiments.

Next, in order to investigate the impact of PFH, the competitive adsorption of BSA and DPPC was studied under a PFH saturated nitrogen atmosphere. The gaseous phase was saturated with PFH by flushing the experimental chamber with a N_2/PFH stream for 30 min before the injection of the BSA/DPPC mixture into the sub-phase. PFH adsorbed to the liquid/gas interface resulting in a surface pressure of ~ 2 mN/m comparable to the saturation surface pressure of perfluorocarbon gases reported before [137, 138]. The corresponding isotherm is shown in Figure 5.2.4c. Figure 5.2.4d depicts fluorescence micrographs of the BSA/BSA-Texas Red interfacial film at different time points. Similar to the experiments under N_2 atmosphere, the surface pressure was first dominated by BSA adsorption. However, the plateau surface pressure was higher by ~ 2 mN/m ($\pi_{sat} \sim 21$ mN/m), which might be due to the coexistence of PFH with BSA at the interface. Moreover, the displacement of BSA by DPPC was considerably accelerate in comparison to N_2 atmosphere and observed at $t \sim 0.4$ h. The surface pressure finally reached $\pi_{sat} \sim 31$ mN/m. After BSA displacement, fluorescence microscopy revealed the presence of isolated plates and “islands” of both DPPC and BSA both in the presence and absence of PFH (Figure 5.2.4e).

5.2.3 Displacement of Pre-Adsorbed BSA by DPPC

To better understand how the intrusion of DPPC into a BSA layer is enhanced by PFH, the displacement of a pre-adsorbed BSA film was studied in this section in the presence and absence of PFH. For this purpose, BSA was first injected into the sub-phase and allowed to adsorb to the liquid/gas interface for 90 min before DPPC vesicle dispersion was added ([DPPC] = 3 mM). Figure 5.2.5 shows the isotherms obtained in the absence and presence of PFH. Corresponding fluorescence micrographs are shown in figure 5.2.6.

Under nitrogen atmosphere, the surface pressure remained constant for approximately 2 h after DPPC injection (Figure 5.2.5, gray curve). In this regime, a homogeneous and featureless BSA film was observed at the interface (Figure 5.2.6). At $t \sim 3.5$ h the surface pressure started to increase slowly. Simultaneously, dark DPPC domains appeared in the BSA film and grew in size by time (Figure 5.2.6 upper row). The surface pressure finally saturated at $\pi_{sat} \sim 27$ mN/m at $t \sim 7$ h. When the gas phase was saturated with PFH, the BSA

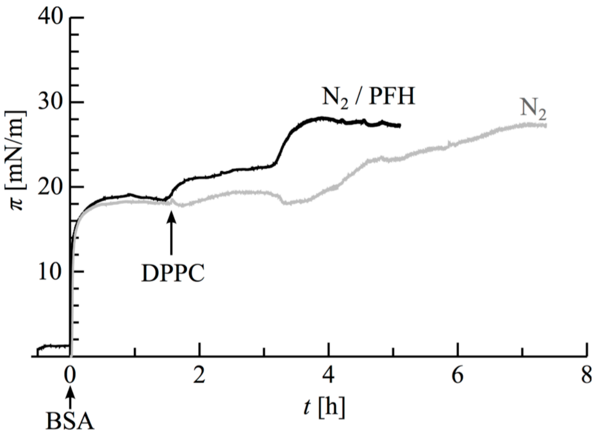

Figure 5.2.5. Displacement of pre-adsorbed BSA by DPPC in the absence (gray) and presence of PFH (black). BSA was injected into the sub-phase at t ~ 0 h (arrow) and allowed to adsorb to the interface for ~ 1.5 h before DPPC injection (arrow).

displacement was significantly accelerated. The surface pressure increased immediately after the injection of the DPPC dispersion (Figure 5.2.5, black curve) and plateaued at π_{sat} ~ 27 mN/m approximately 2 h later at t ~ 4 h. Fluorescence micrographs revealed the appearance of dark DPPC domains already at t ~ 2.3 h. These domains had a narrow and elongated shape in contrast to the broad and irregular domains observed before under N$_2$ atmosphere (Figure 5.2.6 lower row).

Figure 5.2.7 shows Lissajous plots obtained shortly before the injection of DPPC, i.e. at t ~ 1.3 h, in the absence and presence of PFH. In the absence of PFH, the stress-strain behavior of the BSA layer was almost symmetric during compression and expansion (Figure 5.2.7a). In contrast, in the presence of PFH the stress-strain relation was clearly anisotropic during compression and expansion of the film. The altered stress-strain hysteresis in the presence of PFH suggests a change in the viscoelastic properties of the pre-adsorbed BSA film due to the incorporation of PFH, which can promote the adsorption of DPPC.

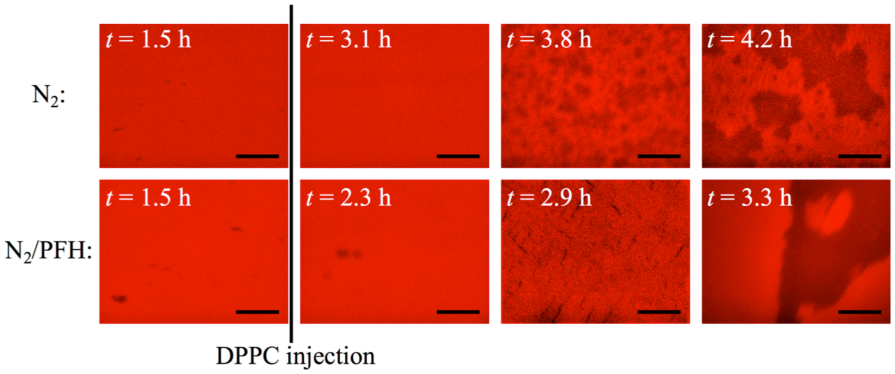

Figure 5.2.6. Fluorescence microscopy images showing displacement of a pre-adsorbed BSA film by DPPC in the absence (upper row) and presence of PFH (lower row).

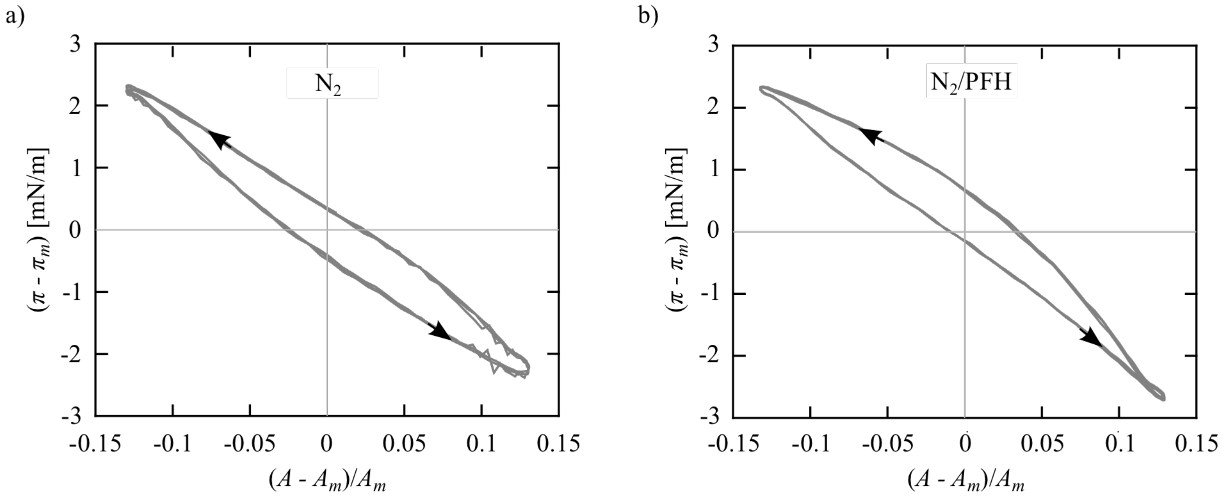

Figure 5.2.7. Lissajous figures of pre-adsorbed BSA in a) absence and b) presence of PFH obtained ~ 1.3 h after BSA injection. Each figure corresponds to 3 successive cycles. Arrows indicate the compression and expansion of the adsorbed layer. A_m and π_m correspond to the mean surface area and mean pressure, respectively.

It is noteworthy that both in presence and absence of PHF the displacement of the pre-adsorbed BSA from the interface is significantly slower compared to the competitive adsorption discussed in section 5.2.2. This might be attributed to the co-adsorption of small amounts of DPPC, when injected together with BSA, facilitating the further recruitment of DPPC during surface area expansion.

5.3 Summary

In the acute respiratory distress syndrome (ARDS) the leakage of serum proteins, like albumin, into the alveoli airspace inactivates the lunge surfactant.

In this chapter the reversion of BSA adsorption by DPPC was studied at an oscillating interface (T □ 33 s, □A = 15%) using a Langmuir film balance. By combing the Langmuir trough with an inverted microscope the impact of PFH on the interfacial processes was visualized by means of fluorescence microscopy. BSA-Texas red and DPPC-Oregon green were used for labeling.

In the first step, in section 5.2.1 the adsorption of pure BSA and DPPC was investigated. For BSA the adsorption isotherm was governed by a fast and slow process with the characteristic adsorption times $\tau_{BSA,1}$ ~ 10 min and $\tau_{BSA,2}$ ~ 1 min and reached saturation surface pressures of ~ 18 mN/m. The DPPC isotherm showed a sign of LE/LC phase transition after ~ 0.7 h. Afterwards the surface pressure increased to ~ 26 mN/m within approximately 1.5 h ([DPPC] = 1 mM), a threefold increase in DPPC concentration ([DPPC] = 3 mM) accelerated the adsorption process, reaching the equilibrium surface pressure after almost 0.5 h. Fluorescence microscopy revealed homogeneous and featureless interfacial films for both compounds.

In section 5.2.2 the competitive adsorption of BSA and DPPC was studied in the absence and presence of PFH by simultaneously injecting the two compounds into the sub-phase. In both cases, immediately after injection the surface pressure was dominated by BSA adsorption. Small DPPC domains appeared in the BSA film at $t \sim 0.5$ h, which grew in size by time. At $t \sim 1.6$ h the mean surface pressure sharply increased to $\pi \sim 30$ mN/m, which was ascribed to the displacement of BSA by DPPC. When the gaseous phase was saturated by PFH, PFH was found to adsorb to the interface. Moreover, the displacement was considerably accelerated ($t \sim 0.4$ h).

In section 5.2.3 the impact of PFH was studied on the displacement of pre-adsorbed BSA by DPPC. PFH was found to considerably accelerate the displacement of BSA. While the displacement set in ~ 2 h after injection of DPPC und N_2-atmosphere, in the presence of PFH the increase in the surface pressure was observed almost immediately after DPPC injection. Moreover, the DPPC domains were observed to be narrow and elongated in shape in the presence of PFH, whereas broad and irregularly shaped domains were found under N_2-atmosphere. The stress-strain relation of the pre-adsorbed BSA was found to alter in the presence of PFH, which was attributed to an incorporation of the PFH into the BSA layer.

5.4 Materials and Methods

5.4.1 Preparation of DPPC Dispersions

Highly concentrated dispersions of L-*α*-1,2-dipalmitoyl-*sn*-3-glycero-phosphatidylcholine (DPPC) ($26 \square 10^{-3}$ mol L^{-1}, 20 ml) (Lipoid, Ludwigshafen, Germany) were prepared in an aqueous HEPES buffer (20 mM HEPES, 150 mM NaCl, pH = 7.4) and tip sonicated for ~ 2 h until the dispersion became transparent. The size distribution of the vesicle suspension was determined by dynamic light scattering using a Zetasizer nanoseries instrument (Melvern Instruments, Malvern, United Kingdom).

5.4.2 Surface Pressure Measurements

Surface pressure/area isotherms were measured using a KSV NIMA Langmuir Minitrough (Biolin Scientific, Stockholm, Sweden) made of Teflon and equipped with two moving barriers and a glass window for microscopy. A water bath circulator was used to regulate the temperature at (37 ± 1)°C. The evaporated water was replaced continuously during the experiments. The Langmuir trough was enclosed in a Plexiglas chamber, equipped with gas in- and outlet. The Barriers were subjected to sinusoidal oscillations with a period of 33 s and surface area variation amplitude of 15%. For all experiments highly concentrated solutions of BSA (6.7×10^{-5} mol L^{-1}, 2 ml) (Sigma Aldrich, St. Louis, United states) and DPPC (26×10^{-3} mol L^{-1}, 20 ml) were prepared injected into the sub-phase yielding a final concentration of 7.5×10^{-7} mol L^{-1} for BSA and 3×10^{-3} mol L^{-1} for DPPC. For BSA/DPPC mixture isotherms, to investigate the competitive adsorption of BSA and DPPC at the interface, a set of experiments was conducted by simultaneous injection of BSA and DPPC. In this case an equivalent volume of the sub-phase was removed before injection of the concentrated sample solutions to keep the sub-phase volume constant. In a second set of experiments BSA was injected first into the HEPES sub-phase and allowed to adsorb to the interface. DPPC was added 90 min after the injection of BSA. Surface pressure was measured by means of a Wilhelmy-plate balance.

Saturation of atmosphere with *F*-hexane.

A flow of Nitrogen was led into the chamber through three subsequent washes with liquid *F*-hexane (Alfa Aesar, Thermo Fisher Scientific, Waltham, United States). *F*-hexane was allowed to adsorb at the interface for 30 min before BSA was injected into the subphase.

5.4.3 Fluorescence Microscopy

The Langmuir trough was mounted on an Eclipse TE2000-U Nikon microscope (Shinagawa, Japan). A X-Cite 120 Metal Halide lamp (Excelitas, Waltham, United States) was used as illumination source. The concentrated BSA solution was doped with 2 mol% of Texas Red conjugated BSA (Molecular Probes, Eugene, United States). DPPC was labeled with 0.03 mol% DHPE-Oregon green (Molecular Probes, Eugene, United States).

Chapter 6
Conclusions

Cells can sense and generate mechanical forces in their surrounding environments. In this study, the mechanical properties of dynamic biological interfaces have been investigated taking systems with different hierarchical levels, from lung surfactant models to regenerating whole tissues.

In chapter 3, the correlation between biophysical properties and function of the native extracelllular matrix (ECM) of freshwater polyp Hydra (mesoglea) was investigated during the process of the asexual self-reproduction. Despite of their simple body design, Hydra's mesoglea exhibits a high degree of similarity to vertebrate ECM. This makes it very feasible for the characterization of the whole mesoglea *ex vivo*, which is not possible by using other organisms. First, to elucidate the mesoscopic structure of hydra mesoglea, nano-focused grazing incidence small-angle X-ray scattering (nano-focused GISAXS) was performed on isolated mesoglea in directions parallel and perpendicular to the oral-aboral axis (OA-axis) in section 3.2.1. The scattering patterns revealed the structure of rod-like objects exhibiting a highly ordered, crystalline-like packing with a distorted hexagonal lattice, which could be attributed to Hydra fibrillar type I collagen (Hcol-I). The lattice parameters of the fibers in directions parallel $a_{\parallel} = (17.6 \pm 3.6)$ nm, $b_{\parallel} = (6.7 \pm 0.8)$ nm, $\gamma_{\parallel} = (97.1 \pm 2.4)°$ and perpendicular $a_{\perp} = (11.8 \pm 0.5)$ nm, $b_{\perp} = (4.3 \pm 0.4)$ nm and $\gamma_{\perp} = (100.3 \pm 9.3)°$ to the OA-axis, were only slightly distorted compared to vertebrate type I collagen fibers from rat-tail tendon. The structural anisotropy with respect to the OA-axis was ascribed to an intrinsic body design, supporting the extensive contractions and extensions of the body column along the axis. In section 3.2.2 the mechanical properties of Hydra mesoglea were probed along the OA-axis by means of nano-indentation using an atomic force microscope (AFM). By measuring the local elastic moduli as a function of relative distance from the foot, standardized elasticity maps were constructed for several mesogleas isolated from hydras of different ages and developmental stages. Sorting the elasticity maps as a function of Hydra's age revealed that freshly detached polyps exhibited a uniformly soft ($E = 40$-90 kPa) mesoglea. By time, during the maturation of the young polyps towards budding Hydras, mesoglea was slightly softened in the upper gastric region ($E \geq 15$ kPa), but stiffened in the lower body ($E \leq 120$ kPa), including the budding zone, where new buds appear during

Hydra's asexual reproduction. A quantitative proteome analysis revealed a close correlation between mesoglea mechanical patterns and protease expression profiles, implying that the mechanical remodeling of mesoglea is conducted by regulation of protease expression. Next, the change in ECM stiffness was studied in section 3.2.3 as a function of altered stem cell activity. For this purpose, Hydras were treated with alsterpaullone (Alp), an inhibitor of the β-catenin destruction complex, to increase the β-catenin level along the body column. Treated Hydras formed ectopic tentacles down the body column within 2-3 days. The mesoglea showed low elastic moduli in the upper body extending into the budding region ($\langle E \rangle \approx 35$ kPa), which increased slightly towards the foot ($\langle E \rangle \approx 60$ kPa). The results were found to be comparable to the overall mesoglea elasticity of β-catenin overexpressing mutant, suggesting that high ECM stiffness facilitates high stem cell activity.

In chapter 4, the mechanical properties of Hydra tissue fragments were elucidated during the early stages of regeneration (~ 3 - 5 h) using a two-fingered micro-robotic-hand, possessing an extremely high force sensitivity (~1 nN). First, in section 4.2.1 Hydra regenerates were compressed linearly to different force levels. The obtained stress-strain relation clearly indicated a linear elastic response within the applied strain levels ($\varepsilon < 0.15$), which yields an elastic modulus $E = (185 \pm 13)$ Pa and a Hookean spring constant $k = (8.1 \pm 0.7)$ mN/m of hydra tissues. Moreover, the stress relaxation curves measured at a constant strain could be fitted with the simple Maxwell model for viscoelastic materials yielding a characteristic relaxation time of $\langle \tau \rangle = (19 \pm 8)$ s. This enables one to calculate a viscous modulus of $\eta = E\langle \tau \rangle = (3.6 \pm 1.5)$ Pas, and the Stokes frictional coefficient $\gamma = k\langle \tau \rangle = (0.17 \pm 0.08)$ Ns/m. Next, in section 4.2.2 the force oscillations of a Hydra regenerate were tracked over time and compared to size fluctuation of a freely regenerating sample. The force oscillations showed a periodicity of $\Delta t = (45 \pm 5)$ s and a maximum-to-minimum difference of $\Delta F = (5 \pm 2) \times 10^{-8}$ N. Both periodicity and magnitude of force oscillations were found to be in good agreement with the size fluctuations of the free specimen ($\Delta t = (59 \pm 12)$ s and $\Delta r = (1.8 \pm 0.4)$ µm corresponding to $\Delta F = (3 \pm 1) \times 10^{-8}$ N). These findings clearly indicated that using the micro-robotic-hand the dynamic mechanical properties of actively deforming tissues can quantitatively be determined without disturbing the natural morphological dynamics.

In chapter 5, the impact of perfluorohexane (PFH) on the viscoelasticity of lipid-protein monolayers mimicking lung surfactant complexes was studied by dilational rheology. PFH draws attentions as a potential therapeutics for the acute respiratory distress syndrome (ARDS). The characteristic lung surfactant inactivation by serum proteins during ARDS was modeled by the adsorption of dipalmitoylphosphatidylcholine (DPPC) from a vesicle suspension to the oscillating interface (T □ 33 s, □A = 15%) of a Langmuir film balance in the presence of bovine serum albumin (BSA). In the first step (5.2.1), the adsorption of the pure components was investigated under a nitrogen atmosphere. The adsorption of DPPC was slower compared to BSA, reaching $\pi_{sat} \sim 26$ mN/m after ~ 1 h ([DPPC] = 1 mM). Moreover, the isotherm showed a sign of liquid expanded/liquid condensed phase transition after ~ 0.7 h at $\pi \sim 7$ mN/m. Next, the competitive adsorption of BSA and DPPC was studied (5.2.2). When DPPC vesicles and BSA were added simultaneously to the sub-phase, the adsorption of BSA was found to dominate the surface pressure early after injection. Saturation of the gas-phase with PFH resulted in the co-adsorption of PFH to the interface and accelerated the BSA displacement ($t \sim 0.4$ h). Remarkably, PFH facilitates the displacement of a pre-adsorbed BSA interfacial layer by DPPC (5.2.3). These findings were attributed to the incorporation of PFH into the BSA monolayer, which was also accompanied by an altered viscoelasticity of the interface, which explains the mechanism of interface softening in alveolar space.

To conclude, the combination of different experimental techniques, ranging from dilational rheology to micro-robotic finger devices, allows for the quantitative understanding on the dynamic regulation of biological interfaces across different length and time scales.

Appendix I

Mesoscopic Structural Order of Highly Uniform Domains of Fluorocarbon-Hydrocarbon Di-blocks Formed at the Air/Water Interface:

A Grazing Incidence Small-Angle X-Ray Scattering Study

Semifluorinated alkanes (SFAs) are purely hydrophobic but yet amphiphilic molecules that self-assemble into highly ordered patterns of monodisperse nano-domains, when spread at the air-water interface [144]. As the self-assembly is governed by the intermolecular interaction, the mesoscopic pattern of the Langmuir monolayers is determined by the molecular structure [144]. In this chapter, grazing incidence small angle X-ray scattering (GISAXS) is utilized to study the structure of different SFA monolayers at the air-water interface. By systematically varying hydro- and fluorocarbon chain length the impact of the each moiety on the monolayer structure is elucidated.

AI.1 Introduction

Semifluorinated alkanes (SFAs) are diblock copolymers of the form $C_nF_{2n+1}C_mH_{2m+1}$ (*FnHm*) that link a fluorocarbon with a hydrocarbon chain (Figure AI.1.1a). Fluorocarbons and hydrocarbons are highly incompatible and differ significantly in many physicochemical

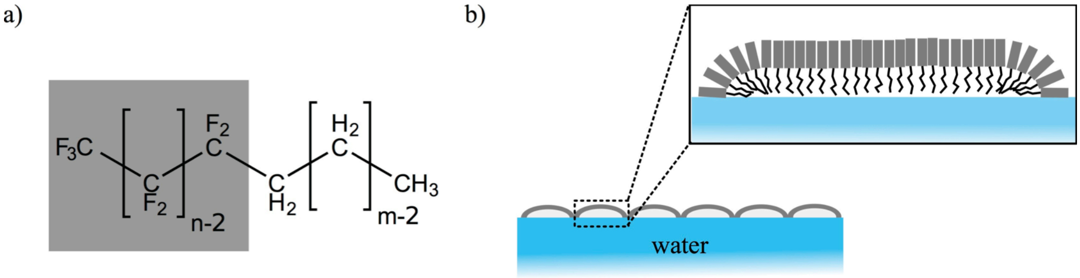

Figure AI.1.1. a) Molecular structure of semifluorinated alkanes, FnHm. b) Schematic representation of surface micelles formed by SFAs at the air-water interface. The molecules are oriented with the F-chain up and H-chain down.

properties [145, 146]. For example, fluorocarbon chains have, due to the larger steric requirements of fluorine, a larger cross sectional area (~ 27-30 Å^2 compared to ~ 18-21 Å^2 of hydrocarbon chains) and take a 15/7 helical conformation, which results in a rod-like and more rigid structure in contrast to the planar *all trans* conformation preferred by hydrocarbons [145, 146]. Moreover, the low polarizability of fluorine lowers the cohesive energy of fluorocarbon chains compared to their hydrogenated homologues [145, 146]. The two moieties also show different affinities as fluorocarbon chains are highly hydrophobic and lipophobic, while hydrocarbons show hydro- and fluorophobicity [145]. The combination of these two immiscible moieties lends SFAs an amphiphilic character. They form micelles in fluorocarbon and hydrocarbon solvents [146] as well as Gibbs film [147, 148] and even stable Langmuir monolayers at the air/water interface, despite the lack of any hydrophilic head groups [145].

A remarkable characteristic of SFA Langmuir monolayers is that they consist of highly monodisperse circular surface micelles that arrange in an ordered hexagonal lattice [144]. These domains have a diameter of $\Phi \sim$ 20-40 nm, which is several times larger than the molecular length (~ 2-3 nm) (Figure AI.1.1) [144]. This feature was first revealed by atomic force microscopy of Langmuir films of *F8H16* transferred to solid substrates [149] but the presence of the surface micelles at the air/water interface could later be proven using Grazing incidence small angle X-ray scattering (GISAXS) [150]. Similar nano-domains had also been reported for other partially fluorinated compounds like fluorinated carboxylic acids [151] or phosphonic acids [152]. X-ray and neutron reflectivity studies on *FnHm* Langmuir and Langmuir-Blodgett films showed that the molecules are oriented vertically with the F-chains up and the H-chains down and in contact with water [153-156], which is in accord with the higher hydrophobicity of fluorocarbon chains. Such a molecular orientation was also supported by surface potential measurements on Langmuir monolayers, revealing a negative surface potential for *FnHm* films [157-159]. However, the formation of other structures with an antiparallel orientation of the SFA molecules [160] as well as bilayers [161] had also been suggested.

Surface micelles were observed for *FnHm* monolayers transferred at surface pressures as low as $\pi \approx 0$ mN/m (*F8H16* and *F8H14*) [162]. Therefore, it was suggested that the self-assembly of the SFAs was driven in a surface concentration dependent manner rather than driven by the surface pressure [162]. Increasing the surface pressure resulted only in a more ordered and dense packing of the micelles but the domains did not shrink remarkably in size nor did they coalescence even at the “collapse pressure” π_c [162, 163]. Indeed compression of the monolayers beyond π_c led to formation of an additional layer on top of the preliminary formed carpet of hemi-micelle, while the surface micelles of the bottom layer remained intact throughout the compression [164, 165].

The properties of the Langmuir monolayers are sensitive to the molecular structure of the SFAs [155, 166]. For example, extending the length of *FnHm* molecules either by increasing the length of the F- or the H-chain was reported to increase the collapse pressure and the stability of the Langmuir films [157-159]. Extensive studies on Langmuir-Blodgett films of different SFAs revealed that the size of the nano-domains was also sensitive to the molecular length: for example, investigation of *F8Hm* (m = 14, 16, 18, 20) showed that the size of the surface hemi-micelles increased monotonically by increasing the hydrocarbon chain length [153, 163]. This finding was also confirmed by GISAXS studied on the corresponding Langmuir monolayers [167]. On the other hand, extending the F-chain length in *FnH16* (n= 6, 8, 10) did not affect the size of the surface micelles [153, 163]. It was also reported that the Langmuir-Blodgett films exhibited a fraction of elongated worm-like micelles coexisting with the circular ones [163]. The area fraction of these elongated micelles was reported to increase with the length of both the F- and the H-chain, reaching up to ~ 12% for *F8H20* [163]. However, most of these studies are based on characterization of the Langmuir-Blodgett films and might be affected by different molecule-substrate interactions or artifacts due to the transfer to solid substrates. But there have been almost no systematic studies addressing the impact of both hydro- and fluorocarbon chain lengths on the *FnHm* monolayer structures at the air/water interface.

In this chapter the structure of *FnHm* monolayers is studied at the air/water interface utilizing grazing incidence small angle X-ray scattering. By carefully modeling the form and structure factor the real-space structure of the homologue series *F8Hm* ($m = 4$, 16, 18, 20), *F10Hm* ($m = 16$, 18) and *FnH16* ($n = 8$, 10, 12) is investigated in order to elucidate the impact of the H- and F-chain lengths on the size and lateral order of the surface micelles. Moreover, the change in mesoscopic structure of the monolayers is tracked as a function of surface pressure.

AI.2 Results and Discussion

In order to investigate the correlation between the molecular length and the mesoscopic structure of *FnHm* Langmuir monolayers, three homologue series were studied: the impact of the H-chain length was addressed by 1) *F8Hm* with $m = 14, 16, 18, 20$ (Figure AI.2.1a) and 2) *F10Hm* with $m = 16, 18$ (Figure AI.2.1b, whereas the homologue series 3) *FnH16* with $n = 8, 10, 12$ (Figure AI.2.1c) was studied to elucidate the influence of the F-chain length. The corresponding π-A isotherms are illustrated in figure AI.2.1. For all compounds the onset of increase in surface pressure was found at a molecular area of 30-38 Å^2 close to the cross sectional area of the fluorocarbon chains (~ 27-30 Å^2). Moreover, the collapse pressure π_c ranged from ~ 10 mN/m for the shortest studied chain *F8H14* and increased with the length of the H- and F-chain, reaching ~ 20-22 mN/m for the longest studied SFAs *F12H16* and *F10H18* in good agreement with previous studies [157-159].

To determine the mesoscopic structure of *FnHm* monolayers at the air/water interface GISAXS was combined with the Langmuir trough technique. The experimental setup, which is schematically depicted in figure AI.2.2a, enabled the determination of structural changes during the monolayer compression over a wide range of surface pressures from $\pi = 0$ mN/m to near collapse pressures $\pi < \pi_c$ (Figure AI.2.2b). Figure AI.2.3a shows the scattering pattern of *F10H16* recorded at $\pi = 5$ mN/m as a representative example. The well-marked scattering pattern indicated a monolayer structure with a high crystalline-like lateral order in accord with previous reports [150, 165, 167]. To derive the monolayer structure in real space, the intensity profile along q_y, $I = I(q_y)$, was obtained by integrating the scattering intensity over the range

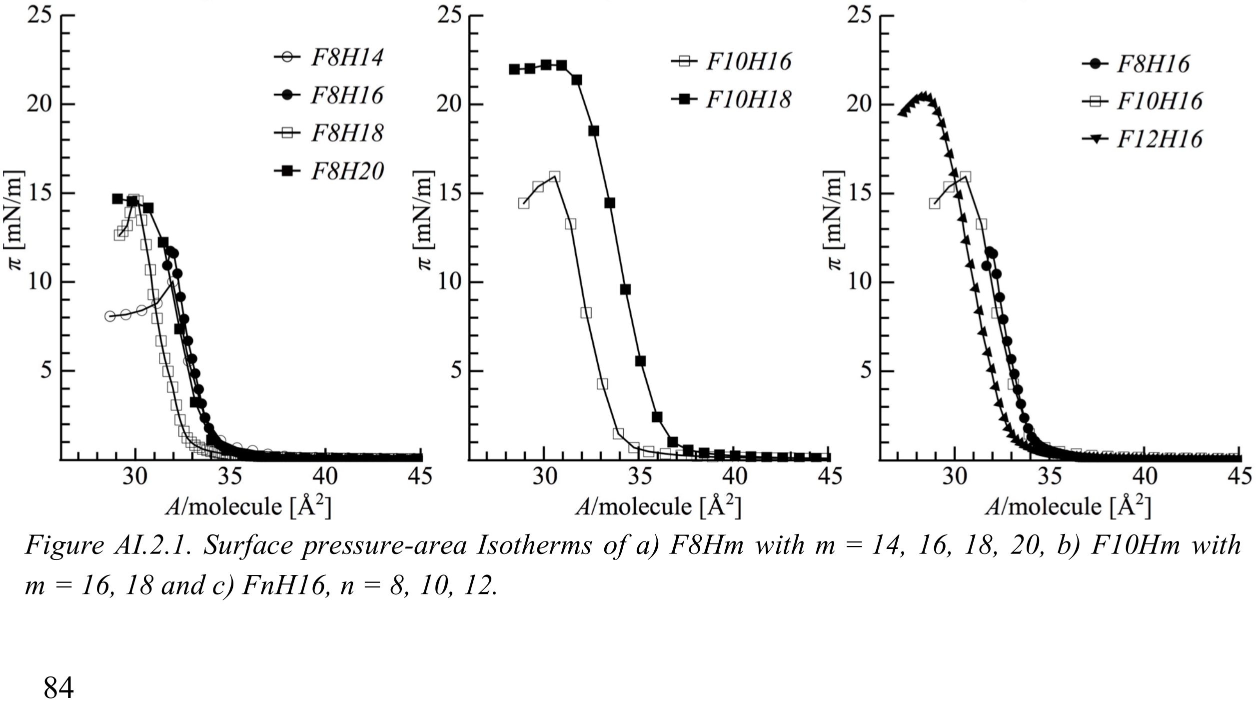

Figure AI.2.1. Surface pressure-area Isotherms of a) F8Hm with m = 14, 16, 18, 20, b) F10Hm with m = 16, 18 and c) FnH16, n = 8, 10, 12.

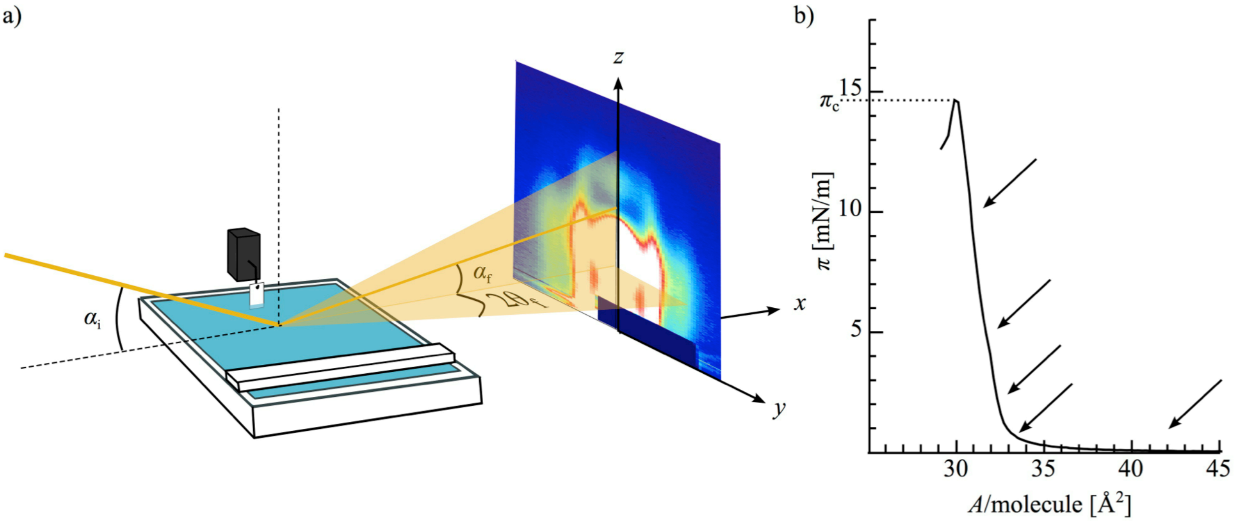

Figure AI.2.2. GISAXS of FnHm Langmuir monolayers at the air/water interface. A) Experimental setup. Langmuir monolayers of FnHm were prepared at the air/water interface of a Langmuir trough equipped with a moving barrier. The X-ray beam impinged on the interface at an incident angle α_i. Surface pressure was measured using the Wilhelmy-plate method. b) Surface pressure-area isotherm of F8H18. GISAXS patterns were collected at different surface pressures (arrows) up to the collapse pressure π_c.

$q_z = (0.8 \pm 0.1)$ nm^{-1} as indicated by the red lines in the 2D-pattern (Figure AI.2.3a). As mentioned in section 2.4, according to the relation $I(q_y) \propto |F(q_y)|^2 \cdot S(q_y)$, $I(q_y)$ is governed by contributions from 1) the surface micelle shape and size, which is described by the form factor $F(q_y)$ as well as 2) the lateral organization of the surface micelles at the interface, which is reflected by the structure factor $S(q_y)$. Based on this relation, the experimental data

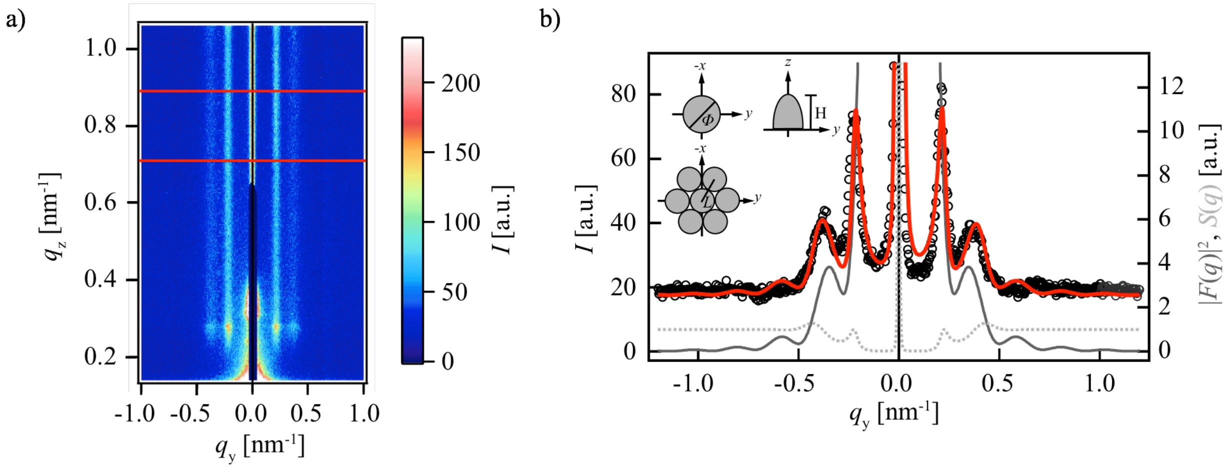

Figure AI.2.3. a) Scattering pattern of F10H16 monolayers obtained at a surface pressure of 5 mN/m. The scattering intensity was integrated over $q_z = (0.8 \pm 0.1)$ nm^{-1} indicated by the red lines to obtain b) the scattering intensity as a function of q_y (black circles). $I(q_y)$ was fitted using adequate models for the form factor (dark gray) and structure factor (broken light gray curve). The models are shown in the inset. The real space structural parameters were obtained from the best fit (red curve).

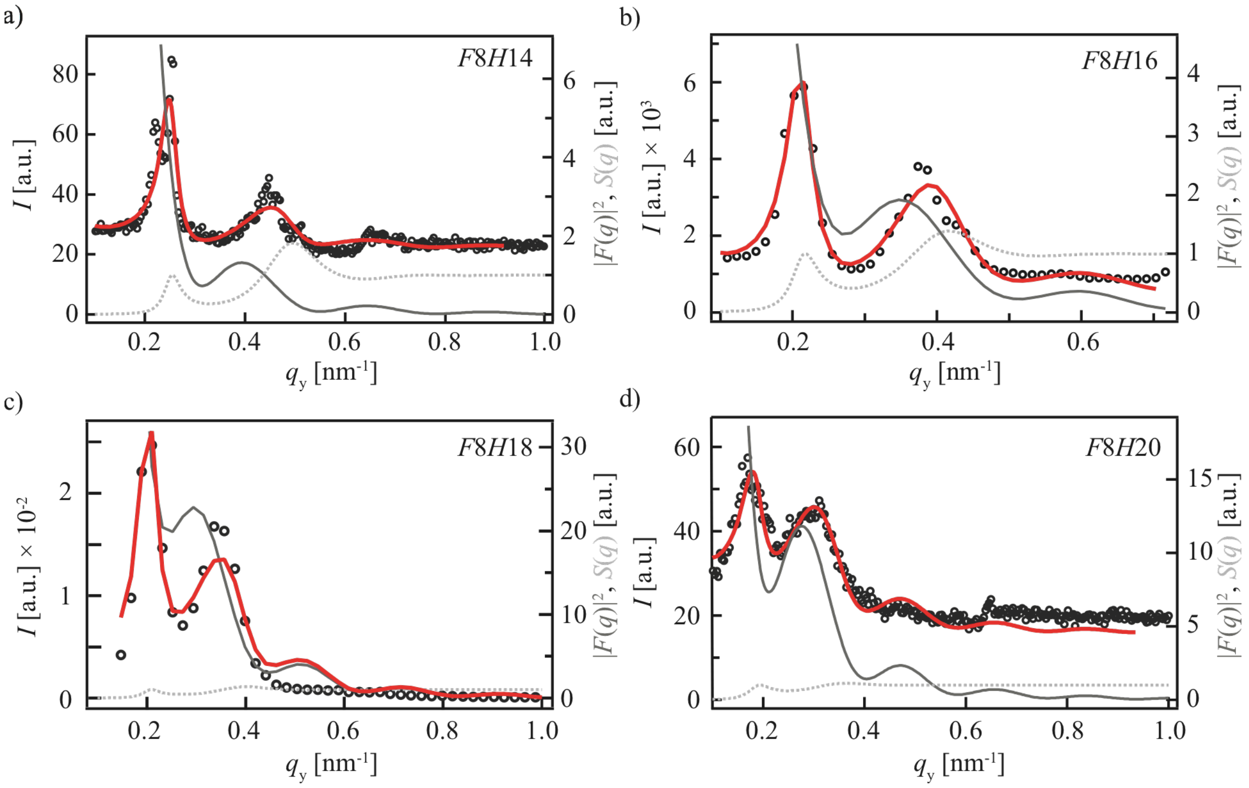

Figure AI.2.4. Integrated GSAXS intensity (black circles) measured at π = 5 mN/m and the best fit (red) for homologue aeries F8Hm:a) F8H14, b) F8H16, c) F8H18, d) F8H20. Form factor and structure factor contributions are represented by the dark gray and broken light gray curves, respectively.

were fitted by applying adequate models for $F(q_y)$ and $S(q_y)$ (Figure AI.2.3b): the hemi-micelles were considered to be monodisperse and modeled by the form factor of a hemispheroid with a diameter Φ and height H: $F(q_y) = F(q_y, \Phi, H)$ (Figure AI.2.3b inset). The form factor was further considered within the framework of the distorted wave Born approximation (DWBA) in order to account for multiple scattering events. The structure factor $S(q_y)$ was modeled by a 2D-hexagonal paracrystal with a lattice parameter L (Figure AI.2.3b inset). This model was chosen based on previous AFM and X-ray scattering studies [150, 163, 165, 167], which could also be confirmed by the relative positions of the scattering peaks.

AI.2.1 Impact of the molecular length on film structure

To better understand how changes in the F- or H-block length influence the mesoscopic structure of the monolayer, the *FnHm* monolayers were compared at a constant surface pressure of π = 5 mN/m. (Figure 7.2.4 and AI.2.5). The monolayer structures were compared with regard to 1) surface micelle size and 2) the short-range lateral order.

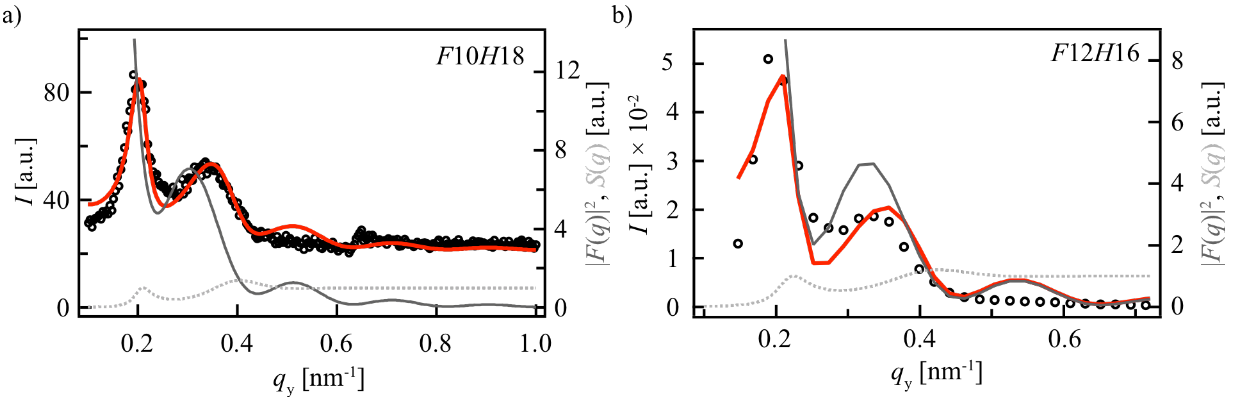

Figure AI.2.5. Integrated GSAXS intensity (black circles) measured at $\pi = 5$ mN/m and the best fit (red) for: a) F10H18, and b) F12H16. Form factor and structure factor contributions are represented by the dark gray and broken light gray curves, respectively.

1) Surface micelle size. Figure AI.2.6 summarizes the change in surface micelle diameter as a function of the (a) H-chain length, *m*, and (b) F-chain length, *n*. The increase in molecular length by extending either the H- or the F-chain led to an increase of the surface micelle diameter. In case of a constant F-chain ($n = 8$) (Figure AI.2.6a) the increase in the H-chain length from $m = 14$ to 20 was accompanied by an almost monotonic increase of surface micelle diameter from $\Phi_{F8H14} = (28 \pm 4)$ nm to $\Phi_{F8H20} = (37 \pm 6)$ nm, which is in good agreement with previous reports [163, 167], where the diameters was found to increase from $\Phi \approx 20$ nm at $m = 14$ to $\Phi \approx 35$ nm for $m = 20$. A similar tendency was also observed for the *F10H16*, $\Phi = (30 \pm 5$ nm), and *F10H18* $\Phi = (32 \pm 5$ nm). In comparison, at a constant H-chain length of $m = 16$ extending the F-chain length by 2 -CF$_2$- groups from $n = 8$ to 10 resulted in only a minor increase in micelle diameter from $\Phi_{F8H16} = (29 \pm 5)$ nm to $\Phi_{F10H16} = (30 \pm 5)$ nm but the addition of further 2 -CF$_2$- groups caused an increase in the surface micelle diameter to the value $\Phi_{F12H16} = (33 \pm 5)$ nm. This finding is in accord with Zhang et al., who reported that the domain size of *FnH16* was independent of the F-chain length for $n = 6$-10 [163].

The equilibrium domain radius is governed by the balance between 1) the line tension λ, which promotes the self-assembly of the molecules into nano-domains and 2) the dipole-dipole repulsive interaction [168]. McConnell suggested the equilibrium domain radius to be R_{eq} □ $exp(\lambda/\mu^2)$ with μ representing the difference in dipole density of the domain and its surrounding phases [168]. Since the dipole moment of *FnHm* molecules is mainly determined by the terminal CF$_3$ group and the CF$_2$-CH$_2$ junction between the hydro- and fluorocarbon blocks, it is supposed to be independent from the molecular length, which was supported by semi-empirical calculations as well as surface potential measurements [157, 169]. Thereafter, the increase in the domain size by increasing the H- and F-chain length can be attributed to an increase in the line tension due to the larger van der Waals interactions. In this context, the less pronounced impact of the F-chain length on the domain size might be ascribed to the lower polarizability of fluorocarbon compared to hydrocarbon chains.

2) Short-range lateral order. The influence of the molecular structure on the lateral order of the surface micelles was investigated by comparing the correlation length ξ. As mentioned in section 2.4, the structure factor can be considered as Fourier transformation of the real space pair correlation function $g(r)$, which can be used to determine the correlation length [170].

In the model of short-range order (SRO), the correlation length is given by

$$\xi = \frac{\langle d\rangle^3}{2\sigma^2} \tag{AI.1}$$

Where $\langle d\rangle$ represents the mean distance between two adjacent domains, which corresponds to the surface micelle diameter Φ, σ describes the root mean square standard deviation of $\langle d\rangle$ and corresponds to the width of the first correlation peak in $g(r)$ [170]. Using equation (AI.1) a correlation length of $\xi \approx$ 500-800 nm was obtained for the compounds studied at π = 5 mN/m (Figure AI.2.6). The correlation lengths obtained for the *F8Hm* series are considerably larger than the values reported previously by Bardin et al. ($\xi \approx$ 175-215 nm) [167]. It should also be noted that Bardin et al. calculated the values based on the scattering peak width using the Scherrer equation. But the method used in this study allows for a more advanced determination of the correlation length by eliminating any contributions from the form factor.

To better elucidate the impact of the H- or F-chain lengths on the monolayer packing order, the correlation lengths were normalized by the surface micelle diameter. The change in the normalized correlation length ξ/Φ as a function of hydrocarbon and fluorocarbon chain lengths is shown in figure AI.2.7 for the series (a) *F8Hm* and (b) *FnH16*, respectively. All monolayers showed correlation lengths of 18-24 times larger than a single domain diameter implying a high degree of lateral order. In the *F8Hm* series, the highest degree of correlation was observed for the shortest molecule *F8H14* with ξ/Φ = 24. Extending the hydrocarbon chain by two CH_2 groups to *F8H16* resulted in a decrease in the spatial correlation to ξ/Φ = 19. Further increase in the H-chain length to m = 18 and 20 did not remarkably affect the degree of correlation. A decrease in monolayer order by increasing the hydrocarbon chain length has also been reported for other partially fluorinated compounds like fluorinated alkanethiols (on water and gold substrates) [171, 172] and fluorinated double chain monomorpholinophophates [173] and can be attributed to an increase in the gauche defects of the hydrocarbon chain. On the other hand, at a constant H-block length of m = 16 the increase

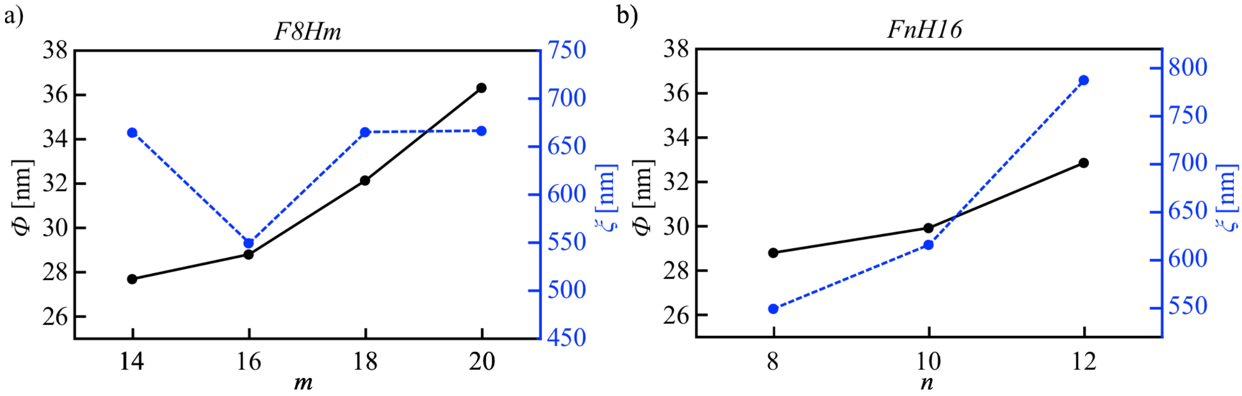

Figure AI.2.6. Change in surface micelle size (black) and correlation length (blue dashed line) as a function of a) hydrocarbon chain length, m, for the homologue series F8Hm and b) length of fluorocarbon chain n measured for FnH16. Error bars are skipped for the sake of clarity. See Figure AI.2.9 for errors.

in the F-chain length from $n = 8$ to 12 led to an almost monotonic increase of ξ/Φ. In this case the increase in the length of the rigid, rod-like F-chain increases the attractive van der Waals interactions leading to a higher lateral order.

It is noteworthy that previous AFM studies on Langmuir-Blodgett films showed the presence of elongated worm-like micelles dispersed among the circular domains [163]. Since the fraction and length of these micelles were also reported to increase with the molecular length [163], they might be considered as a source of disorder in the Langmuir monolayers. The fraction of the elongated micelles was also reported to decrease with increasing the surface pressure [163]. Thus, to verify if the observed decrease in correlation length might be attributed to the increase in elongated micelles, the scattering pattern of *F10H16* was compared at $\pi = 2$ mN/m and $\pi = 10$ mN/m (Figure AI.2.8). Although Zhang et al. reported a decrease in the area fraction of elongated micelles from ~ 10% at $\pi = 2$ mN/m to ~ 1.5% at $\pi = 10$ mN/m [153, 163], the scattering pattern did not show any significant change in the width of the first peak and

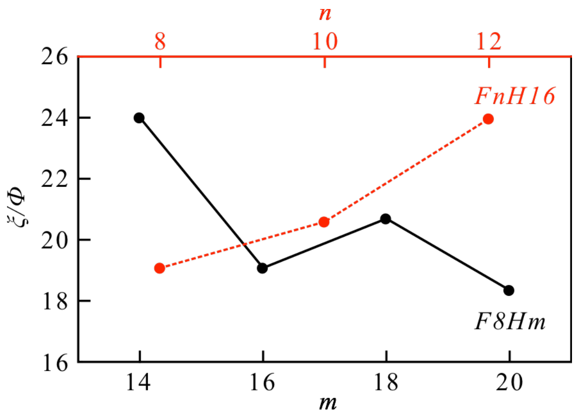

Figure AI.2.7. Correlation length ζ normalize by surface micelle diameter Φ as a function of the hydrocarbon chain length m (black, F8Hm) and fluorocarbon chain length (red dashed line: FnH16).

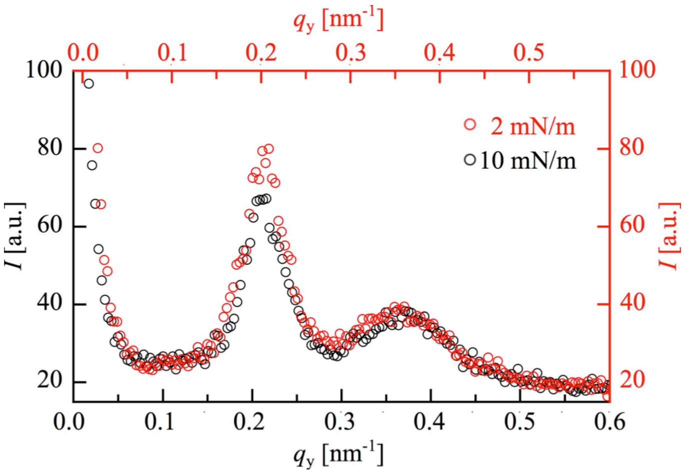

Figure AI.2.8. Integrated scattering intensity of F10H16 obtained at π = 2 mN/m (red circles) and 10 mN/m (black circles). The curves are slightly shifted relative to each other along q_y to overlap the first scattering peak for easier comparison.

hence the degree of lateral order (Figure AI.2.8). Hence, the formation of the elongated micelles might be, as suggested by Bardin et al. [167], ascribed to structural modifications due to the transfer of the monolayers to the solid substrate. Changes in the molecular conformational order upon transfer of monolayers to a solid substrate had been reported before for partially fluorinated fatty acids [174].

AI.2.2 "Rigidity" of surface micelles

The surface micelle diameter, Φ, was also analyzed as a function of the surface pressure for the three homologue series (Figure AI.2.9). All monolayers showed a ratio $L_h/\Phi = 0.8\text{-}1.0$ implying a closed packing of the surface micelles even at near zero surface pressures $\pi > 0$ mN/m. *F8H14*[*], *F8H20*, *F10H16* and *F12H16* showed regular scattering patterns even at $\pi = 0$ mN/m ($A \approx 76$ Å^2/molecule) ($L_h/\Phi = 0.7\text{-}0.85$). The formation of highly ordered surface micelle films at the air/water interface had been reported before but only for $\pi \geq 0.5$ mN/m [150, 167]. Moreover, only Langmuir-Blodgett films of *F8H14* and *F8H16* were observed to consist of hemi-micelles when transferred at 0 mN/m ($A \approx 41$ -49 Å^2/molecule) [162].

---

[*] Although *F8H14* showed regular scattering peaks at 0 mN/m, the Scattering data could not be fitted using the model introduced in this section. Therefore, the corresponding data point is not shown in Figure AI.2.9

The surface micelle size was almost independent from the surface pressure for all compounds studied in accord with previous reports [162, 167], implying that 1) the hemi-micelles were highly "rigid" and not markedly deformed during monolayer compression 2) the hemi micelles did not coalesce even at near "collapse" surface pressures; they stayed intact and retained their shape. The results indicate strong repulsive inter-domain interactions, which is consistent with the formation of highly ordered hexagonal lattices (see above). On the other hand, Fontaine et al. suggested that the coalescence of the hemi-micelle might be prevented by the presence of horizontally oriented molecules in the inter-micelle space [165]. The presences of such lying molecules was also proposed by Semenov et al. [175] but it could, to the knowledge of this author, not been proved so far.

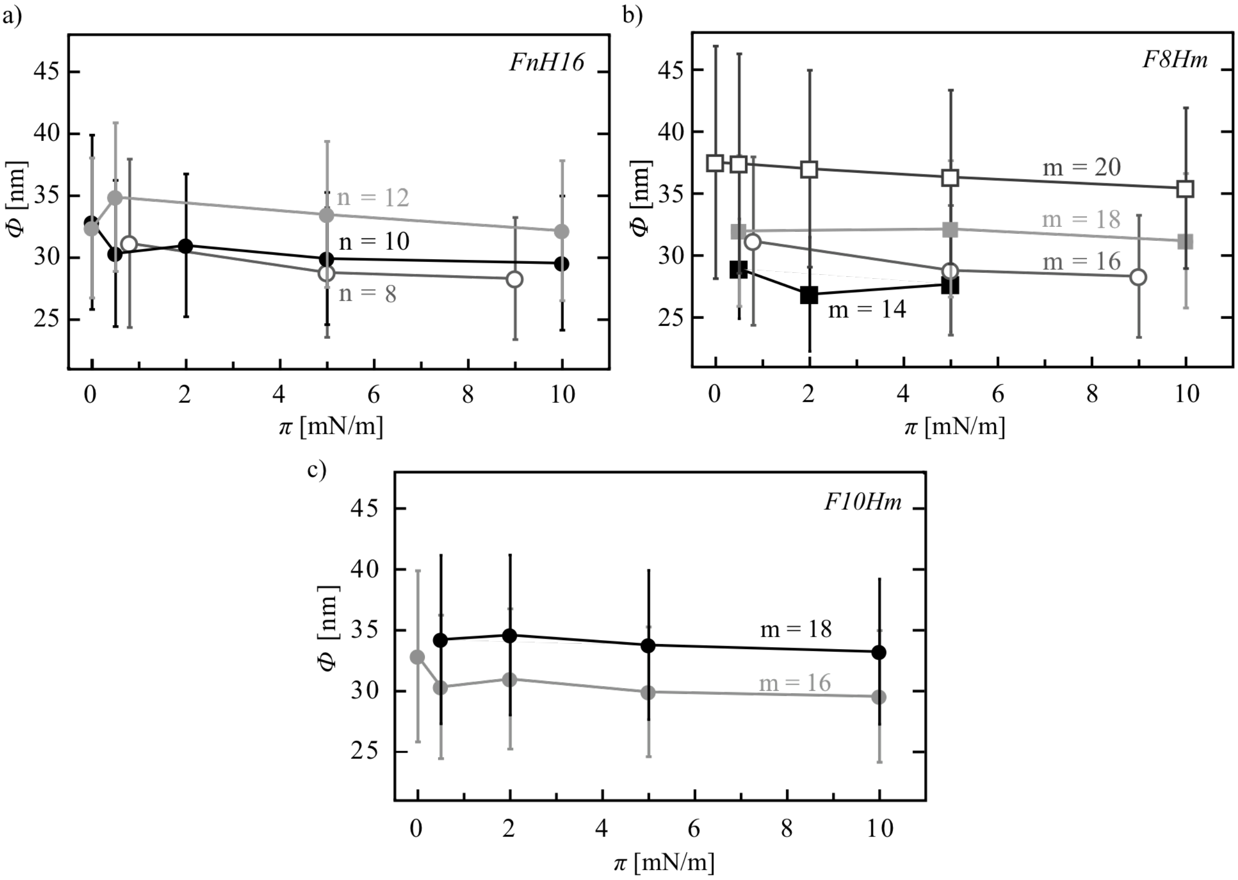

Figure AI.2.9. Change of surface micelle diameter Φ as a function of surface pressure π for the homologue series a) FnH16 (n = 8, 10,12), b) F8Hm (m = 14 ,16 ,18 ,20) and c) F10Hm (m = 16, 18).

AI.3 Summary

Semifluorinated alkanes FnHm are diblock copolymers with a weak amphiphilic character. When spread at the air/water interface, the molecules self-assemble into highly monodisperse nanometer sized surface micelles. In this chapter the impact of molecular length on the surface micelle size and organization was studied at the air/water interface by systematically varying the length of the hydrocarbon (*F8Hm* with m = 14, 16, 18, 20; *F10Hm* with m = 16, 18) or fluorocarbon (*FnH16* with n = 8, 10, 12) block length. The mesoscopic structure of the Langmuir monolayers was elucidated from the experimental scattering intensity by carefully modeling the form and structure factor to account for shape and organization of the micelles, respectively.

To shed light on the impact of the H- and F-block lengths the monolayer structures were compared at a constant surface pressure $\pi = 5$ mN/m. The results clearly showed a highly ordered crystalline-like hexagonal arrangement of circular surface micelles. It was found that increasing both the H- or F-chain length resulted to an increase in the surface micelle diameter Φ. For example, at a fixed F-chain length of $n = 8$ (*F8Hm*) the micelle diameter Φ increased from ~ 28 nm for *F8H14* to ~ 37 nm for *F8H20*. On the other hand, extending the F-chain length from *F8H16* to *F12H16* led to an increase in Φ from ~ 29 nm to ~ 33 nm. The increase in the surface micelle diameter was attributed to an increase in the line tension as a result of larger attractive van der Waals interactions between longer hydro- and fluorocarbon chains.

Moreover, the pair correlation functions were deduced from the structure factors in order to calculate the short-range correlation lengths ξ. The results revealed a high degree of spatial correlation for all studied *FnHm* monolayers showing correlation lengths of 18-24 times larger than a single domain size. Increasing the hydrocarbon length was found to result in a decrease in correlation degree ($\xi/\Phi \approx 24$ to $\xi/\Phi \approx 19$), which was attributed to an increase in the gauche defects of the longer H-chains. In contrast, increasing the F-chain length led to an almost monotonic increase in ξ/Φ from 19 for *F8H16* to 24 for *F12H16*. This tendency was ascribed to an increase in the van der Waals interactions between the fluorocarbon blocks.

The change in surface micelle diameter was also studied as a function of surface pressure. The domain size of all compounds was found to be independent from the surface pressure, implying a high rigidity of these nano-domains and strong repulsive inter-domain interactions.

AI.4 Materials and Methods

AI.4.1 Compounds

The compounds tested in this study: *F8H14*, *F8H16*, *F8H18*, *F8H20*, *F10H16*, *F10H18* and *F12H16* were synthesizes in the Laboratory of Professor M. P. Krafft at Institut Charles Sadron (Strasbourg, France).

AI.4.2 GISAXS experiments

GISAXS experiments were performed at the European Synchrotron Radiation Facility (ESRF, Grenoble, France) at the beam line ID10B on a dedicated film balance with a surface area of $A_S \approx 692$ cm^2 and equipped with a moveable barrier. The trough was enclosed in a gastight box and all experiments were performed in a Helium atmosphere and at room temperature. The surface pressure was measured using the Wilhelmy-plate method. The monolayers were prepared by spreading $v = 150$ µl of a 1 mM solution of *FnHm* in chloroform on the water sub-phase. The solvent was allowed to evaporate for several minutes. The surface area was compressed with a speed of ~ 34 mm^2/s. The surface pressure was kept constant during GISAXS measurements. The interface was impinged with a monochromatic X-ray beam of 10 keV and at an incident angle of 0.2° (*F8H14*, *F8H16*, *F8H20*, *F10H16*, *F10H18*) or 8 keV at an incident angle of 0.12° (*F8H18*, *F12H16*). The scattering intensity was detected using either a linear Gabriel Detector (*F8H18*, *F12H16*) or 2D-pixel detectors: Pilatus (*F8H16*) and MaxiPix (*F8H14*, *F8H20*, *F10H18*, *F10H16*). The background scattering was measured on a pure water sub-phase.

AI.4.3 Data analysis

After background subtraction, scattering patterns were analyzed by the software package FitGISAXS [176] using IGOR PRO. The scattering profile along q_y was averaged over a range $q_z = (0.8 \pm 0.1)$ nm^{-1}. The obtained scattering intensity profiles were fitted within the distorted wave born approximation using a hexagonal paracrystal of monodisperse hemispheroids as a model for the *FnHm* monolayers. Structure $S(q_y)$ and form factor $F(q_y)$ were obtained from the best fit.

Appendix II

List of Abbreviations

AFM	Atomic Force Microscopy
ALF	Alveolar Lining Fluid
Alp	Alsterpaullone
ANOVA	Analysis of Variance
ARDS	Acute Respiratory Distress Syndrome
BA	Born Approximation
BSA	Bovine Serum Albumin
β-cat	β-Catenin
DA	Decoupling Approximation
DHPE	1,2-Dihexadecanoyl-*sn*-Glycero-3-Phosphoethanolamine
Dlp-1	Dickkopf-like Protein 1
DLS	Dynamic Light Scattering
DPPC	Dipalmitoylphosphatidylcholine
DTT	Dithiothreitol
DWBA	Distorted Wave Born Approximation
ECM	Extracellular Matrix
GISAXS	Grazing Incidence Small Angle X-Ray Scattering
Gly	Glycine
gPFC	Perfluorocarbon Gas
GSK3	Glycogen Synthase Kinase 3
Hcol-I	Hydra Collagen Type I
Hepes	4-(2-hydroxyethyl)-1-piperazineethanesulfonic acid
Hyβ-cat	Hydra β-Catenin
LC	Liquid Chromatography
LE/LC transition	Liquid expanded-Liquid Condensed transition
LMA	Local Monodisperse Approximation
LS	Lung Surfactant
LTQ	Linear Trap Quadrupole
MMP	Matrix Metalloproteinase

MS	Mass Spectrometry
MS/MS	Tandem Mass Spectrometry
NRDS	Neonatal Respiratory Distress Syndrome
OA-Axis	Oral-Aboral Axis
PDMS	Polydimethylsiloxane
PFC	Perfluorocarbon
PFH	Perfluorohexane
PZT	Piezoelectric Translator
SILAC	Stable Isotope Labeling with Amino acids in Cell culture
SFA	Semi-Fluorinated Alkane
SPE	Solid Phase Extraction
SSCA	Size-Spacing Correlation Approximation
TFA	Trifluoroacetic acid
Tris.HCl	Tris(hydroxymethyl)aminomethane hydrochloride
Wnt-Signaling	Wingless Integrated Signaling

Appendix III

Supporting Information to Chapter 3

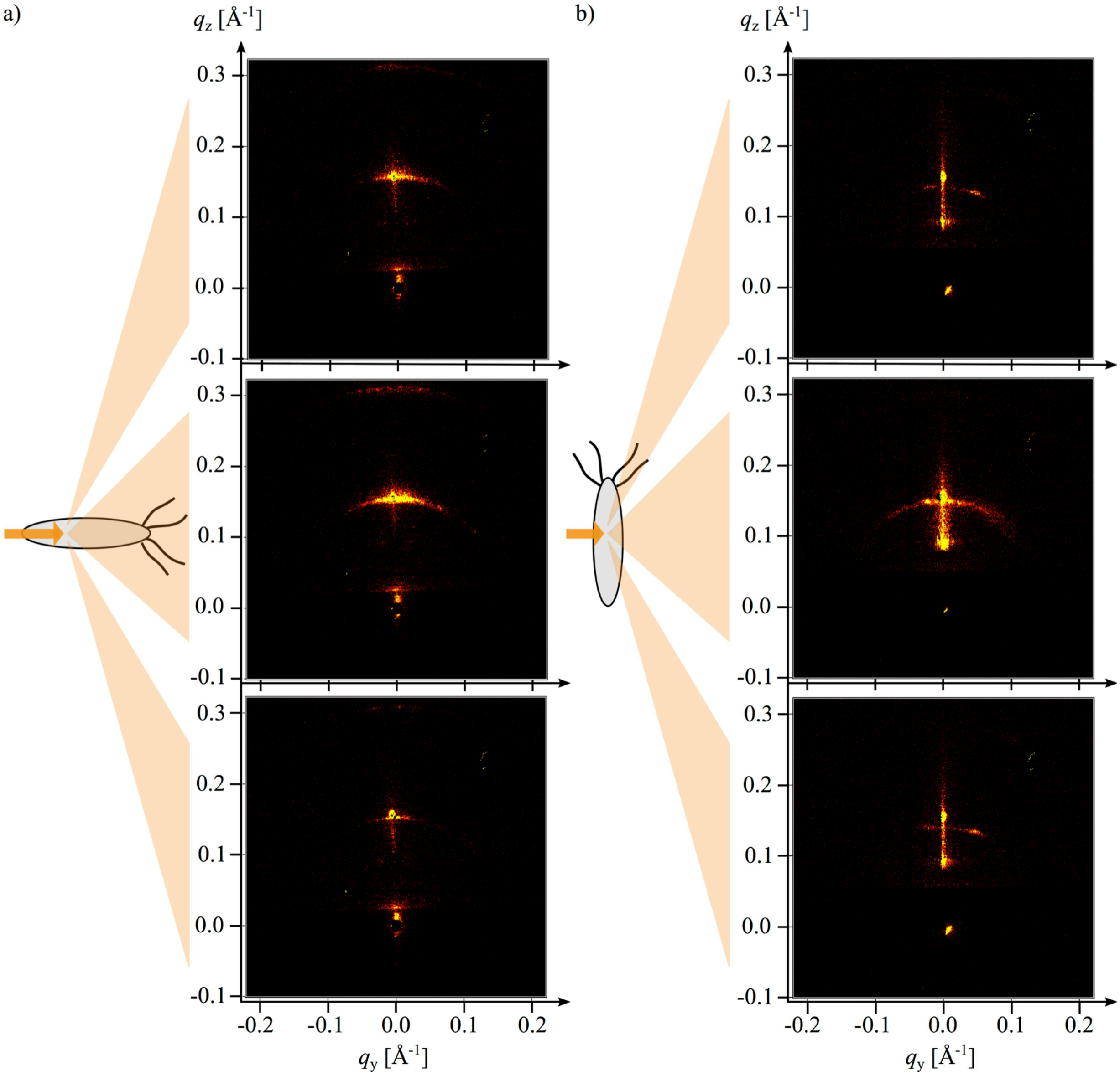

Figure AIII.1. Scattering patterns of hydra mesoglea obtained with beam (orange arrow) a) parallel and b) perpendicular to the main body axis. The patterns showed arcs concentrically arranged around the direct beam (q_y,q_z) *= (0,0) suggesting a highly ordered crystalline-like packing order.*

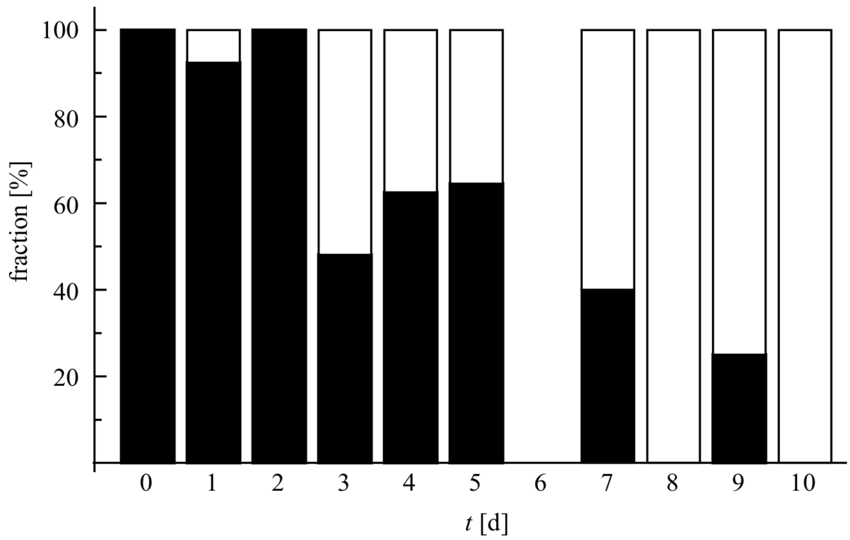

Figure AIII.2. Budding rate of daily fed Hydra magnipapillata as a function of age. Zero time point corresponds to the detachment of the matured bud from the parent. Black: Hydras with no apparent bud; White: Hydras with buds at stage 3 or higher.

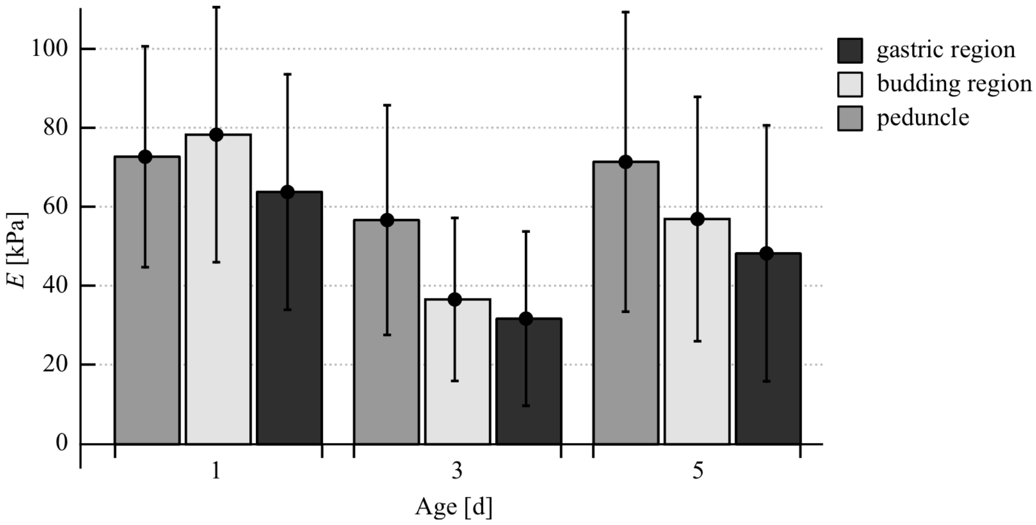

Figure AIII.2. Temporal evolution of the mean elastic modulus of the gastric region, budding region and peduncle of alsterpaullone treated Hydras at $t = 1$ *d (*$n = 5$*)* $t = 3$ *d (*$n = 6$*) and* $t = 5$ *d (*$n = 6$*)*

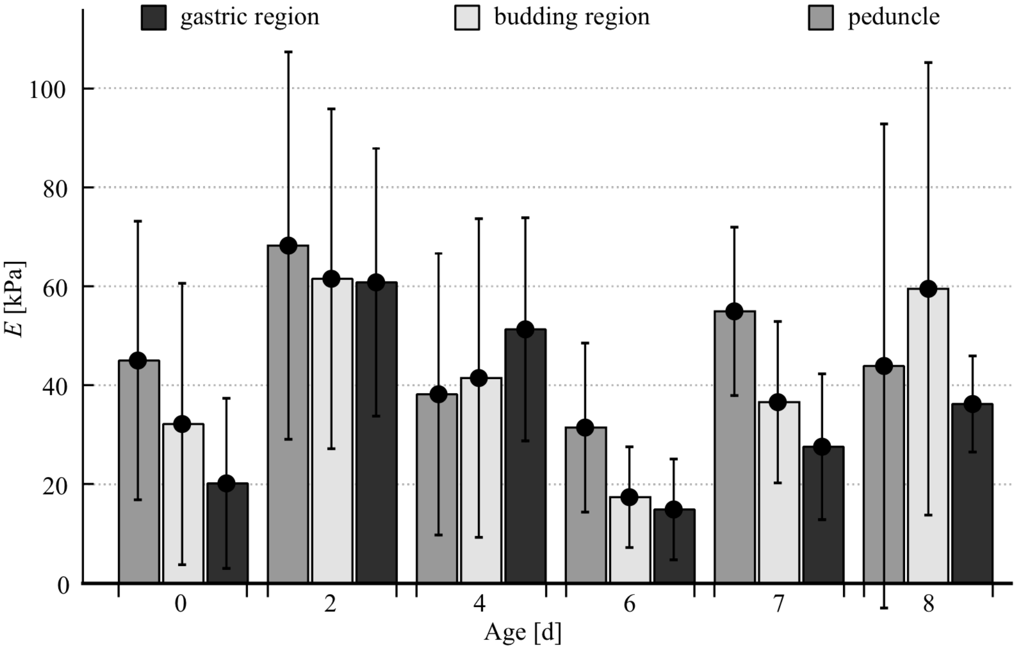

Figure AII.3. Temporal evolution of the mean elastic modulus of the gastric region, budding region and peduncle of β-catenin overexpressing Hydras. The values correspond to an average over 2-6 elasticity patterns for each age class.

Appendix IV

Supporting Information to Chapter 5

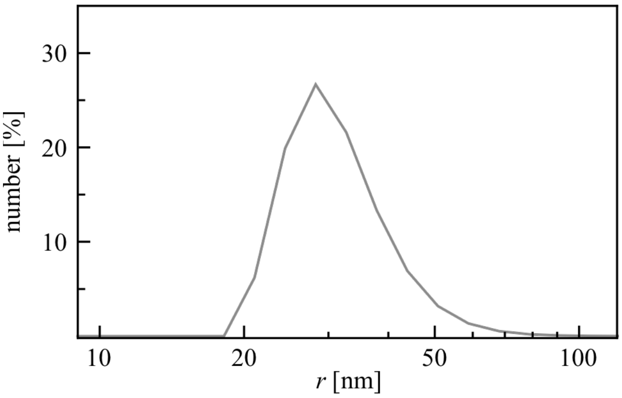

Figure AIV-1. Representative size distribution of a 3 mM DPPC vesicle dispersion obtained by DLS.

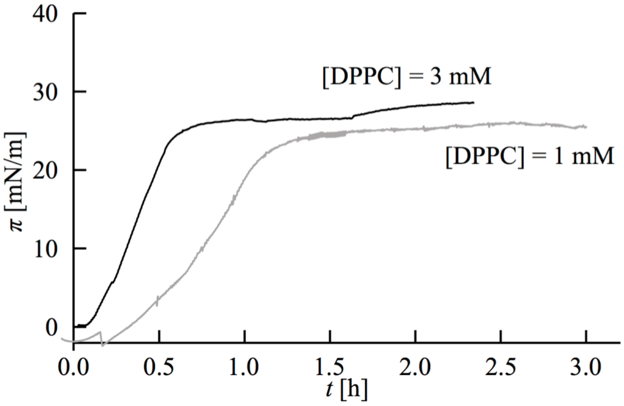

Figure AIV-2. Surface pressure dynamics during adsorption of DPPC to an oscillating air-water interface from an 1 mM (gray) and an 3 mM (black) vesicle dispersion.Only the mean surface pressure is shown.

References

1. Mammoto, T., A. Mammoto, and D.E. Ingber, *Mechanobiology and Developmental Control.* Annual Review of Cell and Developmental Biology, 2013. **29**(1): p. 27-61.
2. Ingber, D.E., *Cellular mechanotransduction: putting all the pieces together again.* The FASEB Journal, 2006. **20**(7): p. 811-827.
3. Humphrey, J.D., E.R. Dufresne, and M.A. Schwartz, *Mechanotransduction and extracellular matrix homeostasis.* Nat Rev Mol Cell Biol, 2014. **15**(12): p. 802-812.
4. Ng, M.R., et al., *Substrate stiffness regulates cadherin-dependent collective migration through myosin-II contractility.* The Journal of Cell Biology, 2012. **199**(3): p. 545-563.
5. Navaro, Y., et al., *Matrix stiffness determines the fate of nucleus pulposus–derived stem cells.* Biomaterials, 2015. **49**: p. 68-76.
6. Zeng, Y., et al., *Substrate stiffness regulates B-cell activation, proliferation, class switch, and T-cell-independent antibody responses in vivo.* European Journal of Immunology, 2015. **45**(6): p. 1621-1634.
7. Wang, Y., et al., *Substrate stiffness regulates the proliferation, migration, and differentiation of epidermal cells.* Burns, 2012. **38**(3): p. 414-420.
8. Chaudhuri, O., et al., *Substrate stress relaxation regulates cell spreading.* Nature Communications, 2015. **6**: p. 6365.
9. Ivanovska, I.L., et al., *Stem cell mechanobiology: diverse lessons from bone marrow.* Trends in Cell Biology, 2015. **25**(9): p. 523-532.
10. Evans, N.D., et al., *Substrate stiffness affects early differentiation events in embryonic stem cells.* Eur Cell Mater, 2009. **18**(1): p. e13.
11. Chowdhury, F., et al., *Soft Substrates Promote Homogeneous Self-Renewal of Embryonic Stem Cells via Downregulating Cell-Matrix Tractions.* PLoS ONE, 2010. **5**(12): p. e15655.
12. Engler, A.J., et al., *Matrix Elasticity Directs Stem Cell Lineage Specification.* Cell, 2006. **126**(4): p. 677-689.
13. Booth, A.J., et al., *Acellular Normal and Fibrotic Human Lung Matrices as a Culture System for In Vitro Investigation.* American Journal of Respiratory and Critical Care Medicine, 2012. **186**(9): p. 866-876.
14. Bonnans, C., J. Chou, and Z. Werb, *Remodelling the extracellular matrix in development and disease.* Nature Reviews: Molecular Cell Biology, 2014. **15**(12): p. 786-801.
15. Heller, E. and E. Fuchs, *Tissue patterning and cellular mechanics.* The Journal of Cell Biology, 2015. **211**(2): p. 219-231.
16. Brouzés, E. and E. Farge, *Interplay of mechanical deformation and patterned gene expression in developing embryos.* Current Opinion in Genetics & Development, 2004. **14**(4): p. 367-374.
17. Hammerschmidt, M. and D. Wedlich, *Regulated adhesion as a driving force of gastrulation movements.* Development, 2008. **135**(22): p. 3625.
18. Farge, E., *Mechanical Induction of Twist in the Drosophila Foregut/Stomodeal Primordium.* Current Biology, 2003. **13**(16): p. 1365-1377.

19. Kumar, A. and G.V. Shivashankar, *Mechanical Force Alters Morphogenetic Movements and Segmental Gene Expression Patterns during Drosophila Embryogenesis.* PLoS ONE, 2012. **7**(3): p. e33089.
20. Otto, J.J. and R.D. Campbell, *Budding in Hydra attenuata: Bud stages and fate map.* Journal of Experimental Zoology, 1977. **200**(3): p. 417-428.
21. Aufschnaiter, R., et al., *In vivo imaging of basement membrane movement: ECM patterning shapes Hydra polyps.* Journal of Cell Science, 2011. **124**(23): p. 4027-4038.
22. Mammoto, A., T. Mammoto, and D.E. Ingber, *Mechanosensitive mechanisms in transcriptional regulation.* Journal of Cell Science, 2012. **125**(13): p. 3061-3073.
23. Kominami, T. and H. Takata, *Gastrulation in the sea urchin embryo: A model system for analyzing the morphogenesis of a monolayered epithelium.* Development, Growth & Differentiation, 2004. **46**(4): p. 309-326.
24. Takata, H. and T. Kominami, *Shrinkage and Expansion of Blastocoel affect the Degree of Invagination in Sea Urchin Embryos.* Zoological Science, 2001. **18**(8): p. 1097-1105.
25. Takata, H. and T. Kominami, *Ectoderm exerts the driving force for gastrulation in the sand dollar Scaphechinus mirabilis.* Development, Growth & Differentiation, 2001. **43**(3): p. 265-274.
26. Soriano, J., et al., *Mechanogenetic Coupling of Hydra Symmetry Breaking and Driven Turing Instability Model.* Biophysical Journal, 2009. **96**: p. 1649.
27. Tanikawa, T. and T. Arai, *Development of a micro-manipulation system having a two-fingered micro-hand.* Robotics and Automation, IEEE Transactions on, 1999. **15**: p. 152.
28. Mammoto, T. and D.E. Ingber, *Mechanical control of tissue and organ development.* Development, 2010. **137**(9): p. 1407.
29. Joshi, S. and S. Kotecha, *Lung growth and development.* Early Human Development, 2007. **83**(12): p. 789-794.
30. Hashim, E., et al., *Reversible tracheal obstruction in the fetal sheep: Effects on tracheal fluid pressure and lung growth.* Journal of Pediatric Surgery. **30**(8): p. 1172-1177.
31. Zuo, Y.Y., et al., *Current perspectives in pulmonary surfactant — Inhibition, enhancement and evaluation.* Biochimica et Biophysica Acta (BBA) - Biomembranes, 2008. **1778**(10): p. 1947-1977.
32. Krafft, M.P., *Overcoming inactivation of the lung surfactant by serum proteins: a potential role for fluorocarbons?* Soft Matter, 2015. **11**(30): p. 5982-5994.
33. El-Gendy, N., et al., *Delivery and performance of surfactant replacement therapies to treat pulmonary disorders.* Therapeutic Delivery, 2013. **4**(8): p. 951-980.
34. *Chapter 1 Introduction*, in *Rheology for Chemists: An Introduction (2)*. 2008, The Royal Society of Chemistry. p. 1-13.
35. Fung, Y.C., *The Meaning of the Constitutive Equation*, in *Biomechanics: Mechanical Properties of Living Tissues*. 1981, Springer New York: New York, NY. p. 22-61.
36. *Stress and Strain Analysis and Measurement*, in *Polymer Engineering Science and Viscoelasticity: An Introduction*. 2008, Springer US: Boston, MA. p. 15-54.
37. *Characteristics, Applications and Properties of Polymers*, in *Polymer Engineering Science and Viscoelasticity: An Introduction*. 2008, Springer US: Boston, MA. p. 55-97.
38. *Chapter 4 Linear Viscoelasticity I: Phenomenological Approach*, in *Rheology for Chemists: An Introduction (2)*. 2008, The Royal Society of Chemistry. p. 92-134.
39. *Differential Constitutive Equations*, in *Polymer Engineering Science and Viscoelasticity: An Introduction*. 2008, Springer US: Boston, MA. p. 159-200.

40. Leite, F., et al., *The atomic force spectroscopy as a tool to investigate surface forces: Basic principles and applications.* Méndez-Vilas A and Díaz J. Modern Research and Educational Topics in Microscopy. Formatex, 2007: p. 747-757.
41. Moreno-Herrero, F. and J. Gomez-Herrero, *AFM: Basic Concepts*, in *Atomic Force Microscopy in Liquid*. 2012, Wiley-VCH Verlag GmbH & Co. KGaA. p. 1-34.
42. Butt, H.-J., B. Cappella, and M. Kappl, *Force measurements with the atomic force microscope: Technique, interpretation and applications.* Surface Science Reports, 2005. **59**(1–6): p. 1-152.
43. *A practical guide to AFM force spectroscopy and data analysis*. JPK Instruments: Technical Note. JPK Instruments AG.
44. Baró, A.M., *Force Spectroscopy*, in *Atomic Force Microscopy in Liquid*. 2012, Wiley-VCH Verlag GmbH & Co. KGaA. p. 65-86.
45. Sneddon, I.N., *The relation between load and penetration in the axisymmetric boussinesq problem for a punch of arbitrary profile.* International Journal of Engineering Science, 1965. **3**(1): p. 47-57.
46. Vinckier, A. and G. Semenza, *Measuring elasticity of biological materials by atomic force microscopy.* FEBS Letters, 1998. **430**(1–2): p. 12-16.
47. Lin, D.C., E.K. Dimitriadis, and F. Horkay, *Robust Strategies for Automated AFM Force Curve Analysis—I. Non-adhesive Indentation of Soft, Inhomogeneous Materials.* Journal of Biomechanical Engineering, 2006. **129**(3): p. 430-440.
48. Bilodeau, G.G., *Regular Pyramid Punch Problem.* Journal of Applied Mechanics, 1992. **59**(3): p. 519-523.
49. Murray, B.S. and E. Dickinson, *Interfacial Rheology and the Dynamic Properties of Adsorbed Films of Food Proteins and Surfactants.* Food Science and Technology International, Tokyo, 1996. **2**(3): p. 131-145.
50. MacRitchie, F., *The film Balance and the Measurement of Interfacial Pressure*, in *Chemistry at Interfaces*. 1990, Academic Press. p. 45-75.
51. *Theory of LB Measurements*, in *Software Manual Langmuir and Langmuir-Blodgett devices, All Models, Revision 1.4*. 2013, KSV NIMA/Biolin Scientific Oy. p. 9-14.
52. Rodríguez Patino, J.M., et al., *Structural-Dilatational Characteristics Relationships of Monoglyceride Monolayers at the Air−Water Interface.* Langmuir, 2001. **17**(13): p. 4003-4013.
53. Hexemer, A. and P. Müller-Buschbaum, *Advanced grazing-incidence techniques for modern soft-matter materials analysis.* IUCrJ, 2015. **2**(Pt 1): p. 106-125.
54. Altamura, D., et al., *Assembled Nanostructured Architectures Studied by Grazing Incidence X-Ray Scattering.* Nanomaterials and Nanotechnology, 2012. **2**.
55. Renaud, G., R. Lazzari, and F. Leroy, *Probing surface and interface morphology with Grazing Incidence Small Angle X-Ray Scattering.* Surface Science Reports, 2009. **64**(8): p. 255-380.
56. *Refractive Index*. [cited 2016 October 25, 2016]; Available from: http://gisaxs.com/index.php/Refractive_index.
57. Müller-Buschbaum, P., *A Basic Introduction to Grazing Incidence Small-Angle X-Ray Scattering*, in *Applications of Synchrotron Light to Scattering and Diffraction in Materials and Life Sciences*, M. Gomez, et al., Editors. 2009, Springer Berlin Heidelberg: Berlin, Heidelberg. p. 61-89.
58. Lazzari, R., *IsGISAXS: a program for grazing-incidence small-angle X-ray scattering analysis of supported islands.* Journal of Applied Crystallography, 2002. **35**(4): p. 406-421.
59. Durniak, C.G., Marina; Pospelov, Gennady; Van Herck, Walter; Wuttke, Joachim, *Scattering cross-section*, in *BornAgain Software for simulating and fitting X-ray and*

neutron small-angle scattering at grazing incidence, User Manual 0.3.1 (January 30, 2015) p. 18-48.

60. Vincent, L.G., et al., *Mesenchymal stem cell durotaxis depends on substrate stiffness gradient strength.* Biotechnology Journal, 2013. **8**(4): p. 472-484.
61. Cameron, A.R., J.E. Frith, and J.J. Cooper-White, *The influence of substrate creep on mesenchymal stem cell behaviour and phenotype.* Biomaterials, 2011. **32**(26): p. 5979-5993.
62. Sarras, M.P., *Components, structure, biogenesis and function of the Hydra extracellular matrix in regeneration, pattern formation and cell differentiation.* International Journal of Developmental Biology, 2012. **56**(6-8): p. 567-576.
63. Shimizu, H., et al., *The extracellular matrix of hydra is a porous sheet and contains type IV collagen.* Zoology, 2008. **111**(5): p. 410-418.
64. Bosch, T.C.G., *Hydra and the evolution of stem cells.* Bioessays, 2009. **31**(4): p. 478-486.
65. Campbell, R.D., *Tissue dynamics of steady state growth in Hydra littoralis: I. Patterns of cell division.* Developmental Biology, 1967. **15**(5): p. 487-502.
66. Holstein, T.W., E. Hobmayer, and C.N. David, *Pattern of epithelial cell cycling in hydra.* Developmental Biology, 1991. **148**(2): p. 602-611.
67. Otto, J.J. and R.D. Campbell, *Tissue economics of hydra: regulation of cell cycle, animal size and development by controlled feeding rates.* Journal of Cell Science, 1977. **28**(1): p. 117-132.
68. Campbell, R.D., *Tissue dynamics of steady state growth in Hydra littoralis. II. Patterns of tissue movement.* Journal of Morphology, 1967. **121**(1): p. 19-28.
69. Graf, L. and A. Gierer, *Size, shape and orientation of cells in budding hydra and regulation of regeneration in cell aggregates.* Wilhelm Roux's archives of developmental biology, 1980. **188**(2): p. 141-151.
70. Deutzmann, R., et al., *Molecular, biochemical and functional analysis of a novel and developmentally important fibrillar collagen (Hcol-I) in hydra.* Development, 2000. **127**(21): p. 4669-80.
71. Hausman, R.E. and A.L. Burnett, *The mesoglea of hydra. I. Physical and histochemical properties.* Journal of Experimental Zoology, 1969. **171**(1): p. 7-13.
72. Sarras, M.P. and R. Deutzmann, *Hydra and Niccolo Paganini (1782–1840)—two peas in a pod? The molecular basis of extracellular matrix structure in the invertebrate, Hydra.* BioEssays, 2001. **23**(8): p. 716-724.
73. Davis, L. and J. Haynes, *An ultrastructural examination of the mesoglea of Hydra.* Zeitschrift für Zellforschung und Mikroskopische Anatomie, 1968. **92**(2): p. 149-158.
74. Zhang, X., B.G. Hudson, and M.P. Sarras Jr, *Hydra Cell Aggregate Development Is Blocked by Selective Fragments of Fibronectin and Type IV Collagen.* Developmental Biology, 1994. **164**(1): p. 10-23.
75. Shimizu, H., et al., *Epithelial morphogenesis in hydra requires de novo expression of extracellular matrix components and matrix metalloproteinases.* Development, 2002. **129**(6): p. 1521-1532.
76. Leontovich, A.A., et al., *A novel hydra matrix metalloproteinase (HMMP) functions in extracellular matrix degradation, morphogenesis and the maintenance of differentiated cells in the foot process.* Development, 2000. **127**(4): p. 907-920.
77. Hausman, R.E. and A.L. Burnett, *The mesoglea of hydra. III. Fiber system changes in morphogenesis.* Journal of Experimental Zoology, 1970. **173**(2): p. 175-185.
78. Burnett, A.L. and R.E. Hausman, *Mesoglea of Hydra .2. Possible Role in Morphogenesis.* Journal of Experimental Zoology, 1969. **171**(1): p. 15-&.

79. Roth, S.V., et al., *In situ observation of nanoparticle ordering at the air-water-substrate boundary in colloidal solutions using x-ray nanobeams.* Applied Physics Letters, 2007. **91**(9): p. 091915.
80. Wess, T.J., et al., *Type I collagen packing, conformation of the triclinic unit cell.* Journal of Molecular Biology, 1995. **248**(2): p. 487-493.
81. Orgel, J.P., et al., *Microfibrillar structure of type I collagen in situ.* Proceedings of the National Academy of Sciences of the United States of America, 2006. **103**(24): p. 9001-5.
82. Lo, C.-M., et al., *Cell Movement Is Guided by the Rigidity of the Substrate.* Biophysical Journal, 2000. **79**(1): p. 144-152.
83. Ong, S.-E., et al., *Stable Isotope Labeling by Amino Acids in Cell Culture, SILAC, as a Simple and Accurate Approach to Expression Proteomics.* Molecular & Cellular Proteomics, 2002. **1**(5): p. 376-386.
84. Petersen, H.O., et al., *A Comprehensive Transcriptomic and Proteomic Analysis of Hydra Head Regeneration.* Molecular Biology and Evolution, 2015. **32**(8): p. 1928-1947.
85. Guder, C., et al., *An ancient Wnt-Dickkopf antagonism in Hydra.* Development, 2006. **133**(5): p. 901-911.
86. Augustin, R., et al., *Dickkopf related genes are components of the positional value gradient in Hydra.* Developmental Biology, 2006. **296**(1): p. 62-70.
87. Hobmayer, B., et al., *WNT signalling molecules act in axis formation in the diploblastic metazoan Hydra.* Nature, 2000. **407**(6801): p. 186-189.
88. Lyu, J. and C.-K. Joo, *Wnt-7a Up-regulates Matrix Metalloproteinase-12 Expression and Promotes Cell Proliferation in Corneal Epithelial Cells during Wound Healing.* Journal of Biological Chemistry, 2005. **280**(22): p. 21653-21660.
89. Kessenbrock, K., et al., *A Role for Matrix Metalloproteinases in Regulating Mammary Stem Cell Function via the Wnt Signaling Pathway.* Cell Stem Cell, 2013. **13**(3): p. 300-313.
90. Egea, V., et al., *Tissue inhibitor of metalloproteinase-1 (TIMP-1) regulates mesenchymal stem cells through let-7f microRNA and Wnt/β-catenin signaling.* Proceedings of the National Academy of Sciences, 2012. **109**(6): p. E309–E316.
91. Leost, M., et al., *Paullones are potent inhibitors of glycogen synthase kinase-3β and cyclin-dependent kinase 5/p25.* European Journal of Biochemistry, 2000. **267**(19): p. 5983-5994.
92. Komiya, Y. and R. Habas, *Wnt signal transduction pathways.* Organogenesis, 2008. **4**(2): p. 68-75.
93. Broun, M., et al., *Formation of the head organizer in hydra involves the canonical Wnt pathway.* Development, 2005. **132**(12): p. 2907-2916.
94. Gee, L., et al., *β-catenin plays a central role in setting up the head organizer in hydra.* Developmental Biology, 2010. **340**(1): p. 116-124.
95. Nakamura, Y., et al., *Autoregulatory and repressive inputs localize Hydra Wnt3 to the head organizer.* Proceedings of the National Academy of Sciences of the United States of America, 2011. **108**(22): p. 9137-9142.
96. Bosch, T.C.G., et al., *The Hydra polyp: Nothing but an active stem cell community.* Development, Growth & Differentiation, 2010. **52**(1): p. 15-25.
97. Reinhardt, B., et al., *HyBMP5-8b, a BMP5-8 orthologue, acts during axial patterning and tentacle formation in hydra.* Developmental Biology, 2004. **267**(1): p. 43-59.
98. Rentzsch, F., et al., *An ancient chordin-like gene in organizer formation of Hydra.* Proceedings of the National Academy of Sciences, 2007. **104**(9): p. 3249-3254.

99. Lenhoff, H.M. and R.D. Brown, *Mass culture of hydra: an improved method and its application to other aquatic invertebrates.* Laboratory Animals, 1970. **4**(1): p. 139-154.
100. Shostak, S., N.G. Patel, and A.L. Burnett, *The role of mesoglea in mass cell movement in Hydra.* Developmental Biology, 1965. **12**(3): p. 434-450.
101. Ponchut, C., et al., *MAXIPIX, a fast readout photon-counting X-ray area detector for synchrotron applications.* Journal of Instrumentation, 2011. **6**(01): p. C01069.
102. Gilles, R., U. Keiderling, and A. Wiedenmann, *Silver behenate powder as a possible low-angle calibration standard for small-angle neutron scattering.* Journal of Applied Crystallography, 1998. **31**(6): p. 957-959.
103. Schneider, C.A., W.S. Rasband, and K.W. Eliceiri, *NIH Image to ImageJ: 25 years of image analysis.* Nat Meth, 2012. **9**(7): p. 671-675.
104. Domke, J. and M. Radmacher, *Measuring the Elastic Properties of Thin Polymer Films with the Atomic Force Microscope.* Langmuir, 1998. **14**(12): p. 3320-3325.
105. Dimitriadis, E.K., et al., *Determination of elastic moduli of thin layers of soft material using the atomic force microscope.* Biophysical Journal, 2002. **82**(5): p. 2798-2810.
106. Cox, J. and M. Mann, *MaxQuant enables high peptide identification rates, individualized p.p.b.-range mass accuracies and proteome-wide protein quantification.* Nat Biotech, 2008. **26**(12): p. 1367-1372.
107. Looso, M., et al., *Spiked-in Pulsed in Vivo Labeling Identifies a New Member of the CCN Family in Regenerating Newt Hearts.* Journal of Proteome Research, 2012. **11**(9): p. 4693-4704.
108. Veschgini, M., et al., *Tracking mechanical and morphological dynamics of regenerating Hydra tissue fragments using a two fingered micro-robotic hand.* Applied Physics Letters, 2016. **108**(10): p. 103702.
109. Fütterer, C., et al., *Morphogenetic oscillations during symmetry breaking of regenerating Hydra vulgaris cells.* EPL (Europhysics Letters), 2003. **64**: p. 137.
110. Trembley, A., et al., *Mémoires pour servir à l'histoire d'un genre de polypes d'eau douce, à bras en forme de cornes*. Vol. c.1. 1744, A Leide :: Chez Jean & Herman Verbeek.
111. Kotpal, P.R.L., *Modern Text Book of Zoology: Invertebrates*. 2012: Rastogi Publications.
112. Bosch, T.C.G., *Why polyps regenerate and we don't: Towards a cellular and molecular framework for Hydra regeneration.* Developmental Biology, 2007. **303**(2): p. 421-433.
113. Shimizu, H., Y. Sawada, and T. Sugiyama, *Minimum Tissue Size Required for Hydra Regeneration.* Developmental Biology, 1993. **155**(2): p. 287-296.
114. Gierer, A., et al., *Regeneration of Hydra from reaggregated cells.* Nature/New Biology, 1972. **239**: p. 98.
115. Bode, H.R., *Axial Patterning in Hydra.* Cold Spring Harbor Perspectives in Biology, 2009. **1**(1): p. a000463.
116. Kücken, M., et al., *An Osmoregulatory Basis for Shape Oscillations in Regenerating Hydra.* Biophysical Journal, 2008. **95**(2): p. 978-985.
117. Benos, D.J. and R.D. Prusch, *Osmoregulation in Hydra: Column contraction as a function of external osmolality.* Comparative Biochemistry and Physiology Part A: Physiology, 1973. **44**(4): p. 1397-1400.
118. Benos, D.J. and R.D. Prusch, *Osmoregulation in fresh-waterHydra.* Comparative Biochemistry and Physiology Part A: Physiology, 1972. **43**(1): p. 165-171.
119. Soriano, J., C. Colombo, and A. Ott, *Hydra Molecular Network Reaches Criticality at the Symmetry-Breaking Axis-Defining Moment.* Physical Review Letters, 2006. **97**(25): p. 258102.

120. Technau, U., et al., *Parameters of self-organization in Hydra aggregates.* Proceedings of the National Academy of Sciences, 2000. **97**(22): p. 12127-12131.
121. Mercker, M., A. Köthe, and A. Marciniak-Czochra, *Mechanochemical Symmetry Breaking in Hydra Aggregates.* Biophysical Journal, 2015. **108**: p. 2396-2407.
122. Khangai, N., et al. *Cell stiffness measurement using two-fingered micro-hand equipped with plate-shaped end effector*. in *Ubiquitous Robots and Ambient Intelligence (URAI), 2014 11th International Conference on*. 2014. Kuala Lumpur, Malaysia: IEEE.
123. Ohara, K., et al., *Dextrous cell diagnosis using two-fingered microhand with micro force sensor.* Journal of Micro-Nano Mechatronics, 2012. **7**: p. 13-20.
124. Forgacs, G., et al., *Viscoelastic Properties of Living Embryonic Tissues: a Quantitative Study.* Biophysical Journal, 1998. **74**: p. 2227-2234.
125. Foty, R.A., et al., *Surface tensions of embryonic tissues predict their mutual envelopment behavior.* Development, 1996. **122**: p. 1611-1620.
126. Zasadzinski, J.A., et al., *Overcoming rapid inactivation of lung surfactant: Analogies between competitive adsorption and colloid stability.* Biochimica et Biophysica Acta (BBA) - Biomembranes, 2010. **1798**(4): p. 801-828.
127. Hansen, J.E. and E.P. Ampaya, *Human air space shapes, sizes, areas, and volumes.* Journal of Applied Physiology, 1975. **38**(6): p. 990-995.
128. Ochs, M., et al., *The Number of Alveoli in the Human Lung.* American Journal of Respiratory and Critical Care Medicine, 2004. **169**(1): p. 120-124.
129. Nguyen, P.N., et al., *Behavior of an Adsorbed Phospholipid Monolayer Submitted to Prolonged Periodical Surface Density Variations.* Angewandte Chemie International Edition, 2013. **52**(25): p. 6404-6408.
130. Nakos, G., et al., *Bronchoalveolar lavage fluid characteristics of early intermediate and late phases of ARDS.* Intensive Care Medicine, 1998. **24**(4): p. 296-303.
131. Jorens, P.G., et al., *Interleukin 8 (IL-8) in the bronchoalveolar lavage fluid from patients with the adult respiratory distress syndrome (ARDS) and patients at risk for ARDS.* Cytokine, 1992. **4**(6): p. 592-597.
132. Taeusch, H.W., et al., *Inactivation of Pulmonary Surfactant Due to Serum-Inhibited Adsorption and Reversal by Hydrophilic Polymers: Experimental.* Biophysical Journal, 2005. **89**(3): p. 1769-1779.
133. Warriner, H.E., et al., *A Concentration-Dependent Mechanism by which Serum Albumin Inactivates Replacement Lung Surfactants.* Biophysical Journal, 2002. **82**(2): p. 835-842.
134. Von Der Hardt, K., et al., *Aerosolized Perfluorocarbon Suppresses Early Pulmonary Inflammatory Response in a Surfactant-Depleted Piglet Model.* Pediatr Res, 2002. **51**(2): p. 177-182.
135. Bleyl, J.U., et al., *Changes in pulmonary function and oxygenation during application of perfluorocarbon vapor in healthy and oleic acid-injured animals.* Critical Care Medicine, 2002. **30**(6): p. 1340-1347.
136. Krafft, M.P. and J.G. Riess, *Perfluorocarbons: Life sciences and biomedical uses Dedicated to the memory of Professor Guy Ourisson, a true RENAISSANCE man.* Journal of Polymer Science Part A: Polymer Chemistry, 2007. **45**(7): p. 1185-1198.
137. Gerber, F., et al., *Fluidization of a Dipalmitoyl Phosphatidylcholine Monolayer by Fluorocarbon Gases: Potential Use in Lung Surfactant Therapy.* Biophysical Journal, 2006. **90**(9): p. 3184-3192.
138. Gerber, F., et al., *Potential Use of Fluorocarbons in Lung Surfactant Therapy.* Artificial Cells, Blood Substitutes, and Biotechnology, 2007. **35**(2): p. 211-220.
139. Gerber, F., M.P. Krafft, and T.F. Vandamme, *The detrimental effect of serum albumin on the re-spreading of a dipalmitoyl phosphatidylcholine Langmuir monolayer is*

counteracted by a fluorocarbon gas. Biochimica et Biophysica Acta (BBA) - Biomembranes, 2007. **1768**(3): p. 490-494.

140. Nguyen, P.N., et al., *Reversing the course of the competitive adsorption between a phospholipid and albumin at an air-water interface.* Soft Matter, 2013. **9**(42): p. 9972-9976.
141. Noskov, B.A., et al., *Bovine Serum Albumin Unfolding at the Air/Water Interface as Studied by Dilational Surface Rheology.* Langmuir, 2010. **26**(22): p. 17225-17231.
142. Nguyen, P.N., et al., *Counteracting the inhibitory effect of proteins towards lung surfactant substitutes: a fluorocarbon gas helps displace albumin at the air/water interface.* Chemical Communications, 2014. **50**(78): p. 11576-11579.
143. Kim, S.H. and E.I. Franses, *New protocols for preparing dipalmitoylphosphatidylcholine dispersions and controlling surface tension and competitive adsorption with albumin at the air/aqueous interface.* Colloids and Surfaces B: Biointerfaces, 2005. **43**(3–4): p. 256-266.
144. Krafft, M.P., *Large Organized Surface Domains Self-Assembled from Nonpolar Amphiphiles.* Accounts of Chemical Research, 2012. **45**(4): p. 514-524.
145. Krafft, M.P. and J.G. Riess, *Chemistry, Physical Chemistry, and Uses of Molecular Fluorocarbon−Hydrocarbon Diblocks, Triblocks, and Related Compounds—Unique "Apolar" Components for Self-Assembled Colloid and Interface Engineering.* Chemical Reviews, 2009. **109**(5): p. 1714-1792.
146. Broniatowski, M. and P. Dynarowicz-Łątka, *Semifluorinated alkanes — Primitive surfactants of fascinating properties.* Advances in Colloid and Interface Science, 2008. **138**(2): p. 63-83.
147. Marczuk, P., et al., *Gibbs Films of Semi-Fluorinated Alkanes at the Surface of Alkane Solutions.* Langmuir, 2002. **18**(18): p. 6830-6838.
148. Feng, X., et al., *AFM Study of Gibbs Films of Semifluorinated Alkanes at Liquid Crystal/Air Interfaces.* ChemPhysChem, 2013. **14**(9): p. 1801-1805.
149. Maaloum, M., P. Muller, and M.P. Krafft, *Monodisperse Surface Micelles of Nonpolar Amphiphiles in Langmuir Monolayers.* Angewandte Chemie International Edition, 2002. **41**(22): p. 4331-4334.
150. Fontaine, P., et al., *Direct Evidence for Highly Organized Networks of Circular Surface Micelles of Surfactant at the Air−Water Interface.* Journal of the American Chemical Society, 2005. **127**(2): p. 512-513.
151. Kato, T., et al., *Monodisperse Two-Dimensional Nanometer Size Clusters of Partially Fluorinated Long-Chain Acids.* Langmuir, 1998. **14**(7): p. 1786-1798.
152. Trabelsi, S., et al., *Correlating Linactant Efficiency and Self-Assembly: Structural Basis of Line Activity in Molecular Monolayers.* Langmuir, 2009. **25**(14): p. 8056-8061.
153. Zhang, G., et al., *Surface micelles of semifluorinated alkanes in Langmuir-Blodgett monolayers.* Physical Chemistry Chemical Physics, 2004. **6**(7): p. 1566-1569.
154. Huang, Z., et al., *Structural studies of semifluorinated hydrocarbon monolayers at the air/water interface.* Journal of the Chemical Society, Faraday Transactions, 1996. **92**(4): p. 545-552.
155. de Viguerie, L., et al., *Effect of the Molecular Structure on the Hierarchical Self-Assembly of Semifluorinated Alkanes at the Air/Water Interface.* Langmuir, 2011. **27**(14): p. 8776-8786.
156. Mourran, A., et al., *Self-Assembly of the Perfluoroalkyl-Alkane F14H20 in Ultrathin Films.* Langmuir, 2005. **21**(6): p. 2308-2316.
157. Broniatowski, M., et al., *Langmuir Monolayers Characteristic of (Perfluorodecyl)-Alkanes.* The Journal of Physical Chemistry B, 2004. **108**(35): p. 13403-13411.

158. Broniatowski, M., I. Sandez Macho, and P. Dynarowicz-Łątka, *Study of perfluorooctyl-n-alkanes monolayers at the air–water interface.* Thin Solid Films, 2005. **493**(1–2): p. 249-257.
159. Broniatowski, M., J. Miñones Jr, and P. Dynarowicz-Łątka, *Semifluorinated chains in 2D-(perfluorododecyl)-alkanes at the air/water interface.* Journal of Colloid and Interface Science, 2004. **279**(2): p. 552-558.
160. Abed, A.E., et al., *Experimental evidence for an original two-dimensional phase structure: An antiparallel semifluorinated monolayer at the air-water interface.* Physical Review E, 2002. **65**(5): p. 051603.
161. El Abed, A., et al., *Air-water interface-induced smectic bilayer.* Physical Review E, 2000. **62**(5): p. R5895-R5898.
162. Gonzalez-Perez, A., C. Contal, and M.P. Krafft, *Experimental evidence for a surface concentration-dependent mechanism of formation of hemimicelles in Langmuir monolayers of semi-fluorinated alkanes.* Soft Matter, 2007. **3**(2): p. 191-193.
163. Zhang, G., et al., *Occurrence, Shape, and Dimensions of Large Surface Hemimicelles Made of Semifluorinated Alkanes. Elongated versus Circular Hemimicelles. Pit- and Tip-Centered Hemimicelles.* Journal of the American Chemical Society, 2005. **127**(29): p. 10412-10419.
164. de Gracia Lux, C., et al., *Compression of Self-Assembled Nano-Objects: 2D/3D Transitions in Films of (Perfluoroalkyl)Alkanes—Persistence of an Organized Array of Surface Micelles.* Chemistry – A European Journal, 2010. **16**(24): p. 7186-7198.
165. Fontaine, P., et al., *Evidence for Interaction with the Water Subphase As the Origin and Stabilization of Nano-Domain in Semi-Fluorinated Alkanes Monolayer at the Air/Water Interface.* Langmuir, 2014. **30**(50): p. 15193-15199.
166. Theodoratou, A., et al., *Semifluorinated Alkanes at the Air–Water Interface: Tailoring Structure and Rheology at the Molecular Scale.* Langmuir, 2016. **32**(13): p. 3139-3151.
167. Bardin, L., et al., *Long-Range Nanometer-Scale Organization of Semifluorinated Alkane Monolayers at the Air/Water Interface.* Langmuir, 2011. **27**(22): p. 13497-13505.
168. McConnell, H.M. and R. De Koker, *Note on the theory of the sizes and shapes of lipid domains in monolayers.* The Journal of Physical Chemistry, 1992. **96**(17): p. 7101-7103.
169. Dynarowicz Łatka, P., et al., *Structural Investigation of Langmuir and Langmuir−Blodgett Monolayers of Semifluorinated Alkanes.* The Journal of Physical Chemistry B, 2006. **110**(12): p. 6095-6100.
170. Schmidbauer, M., *Dynamical Scattering Effects at Grazing Incidence Conditions*, in *X-Ray Diffuse Scattering from Self-Organized Mesoscopic Semiconductor Structures (Springer Tracts in Modern Physics)*. 2004, Springer-Verlag Berlin Heidelberg. p. 127-138.
171. Volpati, D., et al., *Semifluorinated thiols in Langmuir monolayers – A study by nonlinear and linear vibrational spectroscopies.* Journal of Colloid and Interface Science, 2015. **460**: p. 290-302.
172. Zenasni, O., et al., *Self-assembled monolayers on gold generated from terminally perfluorinated alkanethiols bearing propyl vs. ethyl hydrocarbon spacers.* Journal of Fluorine Chemistry, 2014. **168**: p. 128-136.
173. Giulieri, F., et al., *Impact of the Spacer on the Condensing Effect of Fluorinated Chains Investigated by Grazing Incidence X-ray Diffraction on Ultrathin Langmuir Monolayers.* Langmuir, 2012. **28**(33): p. 12022-12029.

174. Ren, Y., K.-i. Iimura, and T. Kato, *Surface Micelles of F(CF2)m(CH2)22COOH on the Aqueous Cadmium Acetate Solution Investigated in Situ and ex Situ by Infrared Spectroscopy.* The Journal of Physical Chemistry B, 2002. **106**(6): p. 1327-1333.
175. Semenov, A.N., et al., *Theory of Surface Micelles of Semifluorinated Alkanes.* Langmuir, 2006. **22**(21): p. 8703-8717.
176. Babonneau, D., *FitGISAXS: software package for modelling and analysis of GISAXS data using IGOR Pro.* Journal of Applied Crystallography, 2010. **43**(4): p. 929-936.